

**Study of Spectral function scaling property of High Temperature  
Superconductors**

**BY**

**DINGFEI AI**

**B.S, Wuhan University 2006**

**THESIS**

Submitted in partial fulfillment of the requirements  
for the degree of Doctor of Philosophy in Physics  
in the Graduate College of the  
University of Illinois at Chicago, 2011

Chicago, Illinois

Defense Committee:

Juan Carlos Campuzano, Chair and Advisor  
Anjum Ansari  
Mark Schlossman  
Wai- Yee Keung  
Robert Klie, Physics Department University of Illinois at Chicago  
Michael Norman, Argonne National Laboratory

## ACKNOWLEDGMENTS

All the result and works presented in this thesis are the crystal of more than five years of my work. And it would not have been possible without the guidance and support from many people. First and foremost, I would like to thank my parents for being the constant source of emotional and material support all through graduate school years, no matter it is good or difficult time.

Thanks to all of my colleagues in the group, for their indelible contributions and support that resulted in many of the results presented in this thesis. To Dr. Utpal Chatterjee who introduced me to the world of experimental physics, who acted as guidance through my transition from fresh graduate student to experimentalist, who took the role of big brother in personal life. To Dr. Ming Shi for being always like a father to me and for teaching me about experimental technics and data analysis method. To Dr. Junjing Zhao for experiment and data discussions, for generous help during our long experiment time in Synchrotron Radiation Center. Thanks to Fanny R, Jim for joining me during our experiment time at Synchrotron Radiation Center.

Thanks to all the stuffs in the machine shop at UIC, for their professional design and works on our experiment setup,. Special thanks to Greg Rogers and Mike Fisher at SRC for helping us to solving alot of problem in experiment setup during our experiment time. Thanks to Dr. Tom Miller for always helping me during tough times at Synchrotron Radiation Center.

## ACKNOWLEDGMENTS (Continued)

Thanks to Prof Dirk Morr whom I indebted so much for teaching me advanced concepts in Condensed matter Physics from which I benefit alot through my condensed matter experimental study.

Many thanks to the senior collaborators of our group — Prof M. Randeria, Prof M. Norman. Every discussiong with them is always a precious experience as they always brought up some insightful opinions and innovational ideas.

Finally my largest gratitude to my advisor Prof Juan Carlos Campuzano. This thesis could not have ever been a reality without his help and support. During my PhD studies in his lab, he not only taught me about Physics knowledge, but also taught mehow to think independently and rationally in order to hurdle all the obstacles in the research work.

# TABLE OF CONTENTS

| <u>CHAPTER</u> |   | <u>PAGE</u> |
|----------------|---|-------------|
| <b>1</b>       | <b>ABSTRACT . . . . .</b>   | <b>1</b>    |
| <b>2</b>       | <b>SEVERAL FEATURES OF HIGH <math>T_C</math> SUPERCONDUCTORS . . . . .</b>  | <b>3</b>    |
| 2.1            | Introduction . . . . .  | 3           |
| 2.2            | Superconductivity . . . . .   | 4           |
| 2.3            | Conventional Superconductivity . . . . .  | 4           |
| 2.4            | SC order parameter . . . . .  | 14          |
| 2.5            | High Temperature(High $T_c$ ) Superconductor . . . . .  | 15          |
| 2.6            | Common features among different HTSC materials . . . . .  | 19          |
| 2.7            | Crystal Structure . . . . .   | 20          |
| 2.8            | The parent compound . . . . .   | 21          |
| 2.9            | Doping the parent compound . . . . .  | 23          |
| 2.10           | Pseudogap Phase . . . . .   | 26          |
| 2.11           | Superconducting state . . . . .   | 31          |
| <b>3</b>       | <b>EXPERIMENTAL TECHNIQUES:ANGLE RESOLVED PHOTOEMISSION . . . . .</b>   | <b>34</b>   |
| 3.1            | Basics of Photonemission Spectroscopy . . . . .   | 34          |
| 3.2            | Energetics of Angle Resolved Photoemission Spectroscopy . . . . .   | 37          |
| 3.3            | Spectral Function formalism of ARPES data . . . . .   | 40          |
| 3.4            | Different representations of ARPES data . . . . .   | 46          |
| <b>4</b>       | <b>ELECTRONIC PHASE DIAGRAM OF HIGH-TEMPERATURE COPPER OXIDE SUPERCONDUCTORS . . . . .</b>  | <b>49</b>   |
| 4.1            | ARPES measurement and data analysis . . . . .   | 50          |
| 4.2            | $T^*$ and $T_{coh}$ . . . . .   | 50          |
| 4.3            | Quantative determination of $T^*$ and $T_{coh}$ line . . . . .  | 59          |
| 4.4            | Conclusion . . . . .  | 61          |
| <b>5</b>       | <b>OBSERVATION OF A D-WAVE NODAL LIQUID IN HIGHLY UNDERDOPED <math>\text{Bi}_2\text{Sr}_2\text{CaCu}_2\text{O}_{8+\delta}</math> (BI2212) . . . . .</b> | <b>63</b>   |
| 5.1            | Samples . . . . .   | 64          |
| 5.2            | How to measure the energy gap using ARPES . . . . .   | 64          |
| 5.2.1          | Symmterization . . . . .  | 65          |
| 5.3            | Gap anisotropy in the PG state and in the SC state . . . . .  | 67          |
| 5.4            | Result . . . . .  | 69          |

## TABLE OF CONTENTS (Continued)

| <u>CHAPTER</u> |  | <u>PAGE</u> |
|----------------|--|-------------|
| 5.5            | Anisotropic gap of insulating and superconducting samples . .                            | 72          |
| 5.6            | Conclusion . . . . .   | 75          |
| <b>6</b>       | <b>SCALING CHARACTERISTIC OF SPECTRAL FUNCTION<br/>OF UNDER-DOPED CUPRATES . . . . .</b> | 78          |
| 6.1            | Motivation . . . . .   | 78          |
| 6.2            | Methodolog and results . . . . .   | 79          |
| 6.2.1          | Temperature term . . . . .   | 82          |
| 6.2.2          | K parallel term . . . . .  | 91          |
| 6.3            | Conclusion . . . . .   | 109         |
|                | <b>CITED LITERATURE . . . . .</b>  | 110         |
|                | <b>VITA . . . . .</b>  | 121         |

## LIST OF FIGURES

| <u>FIGURE</u> |   | <u>PAGE</u> |
|---------------|---|-------------|
| 1             | Resistivity versus Temperature of Mercury superconductor . . . . .  | 6           |
| 2             | (A) A regular conductor is placed in a magnetic field and consequently some magnetic flux gets trapped inside it. (B) and (C) shows how superconductivity is different from the state of just perfect conductivity. .                         | 8           |
| 3             | Temperature dependence of SC gap . . . . .  | 16          |
| 4             | History of discovery from Superconductor to of higher $T_c$ Superconductor  | 18          |
| 5             | Crystal Structure for three different families of HTSC materials. (a) $\text{La}_{2(1-x)}\text{Sr}_2\text{CuO}_4$ , (b) $\text{YBa}_2\text{Cu}_3\text{O}_{7+\delta}$ , (c) $\text{Bi}_2\text{Sr}_2\text{CaCu}_2\text{O}_{8+\delta}$ . . . . . | 21          |
| 6             | Phase diagram of hole doped cuprates . . . . .  | 25          |
| 7             | Energetics of the photoemission process . . . . .   | 36          |
| 8             | Mechanism of ARPES experiment . . . . .   | 38          |
| 9             | Energy Momentum Relation from ARPES data . . . . .  | 41          |
| 10            | Graphic of One step and Three step process . . . . .  | 42          |
| 11            | EDC and MDC intepretation of ARPES data . . . . .   | 47          |
| 12            | Phase diagram schematics:(A) Schematic phase diagram for a quantum critical point near optimal doping. (B) Schematic phase diagram for a doped Mott insulator. . . . .  | 52          |

# LIST OF FIGURES (Continued)

## FIGURE

## PAGE

- 13      Spectra at constant temperature as a function of doping. (A) Dots indicate the temperature and doping values of the spectra of the same color plotted in BD. (B) Spectra at  $T \sim 300K$  for several samples measured at the antinode, where the d-wave superconducting gap below  $T_c$  is largest. The spectra are normalized to high binding energy and symmetrized in energy to eliminate the Fermi function. The doping values are indicated by the top row of dots in A. (C) Same as in B, but at  $T \sim 150K$ , with the dopings indicated by the middle row of dots in A. (D) Same as in B, but at  $T = 100K$ , with the dopings indicated by the bottom row of dots in A. . . . . 53
  
- 14      Additional signatures of spectral coherence. a Spectra for a small range of binding energy for different temperatures, showing the break visible when the coherent component merges with the incoherent component. The straight lines are guides to the eye. These spectra are for an overdoped 67K sample. b Derivative of the top spectrum shown in a. The sharp change in the slope at the break point is indicated by the arrows. c Spectra at constant energy (integrated over 10mev around the Fermi energy) as a function of momentum. The different curves are from the same sample, for increasing temperatures from bottom to top. At low T, four peaks are observed due to the splitting of the CuO<sub>2</sub> states into bonding and antibonding combinations. These two combinations merge at  $T_{coh}$  into a single broad peak. b Intensity map of the dispersion, with the bottom panel corresponding to the bottom spectra in c, and the top panel to the top spectra in c. . . . . 54
  
- 15      Spectra at constant doping as a function of temperature. (A) Dots indicate the temperature and doping values of the spectra of the same color plotted in BD. (B) Symmetrized antinodal spectra for two optimally doped samples ( $\delta = 0.16$ ). The temperature values are indicated by the left row of dots in A. (C) Same as in B, but for a doping of  $\delta = 0.183$ , with the temperatures indicated by the middle row of dots in A. (D) Same as in B, but for a doping of  $\delta = 0.224$ , with the temperatures indicated by the right row of dots in A. Gray lines in B and C mark the location of the gap. . . . . 58

## LIST OF FIGURES (Continued)

| <u>FIGURE</u> |  | <u>PAGE</u> |
|---------------|--|-------------|
| 16            | <p>Fermi function divided spectra. (A) Antinodal spectra for two optimally doped samples, <math>\delta = 0.16</math>, showing sharp peaks with an energy gap (green curves) below <math>T_c</math>, but broad gapless spectra (purple curve) above <math>T_c</math>. Colored lines show Fermi function-divided data, with symmetrized data superimposed as sharp black lines. (B) Spectra for an overdoped sample, <math>\delta = 0.183</math>, showing that, unlike in A, the spectral gap is lost above 100 K, whereas the sharp peak persists to higher temperature. (C) Data for an overdoped <math>\delta = 0.224</math> sample. The sharp spectral peak decreases in intensity with increasing temperature. By <math>T = 250K</math>, the spectral line shape is broad and temperature independent. (D) Linearly decreasing intensity of the sharp spectral peak relative to the broad Lorentzian with increasing <math>T</math> for three values of <math>\delta</math>. <math>T_{coh}</math> is where this intensity reaches zero. (E) Momentum distribution curves (MDCs) for an overdoped <math>\delta = 0.224</math> sample, showing that a qualitative change in spectral shape occurs near <math>T_{coh}</math>. (F) Comparison of the MDC of an OP doped sample, to that of an OD sample at a similar <math>T</math>. (G) <math>T</math>-independence of the spectral shape for an OP sample above <math>T_{coh}</math>. . .</p> | 60          |
| 17            | <p>Electronic phase diagram of <math>Bi_2Sr_2CaCu_2O_{8+\delta}</math> versus hole doping, <math>\delta</math>. Brown dots indicate incoherent gapped spectra, blue points coherent gapped spectra, green dots coherent gapless spectra, and red dots incoherent gapless spectra. The brown double triangles denote <math>T_c</math>, and the green double triangles <math>T_{coh}</math>. <math>T_c</math> denotes the transition temperature into the superconducting state (shaded gray and labeled <math>D - wave</math> SC). . .</p>  | 62          |
| 18            | <p>Symmetrized EDCs for underdoped samples along the Fermi surface. (a) <math>T_c = 90K</math> sample in the superconducting state at <math>T = 40K</math>, and (b) the same sample in the pseudogap phase at <math>T = 140K</math>. The bottom EDC is at the node, while the top is at the anti-node, as defined in (d). (c) Variation of the gap around the Fermi surface extracted from (a) and (b). (d) Location of the momentum cuts (red lines), Fermi surface (blue curves), and special points (node and anti-node) in the zone. (e) Symmetrized EDCs for a very underdoped, <math>T_c = 25K</math>, sample (corresponding to <math>k_F</math> points 4 through 15), measured at 55K in the pseudogap state. . . . .</p>   | 68          |
| 19            | <p>Data for non-superconducting samples. (a) Schematic phase diagram of <math>Bi_2Sr_2CaCu_2O_{8+\delta}</math> in the hole-doping (<math>\delta</math>), temperature (<math>T</math>) plane. The arrow indicates the doping level of the non-superconducting thin film samples whose data are shown in subsequent panels. (b) <math>T</math>-dependence of the resistance showing an insulating upturn. (c) Low-energy ARPES intensity at <math>T=16K</math> . . . . .</p>  | 71          |



## LIST OF FIGURES (Continued)

| <u>FIGURE</u> |  | <u>PAGE</u> |
|---------------|--|-------------|
| 20            | <p>Spectral function vs. doping. (a) The doping levels <math>\delta</math> of the four samples whose spectra are shown in panels (d) through (g). The determination of <math>\delta</math> is described in the Supplemental section. (b) Nodal spectrum and background (see text) for the non-superconducting sample D in (a) at <math>T = 16\text{K}</math>. c Backgroundsubtracted, symmetrized intensity for sample D at the antinode (<math>\theta = 0</math>) showing a gap and node (<math>\theta = 45</math>) with zero gap. (d) through (g) show symmetrized EDCs, without background subtraction, for (d) the non-superconducting thin film at <math>T = 16\text{K}</math>, (e) an underdoped <math>T_c = 33\text{K}</math> thin film at <math>T = 16\text{K}</math>; (f) an underdoped <math>T_c = 69\text{K}</math> single crystal at <math>T = 20\text{K}</math>, and (g) a near-optimal <math>T_c = 80\text{K}</math> thin film at <math>T = 40\text{K}</math>. In each panel (d) through (g) the spectra are plotted with increasing from 0 (antinode) at the top to 45 (node) at the bottom. Note the highly anisotropic gap seen at all four doping levels, with sharp quasiparticle peaks at the gap edge at all <math>K_F</math>, with weight diminishing with underdoping for all superconducting samples. Even after superconductivity is lost, we see in (d) a clear low-energy gap scale as emphasized by the red lines drawn in the top spectrum. . . . .</p> | 73          |
| 21            | <p>The spectral gap as a function of angle around the Fermi surface and doping. (a) The spectral gap <math>\Delta(\theta)</math>, normalized by its maximum value at the antinode, plotted as a function of the Fermi surface angle <math>\theta</math>. Different colors are used for various superconducting samples (single crystals and thin films), while an open symbol is used for the non-superconducting sample. The energy gap at all doping levels is consistent with the d-wave form <math>\cos(2\theta)</math> shown as a black curve. (b) Maximum gap as a function of hole-doping. Gaps of the superconducting samples are denoted by filled symbols (blue for thin films and red for single crystals measured in this work, and green for published data), while open circles are used for the non-superconducting samples. . . . .</p>  | 77          |
| 22            | <p>Background subtraction procedure. (a) intensity map of energy and momentum. (b) EDC far away from <math>k_F</math> (c) the spectrum before the background subtraction (d) the spectrum after background subtraction.</p>  | 81          |
| 23            | Fermi function divided intensity map . . . . .   | 83          |
| 24            | Raw data for under-doped ( $T_c=78\text{K}$ ), EDCs at different temperatures .  | 85          |
| 25            | Scaled data for under-doped ( $T_c=78\text{K}$ ), EDCs at different temperatures   | 86          |
| 26            | Scaling result for larger energy range from $-600\text{meV}$ to $0\text{meV}$ . . . . .  | 87          |

## LIST OF FIGURES (Continued)

| <u>FIGURE</u> |   | <u>PAGE</u> |
|---------------|---|-------------|
| 27            | Comparison of different scaling parameter values (a) $\alpha = 0.3$ (b) $\alpha = 0.5$<br>(c) $\alpha = 0.6$ (d) $\alpha = 0.9$ . . . . . | 88          |
| 28            | Chi-square value as function of scale parameter . . . . .   | 89          |
| 29            | Scaled data for under-doped ( $T_c=47K$ ), EDCs at different temperatures   | 90          |
| 30            | Scaled data for under-doped ( $T_c=85K$ ), EDCs at different temperatures   | 91          |
| 31            | Tight-binding fit of the Fermi surface . . . . .  | 94          |
| 32            | Intensity and $k_{  }$ value in 3D map (a) the intensity (b) the $k_{  }$ . . . . .   | 95          |
| 33            | Intensity and $k_{  }$ value in 2D map (a) the intensity (b) the $k_{  }$ . . . . .   | 96          |
| 34            | Raw data for under-doped ( $T_c=68K$ ), MDCs for different temperature .  | 99          |
| 35            | Scaled data for under-doped ( $T_c=68K$ ), MDCs for different temperature   | 100         |
| 36            | Unscaled and scaled data for under-doped ( $T_c=80K$ ), MDCs for different<br>temperature . . . . .                                       | 101         |
| 37            | Momentum lines chosen for Fig.33, 34 . . . . .  | 102         |
| 38            | Scaling parameter versus Fermi-surface cut . . . . .  | 103         |
| 39            | Scaling result for different value of z (a) result for z=1 (b) result for z=2<br>(c) result for z=8 . . . . .                             | 104         |
| 40            | Scaling result for different value of z (a) result for z=1.1 (b) result for<br>z=0.6 (c) result for z=0.2 . . . . .                       | 105         |
| 41            | Scaling result for smaller $k_{  }$ range . . . . .   | 107         |
| 42            | Scaled data for over-doped ( $T_c=67K$ ) and chi-square (a) scaled data (b)<br>chi-square value vs parameters . . . . .                   | 108         |
| 43            | Measured samples in phase diagram . . . . .   | 109         |

## LIST OF ABBREVIATIONS

|                |  |
|----------------|--|
| ARPES          | Angle Resolved Photoemission Spectroscopy                |
| CMR            | Colossal Magneto Resistance                              |
| DC             | Direct Current   |
| SC             | Superconducting  |
| $T_c$          | Critical Temperature                                     |
| PG             | Pseudogap  |
| HTSC           | High Temperature Superconductor                          |
| FL             | Fermi Liquid   |
| PG             | Pseudogap  |
| HTSC           | High Temperature Superconductor                          |
| BCS            | Bardeen Cooper Schrieffer                                |
| Bi2212         | $\text{Bi}_2\text{Sr}_2\text{CaCu}_2\text{O}_{8+\delta}$ |
| $\text{CuO}_2$ | Copper Oxygen  |
| Cu             | Copper   |
| O              | Oxygen   |
| Bi             | Bismuth  |
| BiO            | Bismuth Oxygen   |

## LIST OF ABBREVIATIONS (Continued)

|     |                             |
|-----|-----------------------------|
| FS  | Fermi Surface               |
| PES | Photoemission Spectroscopy  |
| UHV | Ultra High Vacuum           |
| EDC | Energy Distribution Curve   |
| MDC | Momentum Distribution Curve |

## CHAPTER 1

### ABSTRACT

High Temperature Superconductors (HTSCs) were first discovered in 1986, but despite enormous amount of research for last two decades, these materials are still not yet completely understood. HTSCs exhibit very complicated three dimensional phase diagram parameterized by temperature, magnetic field and carrier concentration. Up to now we do not know how to properly characterize all of their different phases, in particular the so-called pseudogap (PG) phase where the system is not macroscopically a superconductor but shows properties similar to the superconducting (SC) state. Angle Resolved Photoemission Spectroscopy (ARPES) that probes the momentum space structure of a system has greatly contributed to our understanding of the electronic structure of HTSCs. In this thesis I will present various ARPES studies on HTSCs.

In order to understand the origin of high temperature superconductivity in copper oxides, we must understand the normal state from which it emerges. I will present the evolution of the normal state electronic excitations with temperature and carrier concentration in  $\text{Bi}_2\text{Sr}_2\text{CaCu}_2\text{O}_{8+\delta}$  using ARPES data. I will show that unlike conventional superconductor, the high temperature superconductors exhibit two additional temperature scales which are pseudogap scale  $T^*$ , below which electronic excitations exhibit an energy gap, coherence scale  $T_{\text{coh}}$ , below which sharp spectral features appear due to increased lifetime of the excitations. And  $T^*$  and  $T_{\text{coh}}$  are strongly doping dependent, and cross each other near optimal doping.

I will also present ARPES observation of the electronic excitations of the non-superconducting state that exists between the antiferromagnetic Mott insulator at zero doping and the superconducting state at larger dopings in  $\text{Bi}_2\text{Sr}_2\text{CaCu}_2\text{O}_{8+\delta}$  (Bi2212). I will show that the state is a nodal liquid whose excitation gap becomes zero only at points in momentum space, and the material has the same gap structure as the d-wave superconductor despite that it has resistivity characteristic of an insulator and the absence of coherent quasiparticle peaks. And there is a smooth evolution of the spectrum across the insulator-to-superconductor transition

At the end I will show our scaling analysis of ARPES data across the phase diagram. From the scaling analysis, we find that there is a 2-D scaling relation in the pseudogap phase, but not in the normal states in the over-doped phase. Thus the states in the pseudogap phase share the same properties that are different from over-doped phase. And also because of the scaling relation, there is quantum critical line along the Fermi-surface in the pseudogap phase.

## CHAPTER 2

### SEVERAL FEATURES OF HIGH $T_C$ SUPERCONDUCTORS

#### 2.1 Introduction

One crucial challenge in condensed matter physics is to understanding the collective behavior of vast assemblies of interacting particles systems, which could be anything from an organic bio-molecule to a piece of metal. It is natural to think that if we knows the physical properties of each of the constituents and the fundamental laws, then understanding the behavior of the whole system would be quite trivial. But unfortunately this kind of reductionist hypothesis is not true in reality. As a simple example, let us consider the case of a gold wire, made of a very large number of gold atoms. Although a single gold atom does not conduct electricity, the gold wire itself is a very good conductor. Hence for an interacting many-body system, the very fact that the system has large number of degrees of freedoms thus requires new physical concepts to understand it. In this context, one of the most fundamental aspects of a many body system is that the symmetry of the whole system generally does not follow the symmetry of the laws which govern it; on contrast the whole system usually has lower symmetry. This brought up one of the most important and recent ideas in physics, which is called the concept of broken symmetry. For instance if we consider the case of a crystal: the microscopic laws binding atoms into a crystalline structure have perfect spatial homogeneity, while on the hand crystal itself does not. Because in the crystalline state the system loses its continuous translational symmetry. It is

quite important to note that by using the fundamental laws of quantum mechanics, one could not explain such a spontaneous translational symmetry broken in crystals. There are a lot of extraordinary and fascinating physical phenomena in nature which occur on a macroscopic scale, e.g. superconductivity, ferromagnetism, anti-ferromagnetism, ferroelectricity, the kondo effect, colossal magneto resistance(CMR) and so on. These special properties are a direct consequence of the fact that the collective behavior of a system which is consist of many particle is qualitatively different from that of its constituents, in other words the whole system becomes not only more than but very different from the sum of the parts. In this thesis we will focus our discussions only on superconductivity.

## **2.2 Superconductivity**

As their name stated, superconductors have absolutely zero resistance to electric currents below a certain temperature, so called the critical temperature ( $T_c$ ) and below a certain critical value of magnetic field  $H_c$ . Superconductors have the following unique features that different from perfect conductor:

- (i) the superconductor has absolutely zero resistance to DC Electric current
- (ii) the superconductor perfectly excludes magnetic flux

## **2.3 Conventional Superconductivity**

For conventional metals, because of the reduction of inelastic scattering of electrons by phonons, the resistivity usually decreases as the the temperature decrease. The temperature dependence of the resistivity in a metal can be written as  $\rho(t) = \rho_0 + cT^5$  where  $\rho_0$  is the residual



resistivity due to lattice imperfections and impurities in the sample and  $T$  is the temperature. One might ask what would happen to the resistivity as  $T$  approaches zero. It was the year of 1911 when Kammerlingh Onnes and his assistant Holst were measuring the resistance of mercury. To their surprise they discovered that below 4.1K, the resistivity of mercury became exactly zero (Fig. 1)[2]. It took quite a while for both Holst and Onnes to understand that the zero resistivity property of mercury below 4.1K, was not an experimental artifact but the manifestation of a new electronic phase namely superconductivity. It also took many decades for the scientific community to pay attention to Holst's contribution to this discovery. Soon after this discovery, superconductivity was observed in other materials such as thallium, tin and so on.

Other than absolute zero resistance, the perfect diamagnetism of the superconducting (SC) state makes it a unique thermodynamic state which is more than just a state of perfect conductivity (Fig. 2). In order to prove this point, let us consider a hypothetical transition in which a regular conductor turns into a perfect conductor (conductivity  $\sim \infty$ ) for  $T \leq T_N$ . If we put this conductor in a magnetic field, some magnetic flux will be trapped inside it (Fig. 2A). Now, let us first cool down the conductor below  $T_N$ , then put it in a magnetic field. There would be no magnetic flux inside (Fig. 2B), because the system is in a state where the conductivity, and hence the magnetic permeability ( $\mu$ ), is infinite. Then we put the system in a magnetic field at some temperature  $T > T_N$ . As a result some of the field will be trapped inside it, as its conductivity above  $T_N$  is finite. Afterwards if we cool it down through  $T_N$ , the field will still remain trapped inside, even though the system is in a state of perfect conductivity. Therefore

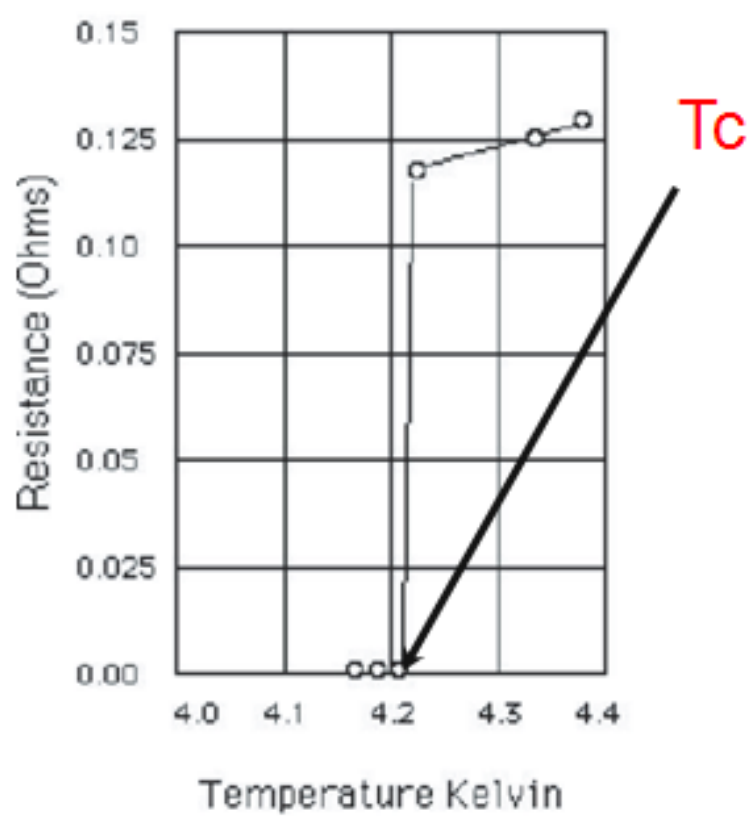


Figure 1. Resistivity versus Temperature of Mercury superconductor

the two processes (a) first cooling down through  $T_N$  and then apply of the field, (b) first apply the field and then cooling down through  $T_N$ , do not lead to same state. On the contrary, as shown in Fig. 2C, in the case of the superconducting transition, those two processes will always lead to same state because of perfect diamagnetism. Hence the superconducting state is not just a state of perfect conductivity, but rather a new state of matter. Another peculiar phenomenon associated with the superconducting state is that of flux quantization, where the magnetic flux enclosed within a hollow superconducting sample is an integral multiple of the fundamental unit  $\frac{hc}{2e}$ . where,  $h$  is Planck's constant and  $c$  is velocity of light.

After the discovery of the superconductor, a great deal of experiment were conducted and followed by many attempts from theoreticians between 1930 and 1950 to understand the mechanism behind superconductivity. Major progress was made with the two fluid model proposed by the London theory [7] in 1935 and then by the Ginzburg-Landau theory in 1950 [8]. Eventually the microscopic theory for superconductivity, known as the BCS theory, was proposed by Bardeen, Cooper and Schrieffer in 1957 almost half a century after the discovery of superconductivity [9]. The most important concept of the BCS theory is that electrons form pairs. The electron pairs which are paired via electron-phonon interactions are called Cooper pairs, and they condense into a single coherent ground state. An electron attracts ions in the lattice and will cause a slight increase in positive charge density around it. This increase in positive charge density will, in turn, attract another electron and the two will form a pair. The Cooper pairs are held together by a certain "binding energy", and can only undergo scattering in the ion lattice if the energy associated with the scattering process is sufficient to split up the Cooper

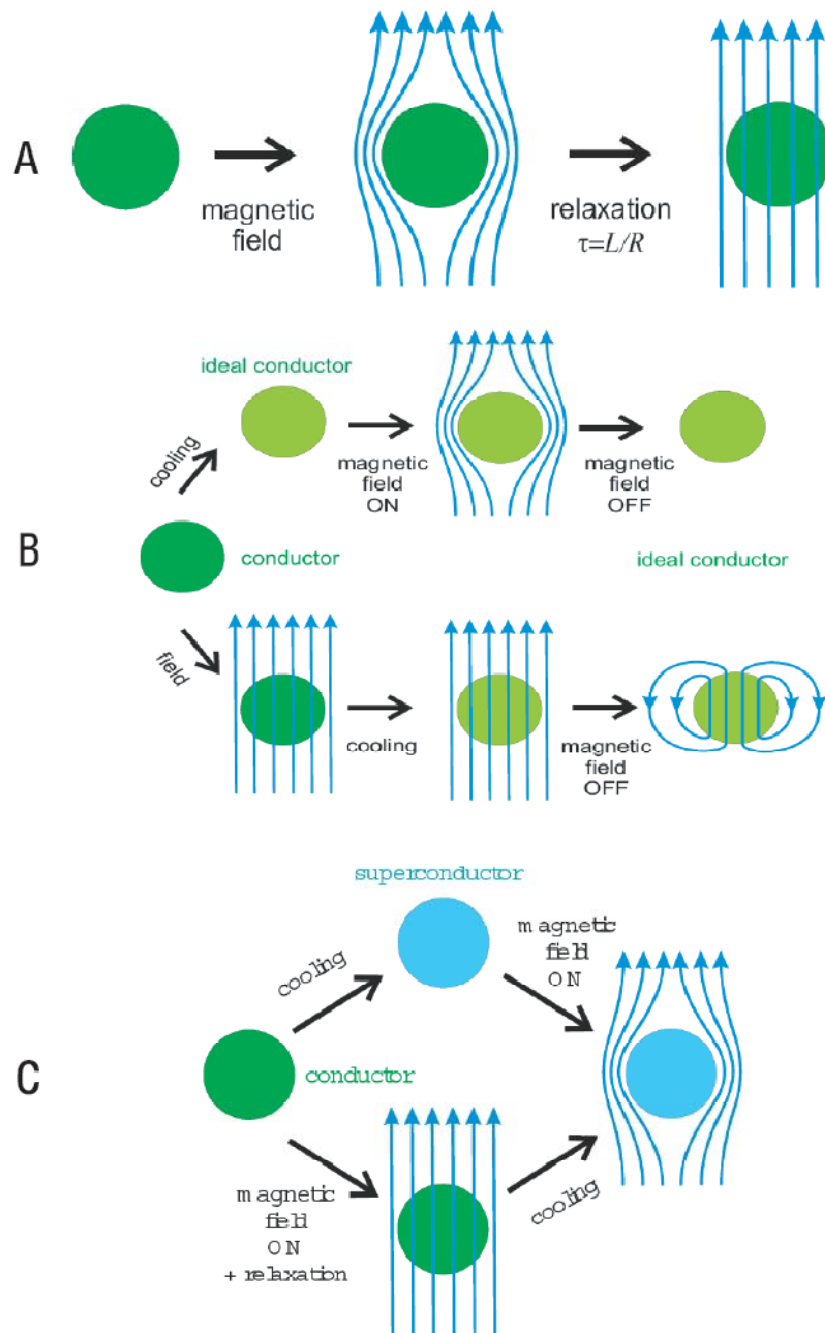


Figure 2. (A) A regular conductor is placed in a magnetic field and consequently some magnetic flux gets trapped inside it. (B) and (C) shows how superconductivity is different from the state of just perfect conductivity.

pairs into their constituent electrons. Otherwise, the Cooper pairs will move through the lattice unscattered. One possible source of energy that could break the binding energy of a Cooper pair is the thermal vibrations of the ion lattice. However, at low temperatures the thermal energy of the lattice is much lower than it is at higher temperatures. Therefore, at low temperatures, the energy to break up the Cooper pairs is not available, and so the Cooper pairs remain stable. The paired electrons have (a) equal and opposite momenta and (b) opposite spins.

Two of the main experimental facts which provided the motivations behind BCS theory are:

- (i) The density of states is gapped around the Fermi surface. This was experimentally observed in terms of exponential variation of specific heat with temperature, near critical temperature  $T_c$  [11], [12]. This led to the idea that some kind of pairing is necessary for superconductivity.
- (ii) Phonons play a major role [13]. This was experimentally demonstrated by isotope effects, as the critical temperature  $T_c$  was found to vary as the inverse square root of the nuclear mass.

Superconductors which are well explained by the framework of BCS theory or its modified forms, are commonly known as conventional superconductors or BCS superconductors. Thallium, lead are few examples of conventional superconductors.

In order to motivate the discussions of our research in high  $T_C$  superconductors (different from conventional superconductors), we consider the formalism of the BCS theory in more detail.

Let us consider a normal metallic system which undergoes a superconducting transition below certain critical temperature  $T_c$ . We will assume the system to be translationally invariant. Thus the state of an electron inside the system can be labelled by  $(\mathbf{k}, \sigma)$  where  $\mathbf{k}$  and  $\sigma$  are the electron's momentum and spin respectively. We will refer the normal metallic state as normal state, i.e. not superconducting. An electron is a spin  $\frac{1}{2}$  particle. Hence, the spin  $\sigma$  of the electron would be such that the  $z$  component of the spin is either  $+\frac{1}{2}$  or  $-\frac{1}{2}$ . The spin  $\sigma$  of the electron corresponding the first case will be denoted by  $\uparrow$  and the second case by  $\downarrow$ . We would like to know the correlation between a pair of electrons labeled by  $(\mathbf{k}, \uparrow)$ ,  $(\mathbf{k}', \downarrow)$  respectively. Up to a good approximation, the only correlation between different pairs of electrons in the normal state is just the statistical correlation in terms of the Pauli exclusion principle. Hence, the correlation function  $P_{\mathbf{k}, \mathbf{k}'}^N = \langle N | \hat{c}_{\mathbf{k}, \uparrow}^\dagger \hat{c}_{\mathbf{k}, \uparrow} \hat{c}_{\mathbf{k}', \downarrow}^\dagger \hat{c}_{\mathbf{k}', \downarrow} | N \rangle$ , will be just a smoothly varying function of  $\mathbf{k}$  and  $\mathbf{k}'$ , where  $|N\rangle$  is some normal state wave function. In case of superconducting (SC) state the correlation function  $P_{\mathbf{k}, \mathbf{k}'}^S = \langle S | \hat{c}_{\mathbf{k}, \uparrow}^\dagger \hat{c}_{\mathbf{k}, \uparrow} \hat{c}_{\mathbf{k}', \downarrow}^\dagger \hat{c}_{\mathbf{k}', \downarrow} | S \rangle$ , will also be a smoothly varying function of  $\mathbf{k}$  and  $\mathbf{k}'$  except for those cases in which  $\mathbf{k}$  and  $\mathbf{k}'$  are related to each other by some special condition—known as *pairing condition* [14]. Two electrons having their states related to each other by the pairing condition form Cooper pairs. It turns out that in the SC state, the pairing condition allows two electrons in states  $(\mathbf{k} + \frac{\mathbf{q}}{2}, \uparrow)$  and  $(-\mathbf{k} + \frac{\mathbf{q}}{2}, \downarrow)$  respectively to form Cooper pairs. From the energy minimization point of view, pairing is most favored for  $\mathbf{q} = 0$  as it corresponds to zero center of mass momentum. Hence, in the SC state, an electron in the state  $(\mathbf{k}, \uparrow)$  forms Cooper pair with another electron in the state  $(-\mathbf{k}, \downarrow)$ .

In the framework of BCS theory, the SC state is explained by a Hamiltonian operator:

$$\hat{H}_{BCS} = \sum_{\mathbf{k}, \sigma} \epsilon_{\mathbf{k}} \hat{c}_{\mathbf{k}, \sigma}^{\dagger} \hat{c}_{\mathbf{k}, \sigma} + \sum_{\mathbf{k}, \mathbf{k}'} V_{\mathbf{k}\mathbf{k}'} \hat{c}_{\mathbf{k}, \uparrow}^{\dagger} \hat{c}_{-\mathbf{k}, \downarrow}^{\dagger} \hat{c}_{\mathbf{k}', \downarrow} \hat{c}_{-\mathbf{k}', \uparrow} \quad (2.1)$$

where:

- (i)  $\hat{c}_{\mathbf{k}, \sigma}^{\dagger}$  are fermionic *creation operators*, i.e.  $\hat{c}_{\mathbf{k}, \sigma}^{\dagger}$  creates an electron with momentum and spin  $(\mathbf{k}, \sigma)$  and  $\hat{c}_{\mathbf{k}, \sigma}$  are the corresponding fermionic *annihilation operators*, i.e.  $\hat{c}_{\mathbf{k}, \sigma}$  destroys an electron with momentum and spin  $(\mathbf{k}, \sigma)$ .
- (ii)  $\epsilon_{\mathbf{k}}$  is the kinetic energy of the electron having momentum  $\mathbf{k}$  with respect to the Fermi energy  $\epsilon_{\mathbf{F}}$
- (iii)  $V_{\mathbf{k}, -\mathbf{k}}$  is interaction between two electrons via lattice deformation (i.e. *electron-phonon interaction*), which causes scattering, in which two paired electrons at initial states  $(\mathbf{k}, \uparrow)$ ,  $(-\mathbf{k}, \downarrow)$  get scattered to final states  $(\mathbf{k}', \uparrow)$ ,  $(-\mathbf{k}', \downarrow)$ , will remaining paired. Note that, this kind of interaction does not conserve the total number of particles. Hence, in principle, any number of cooper pairs can be formed in the SC state.

Now one could solve the above Hamiltonian in mean-field approximation. In order to do that let's define two parameters, namely  $\Delta_{\mathbf{k}}^*$  and  $\Delta_{\mathbf{k}}$ , such that  $\Delta_{\mathbf{k}}^* = \sum_{\mathbf{k}'} \langle V_{\mathbf{k}, \mathbf{k}'} \hat{c}_{\mathbf{k}', \uparrow}^{\dagger} \hat{c}_{-\mathbf{k}', \downarrow}^{\dagger} \rangle$  and  $\Delta_{\mathbf{k}} = \sum_{\mathbf{k}'} \langle V_{\mathbf{k}, \mathbf{k}'} \hat{c}_{-\mathbf{k}', \downarrow} \hat{c}_{\mathbf{k}', \uparrow} \rangle$ , where  $\langle \rangle$  means that expectation values of operators are taken in the ground state. The parameter  $\Delta_{\mathbf{k}}$  is known as the energy gap in the system. Now one can write,  $\sum_{\mathbf{k}'} V_{\mathbf{k}, \mathbf{k}'} \hat{c}_{\mathbf{k}', \uparrow}^{\dagger} \hat{c}_{-\mathbf{k}', \downarrow}^{\dagger} = \Delta_{\mathbf{k}}^* - \delta_1$ , where  $\delta_1 = \Delta_{\mathbf{k}}^* - \sum_{\mathbf{k}'} V_{\mathbf{k}, \mathbf{k}'} \hat{c}_{\mathbf{k}', \uparrow}^{\dagger} \hat{c}_{-\mathbf{k}', \downarrow}^{\dagger}$ . Similarly, one has  $\sum_{\mathbf{k}'} V_{\mathbf{k}, \mathbf{k}'} \hat{c}_{-\mathbf{k}', \downarrow} \hat{c}_{\mathbf{k}', \uparrow} = \Delta_{\mathbf{k}} - \delta_2$  where  $\delta_2 = \Delta_{\mathbf{k}} - \sum_{\mathbf{k}'} V_{\mathbf{k}, \mathbf{k}'} \hat{c}_{-\mathbf{k}', \downarrow} \hat{c}_{\mathbf{k}', \uparrow}$ . Now we linearize  $\hat{H}_{BCS}$ ,

considering  $\delta_1$  and  $\delta_2$  to be small. By doing the process of linearization we will keep only those terms in  $\hat{H}_{BCS}$  which are linear in  $\delta_1, \delta_2$ . Upon linearization  $\hat{H}_{BCS}$  becomes  $\hat{H}_{BCS}^{linearized}$  where:

$$\hat{H}_{BCS}^{Linearized} = \hat{H}^{Meanfield} = \sum_{\mathbf{k}} \left( \epsilon_{\mathbf{k}} (\hat{c}_{\mathbf{k},\uparrow}^\dagger \hat{c}_{\mathbf{k},\uparrow} + \hat{c}_{\mathbf{k},\downarrow}^\dagger \hat{c}_{\mathbf{k},\downarrow}) + \Delta_{\mathbf{k}} \hat{c}_{\mathbf{k},\uparrow}^\dagger \hat{c}_{-\mathbf{k},\downarrow}^\dagger + \Delta_{\mathbf{k}}^* \hat{c}_{-\mathbf{k},\downarrow} \hat{c}_{\mathbf{k},\uparrow} \right) \quad (2.2)$$

. In order to diagonalize  $\hat{H}_{BCS}^{Linearized}$ , we carry a *Bogoliubov transformation* introducing new fermionic operators  $\hat{\alpha}_{\mathbf{k},\uparrow}^\dagger$  and  $\hat{\alpha}_{-\mathbf{k},\downarrow}^\dagger$  such that:

$$\hat{\alpha}_{\mathbf{k},\uparrow}^\dagger = u_{\mathbf{k}} \hat{c}_{\mathbf{k},\uparrow}^\dagger + v_{\mathbf{k}} \hat{c}_{-\mathbf{k},\downarrow} \quad (2.3)$$

$$\hat{\alpha}_{-\mathbf{k},\downarrow}^\dagger = -v_{\mathbf{k}} \hat{c}_{\mathbf{k},\uparrow} + u_{\mathbf{k}} \hat{c}_{-\mathbf{k},\downarrow}^\dagger \quad (2.4)$$

. The anticommutation of fermionic operators gives  $u_{\mathbf{k}}^2 + v_{\mathbf{k}}^2 = 1$ . The quantities  $u_{\mathbf{k}}^2$  and  $v_{\mathbf{k}}^2$  are called *coherence factors*. And finally the Hamiltonian becomes:

$$\hat{H}^{Meanfield} = \sum_{\mathbf{k},\sigma} \left\{ \hat{\alpha}_{\mathbf{k},\sigma}^\dagger \hat{\alpha}_{\mathbf{k},\sigma} \sqrt{\epsilon_{\mathbf{k}}^2 + \Delta_{\mathbf{k}}^2} - \{ \sqrt{\epsilon_{\mathbf{k}}^2 + \Delta_{\mathbf{k}}^2} - \epsilon_{\mathbf{k}} \} \right\} \quad (2.5)$$



. In the above equation, (a) the first term gives the modified dispersion( $E_{\mathbf{k}}$ ) of the system, such that  $E_{\mathbf{k}}^2 = \epsilon_{\mathbf{k}}^2 + \Delta_{\mathbf{k}}^2$  and (b) the second terms shows that there is a net loss of energy in the pairing process. One could show that:

$$u_{\mathbf{k}}^2 = \frac{1}{2} \left\{ 1 + \frac{\epsilon_{\mathbf{k}}}{E_{\mathbf{k}}} \right\} \quad (2.6)$$

$$v_{\mathbf{k}}^2 = \frac{1}{2} \left\{ 1 - \frac{\epsilon_{\mathbf{k}}}{E_{\mathbf{k}}} \right\} \quad (2.7)$$

. It has already been mentioned that,  $\Delta_{\mathbf{k}}$  is the energy gap in the system. We can relate the gap  $\Delta_{\mathbf{k}}$  to the interaction potential  $V_{\mathbf{k},-\mathbf{k}}$  as follows:

$$\Delta_{\mathbf{k}} = \sum_{\mathbf{k}'} \left\{ 1 - 2n_F(E_{k'}) \right\} \frac{-V_{\mathbf{k},\mathbf{k}'} \Delta_{\mathbf{k}'}}{E_{\mathbf{k}'}} \quad (2.8)$$

where  $n_F(E_{k'})$  is the Fermi function, i.e.  $n_F(E_{k'}) = \frac{1}{1 + \exp(\frac{E_{k'}}{k_B T})}$ . The equation above is known as the *BCS gap equation*. By solving the BCS equation self-consistently, we can determine the energy gap in the system. There will be always a trivial solution to the BCS gap equation,  $\Delta_{\mathbf{k}'} = 0$ . In order to obtain a non trivial solution to the BCS gap equation,  $V_{\mathbf{k},\mathbf{k}'}$  needs to be negative. BCS made the following assumption about  $V_{\mathbf{k},\mathbf{k}'}$ :

$$(i) \quad V_{\mathbf{k},\mathbf{k}'} = -V_0 \text{ if } |\epsilon_{\mathbf{k}}|, |\epsilon_{\mathbf{k}'}| < \hbar\omega_D$$

$$(ii) \quad V_{\mathbf{k},\mathbf{k}'} = 0 \text{ otherwise}$$

where,  $\omega_D$  is Debye frequency. Under (a) above assumption and (b) making an approximation that only density of states around  $E_F$  i.e.  $N(E_F) = N(0)$  (since the reference level for energy is  $E_F$ ) are involved, the BCS gap equation becomes,

$$\Delta_{\mathbf{k}} = \Delta_0 = \frac{\omega_D}{\sinh[\frac{1}{N(0)V_0}]} \quad (2.9)$$

Once the interaction potential is assumed to be momentum independent,  $\Delta_{\mathbf{k}}$  becomes momentum independent, too. The momentum independent gap is  $\Delta_0$ . If one assumes that  $V_0$  is quite small, then one gets,

$$\Delta_0 \approx 2\omega_D \exp[\frac{1}{N(0)V_0}] \quad (2.10)$$

The striking feature of the above expression is that  $\Delta_0$  has an *essential singularity* at  $V_0 = 0$  and therefore results of BCS theory could have never been found treating the interaction in perturbative approach. This is one of the canonical examples where perturbation theory does not work.

## 2.4 SC order parameter

When we decrease the superconductor from high temperature  $T$  to a low temperature ( $< T_c$ ), the sample undergoes a second order phase transition at  $T = T_c$ . Different from a first order phase transition, in which the order parameter changes discretely, in a second order phase transition the order parameter changes continuously at the transition  $T_c$ . It turns out that one can choose the superconducting order parameter as a complex scalar function. Hence the superconducting order parameter has (a) a magnitude and (b) a phase. Magnitude of

the complex order parameter is proportional to the gap size  $\Delta_0$  and the phase of the order parameter embodies the fact that the system behaves like one giant condensate below  $T_c$ . One could write the order parameter as  $\Delta_0 \exp(i\theta)$ . We have already known that  $\Delta_0$  is momentum independent, and the phase  $\theta$  of a conventional superconductor is momentum independent as well. Such an order parameter for conventional superconductor is called as *s-wave order parameter* and the symmetry of the order parameter is called *s-wave symmetry*. One could use the BCS gap equation to find out how the superconducting gap, and hence the magnitude of the order parameter, changes as a function of temperature through  $T_c$ . From the BCS gap equation one can get:

$$\Delta_{T \rightarrow 0} = 1.76 k_B T_c \quad (2.11)$$

$$\Delta_{T \rightarrow T_c} \sim 3.2 k_B T_c \left\{ 1 - \frac{T}{T_c} \right\}^{\frac{1}{2}} \quad (2.12)$$

. There are two lessons to learn from these equations—(a) superconducting gap at  $T = 0$  is directly proportional to  $T_c$  and (b) as  $T \rightarrow T_c$  superconducting gap approaches zero in a meanfield fashion. In Fig. 3, we show how the SC gap changes as a function of temperature.

## 2.5 High Temperature(High $T_c$ ) Superconductor

Because superconductors have many unique properties and potential applications in a number of areas, people are continuously trying to discover superconducting materials with higher  $T_c$ . In spite of a lot of effort, the highest  $T_c$  remained around 20K for couple of decades. By

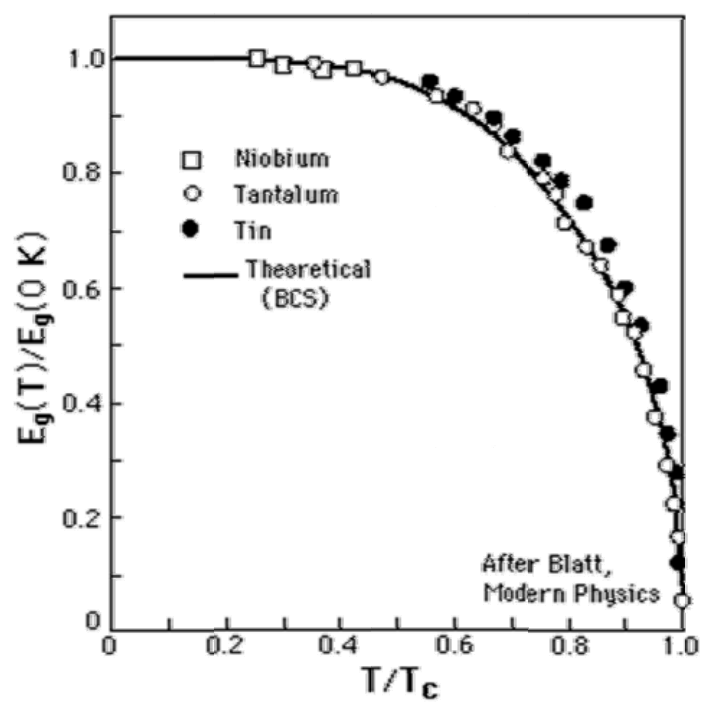


Figure 3. Temperature dependence of SC gap

1970, almost all the existing theoretical issues regarding superconductivity were understood by the BCS theory and the Ginzburg-Landau theory. Therefore, many people thought it is quite the dead end for research in the field of superconductivity. But in 1986, an astonishing discovery brought a real breakthrough in the field of superconductivity research. Two researchers Benoraz and Muller from IBM in Switzerland, discovered a new class of superconductors starting with LaBaCuO, whose  $T_c$  could be as high as 30K [15] . The following year, a new record in  $T_c$  was set in terms of the discovery of another superconductor  $\text{YBa}_2\text{Cu}_3\text{O}_{7+\delta}$ , superconducting at 90K [16]. Soon a whole new series of related materials, e.g.  $\text{Bi}_2\text{Sr}_2\text{Ca}_n\text{Cu}_{n+1}\text{O}_{6+2n+\delta}$  (BISCO – 2201, –2212, –2223),  $\text{Tl}_2\text{Ba}_2\text{Ca}_n\text{Cu}_{n+1}\text{O}_{6+2n+\delta}$ ,  $\text{HgBa}_2\text{Ca}_n\text{Cu}_{n+1}\text{O}_{2n+4+\delta}$  (Hg-1201, -1212, -1223) and so on, were found. Collectively all these new classes of materials are called High Temperature Superconductors (HTSC), because the  $T_c$ 's of these materials are much higher than that of conventional superconductors. A history of the increase in  $T_c$  is shown in Fig. 4 . In the following sections, we will briefly discuss some topics of the fascinating physics of the HTSCs. Details can be found in large volume of literature available on the subject, for example [17], [18],[19], [20], [21], [22].

Superconductivity in HTSC materials is really different for conventional superconductivity for different reasons.

- (i) Before these materials, there was no known case of superconductivity in oxide materials.
- (ii) The parent compounds for all these materials are Antiferromagnetic insulators. On the contrary, conventional superconductors are metallic in normal state, at least not insulating.

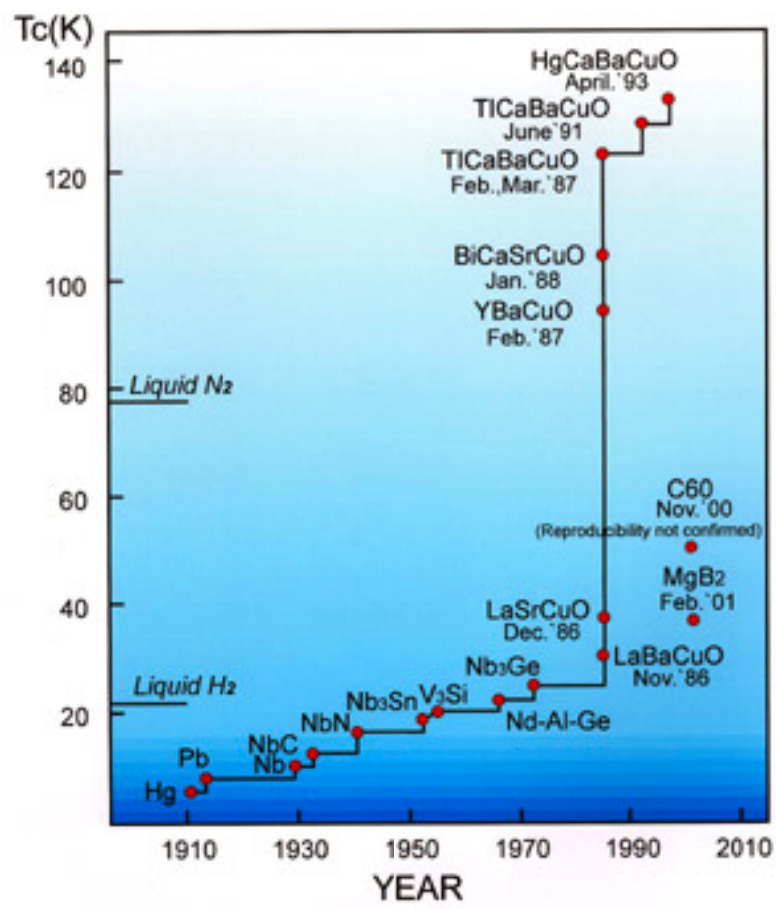


Figure 4. History of discovery from Superconductor to of higher  $T_c$  Superconductor

- (iii) Conventionally, magnetism and superconductivity do not go together. For example in their pioneering work, Abrikosov and Gorkov showed that the presence of magnetic impurities in conventional SC system destroys superconductivity.[23], [24].
- (iv) With  $\delta$ -doping and temperature changing, the HTSC material will experience many different phases,(i.e antiferromagnetic, pseudogap, strange metal, superconducting, conventional metal). And those phase, which are key to HTSC study, are still not well understood.

Hence, even without going into details, one could easily tell that the physics of superconductivity in HTSC materials is quite different from the ones in conventional superconductors. All these astonishing physics of HTSC materials attract an enormous amount of research efforts in this field during the last two decades, but even today the physics of superconductivity in HTSC materials is not completely understood.

## **2.6 Common features among different HTSC materials**

There are very wide variety of materials which are high temperature superconductors. Hence the first step in the process to understand HTSC is to look for common features, if there are any. All these materials, irrespective of having very different chemical composition, share quite a large number of common features, such as:

- (i) All of them have layered perovskite crystal structures containing one or more  $\text{CuO}_2$  planes separated by block layers. Hence, in general these materials are called cuprates. It is commonly believed that the universal physics behind superconductivity in HTSC should be related to the properties of the  $\text{CuO}_2$  planes.

- (ii) The basic features of the phase diagrams for all of them are similar. We will discuss this in later section.
- (iii) Generic features of the electronic structures for example superconducting state, pseudogap state, strange metal state of them are also very similar.

In the following sections we will briefly discuss the common feature among cuprates.

## 2.7 Crystal Structure

The crystallography of the HTSC is by itself a complicated research field. All the work presented in this thesis was carried out on  $\text{Bi}_2\text{Sr}_2\text{CaCu}_2\text{O}_{8+\delta}$  (Bi2212), therefore we discuss the crystal structure of Bi2212 only. In order to make a comparison, we show crystal structures of two other families of HTSC, in Fig. 5. By looking at Fig.5, one can see that all of these different HTSC materials have very anisotropic crystal structures, and one or more  $\text{CuO}_2$  planes that are separate from each other by charge reservoir layers. For instance, there are  $\text{Bi}_2\text{Sr}_2\text{CuO}_{6+\delta}$  (Bi2201),  $\text{Bi}_2\text{Sr}_2\text{CaCu}_2\text{O}_{8+\delta}$  (Bi2212),  $\text{Bi}_2\text{Sr}_2\text{Ca}_2\text{Cu}_3\text{O}_{10+\delta}$  (Bi2223) one, two and three  $\text{CuO}_2$  layers in the unit cell, respectively. Collectively, all these Bi based HTSC materials are known as BISCO. The layers are called reservoir layers because usually they remove electrons from  $\text{CuO}_2$  layer, they are insulating and have no contribution to the low energy electronic excitations. Typically in BISCO systems, the bonding between two BiO unit cells layers is the quite weak Van-der-Waals interaction. Hence, it is easy to cleave BISCO samples and BiO layer emerges as the topmost layer in each piece. In Fig. 5c we can see that the orthorhombic unit cell of Bi2212 has lattice parameters  $a = 5.4, b = 5.4, c = 30.7\text{\AA}$ . This is an extremely tall unit cell. However, the structure in the figure is not the real structure. The BiO layer is distorted



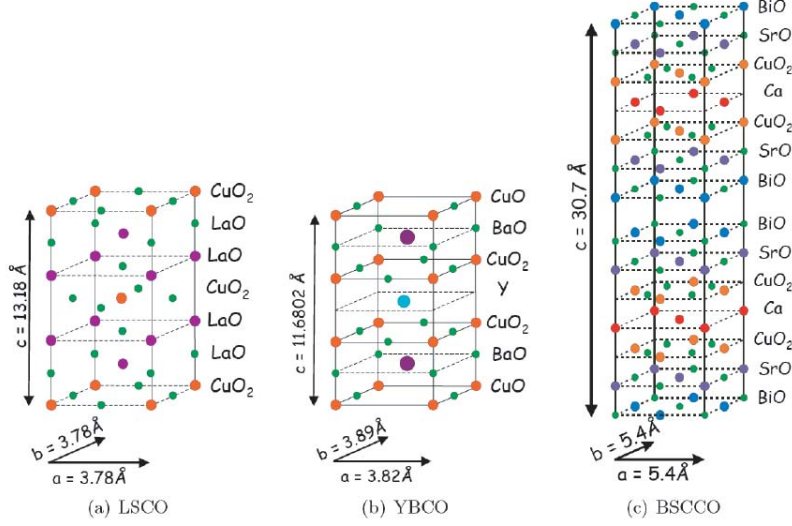


Figure 5. Crystal Structure for three different families of HTSC materials.

(a)  $\text{La}_{2(1-x)}\text{Sr}_2\text{CuO}_4$ , (b)  $\text{YBa}_2\text{Cu}_3\text{O}_{7+\delta}$ , (c)  $\text{Bi}_2\text{Sr}_2\text{CaCu}_2\text{O}_{8+\delta}$

with an incommensurate wave vector directed along the  $b$  direction. The periodicity along the  $b$  direction is about  $27\text{\AA}$ . The actual structure is obtained by displacing atoms primarily perpendicular to the BiO plane, but there is some displacement of all other atoms as well. This distortion is called superlattice, because it induces replica of excitation of the  $\text{CuO}_2$  planes. Effects of the superlattice can be seen in spectroscopy experiments.

## 2.8 The parent compound

In contrast to conventional superconductors, the undoped parent compounds for all high temperature superconductors are insulators. And unlike the conventional metallic superconductor, we can dope the HTSCs by either removing or adding electrons to the  $\text{CuO}_2$  planes and

these will change the properties of the materials, and as the outcome the materials show some special characteristics. Superconductivity originates in the  $CuO_2$  planes and therefore we will only consider the electronic structure of the  $CuO_2$  planes. The active energy states which are close to the Fermi energy are the Cu  $3d_{x^2-y^2}$  electrons of Cu hybridized with the O  $2p$  electrons. Cu is divalent with electronic configuration  $d^9$ . Among all 9  $d$  electrons, only one needs to be considered active for explaining low energy properties of the system. Because of crystal field splitting and Hund's rules, the other states are fully occupied and do not participate in conductivity. For example let's consider the high temperature superconductor  $La_{2(1-x)}Sr_xCuO_4$  which has the simplest crystal structure among all HTSC. The parent compound for this material would correspond to  $x = 0$ — $La_2CuO_4$ . In  $La_2CuO_4$ , Cu is divalent, ie, Cu is in the  $d^9$  configuration. Hence there is one  $d$  electron per unit cell. The system should be a metal, as from standard band theory, that any crystal with odd number of electrons per unit cell has an incompletely filled band of electronic states. But, in fact, this material is a very good insulator. This kind of insulator is known as a Mott insulator. A Mott insulator is qualitatively different from a conventional band insulator. In a band insulators, the conductivity is blocked by a band gap. Electrons cannot move because all orbitals are filled. On the other hand, for a Mott insulator, the conductivity is inhibited by repulsion between electrons. When the highest occupied state has one electron per atom, the creation of a doubly occupied site is required for electron motion. The electron motion is blocked if the Coulomb repulsion between electrons is very strong. Hence a Mott insulator is a direct consequence of local correlations between electrons in the system.

## 2.9 Doping the parent compound

In the last section we have seen that the parent compounds of the HTSC are Mott insulators. Now if we consider the spin degrees of freedom of electrons, because of various possible orientations of electronic spins with respect to each other, there should be a huge degeneracy in ground state. But it turns out that the system condenses in a unique ground state, the antiferromagnetic state. By removal of some of the electrons, the antiferromagnetism is destroyed, and depending on the amplitude of charge removal, these materials exhibit spectacularly different phases. As electrons are removed, holes are created. Electrons are able to move by hopping into the unoccupied holes. An electron hopping into a hole is equivalent to a hole moving into an electron site, so the holes become charge carriers in the system. The dynamic process of changing carrier concentration in the system is called doping. Operationally, doping in these materials can be done in various ways such as:

- (i) by adding oxygen interstitially (e.g.  $\text{Bi}_2\text{Sr}_2\text{CaCu}_2\text{O}_{8+\delta}$ )
  - (ii) by substituting a monovalent atom with a trivalent atom (e.g. by replacing La with Sr in  $(\text{La}_{2(1-x)}\text{Sr}_2\text{CuO}_4)$ )
  - (iii) by removing oxygen atoms from their corresponding stoichiometric positions (e.g.  $\text{YBa}_2\text{Cu}_3\text{O}_{7+\delta}$ )
- and so on.

All these different processes of removing electrons to create holes in the  $\text{CuO}_2$  planes are called hole doping. On the other hand there are other materials which can be doped by adding electrons

to the  $CuO_2$  planes. These materials are known as electron doped materials. In this thesis we will not discuss electron doped materials.

Fig. 6 shows a schematic phase diagram of the hole doped HTSCs. The parent material (i.e.  $\delta = 0$ ) are antiferromagnetic insulators with Neel temperature of the order of  $300K$ . As doping increases, the antiferromagnetism is destroyed very quickly and the system starts to become a conductor. But this conducting phase is very different from the metallic state in conventional metals. This phase has many unusual properties, and it is rather poorly understood. It is called the pseudogap phase. With further increase in doping the conducting phase becomes Fermi liquid like, close a usual metal. At low temperatures, for  $0.07 < \delta < 0.25$ , (for  $Bi_2Sr_2CaCu_2O_{8+\delta}$ ), the system becomes superconducting. The maximum  $T_c$  is achieved for  $\delta \sim 0.15$ , known as optimal doping. As shown in Fig. 6, there is another new phase in the conducting state, in between the so called pseudogap phase and the conventional Fermi-liquid like phase and at higher temperature, called the strange metal phase. As the name states, even now we do not have any proper understanding of the underlying physics for the strange metal phase. Especially the regime right above the superconducting dome and in between the pseudogap, conventional metal and strange metal phase. Fig. 7 shows the  $T_c$  versus hole doping of HTSCs. For  $\delta = 0.07$  at low temperature, the system become superconducting. With doping increase, the  $T_c$  increase till  $\delta = 0.15$  when it reaches its highest value. For further increase in doping,  $T_c$  decrease till  $\delta = 0.25$ , and then the system become metallic.

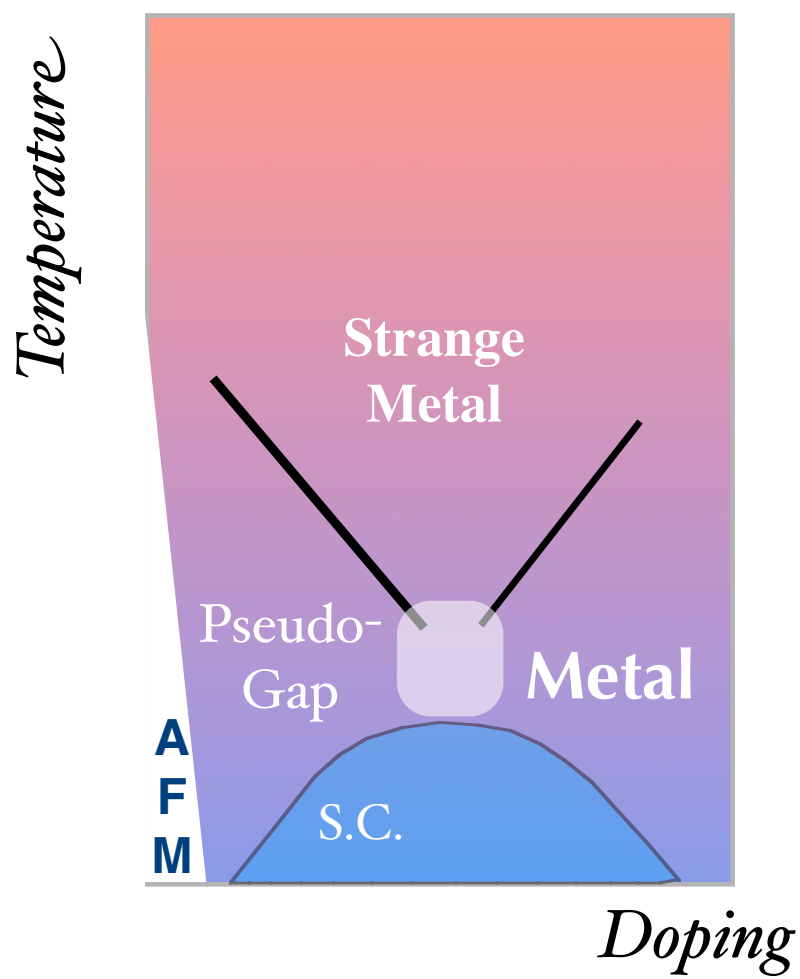


Figure 6. Phase diagram of hole doped cuprates

### 2.10 Pseudogap Phase

The pseudogap (PG) state and the strange metal state (Fig. 6) [17], [25], [26] are poorly understood. Here we will discuss only about the PG state. There is a partial suppression of the low energy excitations in the PG state. As low energy excitations are not completely suppressed there is a partial energy gap opens up in the excitation spectrum of the PG state. Unlike the SC state, in the PG state the energy gap is not a hard gap hence it is called pseudogap. Both spin and charge excitations are partially gapped in the PG state. In certain cases, the system could develop the PG even at a temperature of the order of couple of hundred kelvin. The temperature below which the PG starts to appear is called as  $T^*$ . Unlike  $T_c$ ,  $T^*$  does not define a well defined phase transition, rather  $T^*$  is associated with some cross over. Pseudogap effect was first observed in Inelastic Neutron Scattering (INS) experiment. After that pseudogap effect has been found in static magnetic susceptibility, Knight Shift, Hall effect, AC conductivity, specific heat and ARPES experiments [27], [28], [29], [30], [25]. It is important to know that in all of these experiments, pseudogap effect is always associated with a characteristic temperature  $T^*$  but the actual value of  $T^*$  which obtained in different experiments for the same sample, could be quite different from each other. But all these experiments share one feature in common—with decrease in doping in the underdoped side  $T^*$  increases. Quite surprisingly,  $T^*$  and  $T_c$  are not related to each other in any obvious way.

The result of transport measurements in the PG state are quite surprising. As HTSCs have layered structures, one can measure both their in-plane and the out-of-plane resistivity. The in plane resistivity, commonly known as the  $ab$  plane resistivity ( $\rho_{ab}$ ), and out of plane

resistivity, commonly known as the c axis resistivity ( $\rho_c$ ), show qualitatively different properties as sample-temperature  $T$  is changed. Generally for metals resistivity goes down as  $T$  decreases. And resistivity in insulators grows exponentially as  $T$  goes down. At higher temperatures ( $T \gg T^*$ ), both  $\rho_{ab}$  and  $\rho_c$  decrease as  $T$  decreases. Hence, qualitatively both  $\rho_{ab}$  and  $\rho_c$  show metallic behaviors at higher temperatures. But as  $T \rightarrow T^*$  temperature dependence of  $\rho_{ab}$  starts to look different from that of  $\rho_c$ . As  $T$  becomes lower than  $T^*$ ,  $\rho_c$  exhibits insulating behavior, although  $\rho_{ab}$  always shows metallic behavior. With further decrease in  $T$ , at  $T_c$  the sample undergoes superconducting phase transition and becomes a three dimensional superconductor. Hence it might be quite tempting to conclude that, in the PG state, HTSCs are metallic in plane but insulating out of plane. But in order to determine whether some system behaves like a conventional insulator, one needs to find out whether the resistivity of the system grows exponentially as  $T$  goes down. It turns out that in between  $T^*$  and  $T_c$ , as  $T$  is decreased  $\rho_c$  grows monotonically but never grows exponentially. So strictly speaking even in between  $T^*$  and  $T_c$ ,  $\rho_c$  does not show insulating behavior. By doing transport measurements, at the presence of high magnetic field, one can probe the PG state at very low temperatures as superconductivity gets suppressed by magnetic field. Such field-dependent measurements show that at low temperatures  $\rho_{ab}$  goes down as  $T$  goes down and finally gets saturated to some residual value, but  $\rho_c$  always grows monotonically. Considering all these results, we can say HTSCs are metallic in the plane but neither metallic nor insulating along c axis.

The ratio between  $\rho_c$  to the  $\rho_{ab}$  is pretty large—of the order of couple of thousands as  $\rho_{ab}$  is of the order of couple of hundred  $\mu\Omega\cdot\text{cm}$  and  $\rho_c$  is of the order of couple of  $\Omega\cdot\text{cm}$  for

samples in the PG regime. In order to appreciate the different properties between c axis and ab-plane resistivity, let's introduce the concept of Mott maximum resistivity ( $\rho_{max}$ ). Electrical resistivity in a system has a natural quantum scale, corresponding to the mean free path ( $l$ ) of current relaxing collisions becoming short enough to equal to DeBroglie wave length( $\lambda_{DB}$ ) which is of the order of the lattice constants. When the resistivity of a system approaches  $\rho_{max}$ , electrical conduction process changes from random scattering of propagating electrons to that of hopping or localized electrons. For c axis transport,  $\rho_{max} \sim m\Omega \cdot \text{cm}$  which is couple of hundred times smaller than  $\rho_c$ . In terms of mean free path for electrons,  $\rho_{ab}$  corresponds to around 10 lattice spacing, whereas  $\rho_c$  corresponds to around 0.01 lattice spacings! It means somehow, electronic states are extended in ab plane but localized in the c direction. This is almost impossible to understand in terms of disorder-dominated electronic propagation along c axis. In order to compare the unconventional physics in the normal state of cuprates with conventional metallic state, we will simply discuss about Landau's fermi-liquid theory(FL), one of the most important foundations of modern condensed matter physics. Let's assume that we have an interacting system to deal with. In general, in order to treat the system quantum mechanically one needs to deal with the full Hamiltonian and hence to take into account of all the interactions between all the particles in the system. As long as the number of particle becomes larger than two, there is no way to treat the problem exactly. Even with the most powerful computer in the world, it is not possible to take into account of the interactions between particles in a macroscopic interacting system. As a remedy, Landau came up with an effective theory, known as Fermi-liquid (FL) theory. The essential ingredients of FL theory



is that if (a) the interaction is not too strong and (b) the system does not go through phase transition, interaction between electrons lead to only quantitative changes in the system—no qualitative change happens to the interacting system compared to the non interacting ones. For example the mass of electrons get renormalized to some effective mass in the interacting system and the interacting system still can be treated as a collection of non interacting particles—only with different effective mass. Such renormalized particles are called *quasiparticles*. As a result, one can exam excitations of electrons in the non-interacting system with one-to-one correspondence to the ones of quasiparticles in the inetarcting system. By using this powerful theory, one can calculate various attributes of a system which obeys FL theory. These results are quite general and they do not depend upon the specifics of the system—e.g electronic specific heat as a function of temperature shown linear behavior, magnetic susceptibility is constant, scattering( $\Gamma$ ) as a function of energy( $\omega$ )/Temperature( $T$ ) goes as  $(\omega^2)/T^2$  and so on. FL theory has spectacular success in understanding regular standard solid-state systems, e.g. conventional metals, band insulators, semiconductors. Hence whenever FL theory breaks down for a system, some kind of unconventional physics is needed to understand it. Theoretically, to do controlled calculation in the framework of non fermi liquid behavior is always a tough challenge.

In conventional case, resistivity in metals are due to scattering of electrons with some kind of excitations, such as phonons . Therefore, if the excitations have some characteristic energy scale ( $\omega_0$ ), the resistivity would depend on some higher power of  $T$  for  $k_B T \leq \hbar \omega_0$  and linearly with  $T$  for  $k_B T \geq \hbar \omega_0$ . Hence there is some kind of a crossover temperature in the temperature dependence of  $\rho$  in standard FL systems. But in the PG state over a huge temperature range,

$\rho_{ab} \sim T$  which is a clear violation of standard FL theory. Unlike FL systems, the absence of a crossover temperature in the temperature dependence of resistivity for HTSC materials in the PG state, implies that excitations in the system have zero energy scale. This fact motivated people to bring forward the concept of quantum critical point as the underlying Physics for pseudogap phenomenon in HTSCs. In the quantum critical point scenario, some hidden order is associated with the PG state and until now no body knows how to detect such hidden orders experimentally. In addition the fact that  $\frac{d}{dT}(\rho_{ab})$  does not depend upon  $T_c$ , implies that whatever process causes the resistivity in the plane does not depend upon  $T_c$ .

For regular metals the fermi surface forms closed contours. But ARPES experiment shows that in the PG state there is disconnected fermi surface which continuously expand with temperature increase into a complete fermi surface only above  $T^*$ . This kind of disconnected fermi surface is known as fermi arc. Until now no body knows the underlying Physics behind the formation of fermi arc [31].

All of these unconventional properties of PG state make the Physics of Pseudogap state very complicated and as well very interesting. Hence it is quite naturally believed, that one of the major reasons for the absence of a microscopic theory for superconductivity in HTSC materials, is lack of our understanding of the underlying physics in the PG state. If we can understand the normal state of HTSCs, especially the PG state, it will be quite possible that we can crack the natures behind the superconductivity of HTSCs.

In the later chapter we will discuss about the PGs in more details. Specifically the  $T^*$  line, the region right above the superconducting dome, and the low temperature PG states as there is little spectroscopic data about it.

### 2.11 Superconducting state

In the last section, we have discussed, about various abnormal properties in the so called normal state of HTSC materials. But as the system goes to SC state, some sort of sanity comes into existence, in the sense that HTSCs share same macroscopic underlying properties with conventional superconductors—perfect diamagnetism and perfect conductivity. But there are certain striking differences between SC state in the conventional superconductors and that in HTSC [17]. Below we will glance through a few of them:

- (i) The most striking contrast between the SC state in HTSCs and that in the conventional superconductors, is in terms of momentum anisotropy in SC order parameter. In HTSC, the SC order parameter has huge anisotropy in momentum space—both amplitude and phase vary strongly with momentum. Superconducting gap ( $\Delta_{\mathbf{k}}$ ) for HTSC materials has the form,  $\Delta_{\mathbf{k}} = \frac{\Delta_{max}}{2} \left\{ \cos(k_x) - \cos(k_y) \right\}$ , where  $\mathbf{k} = (k_x, k_y)$ . Because of this specific form of superconducting gap, it vanishes exactly at four points on the Fermi surface—known as nodes. In ARPES experiment one can not see the phase of the order parameter. But in Josephson interference experiments, one can clearly see that phase of the superconducting order parameter varies and really changes sign. Such order parameters are known as d-wave order parameters and the symmetry of the order parameter is called as d-wave symmetry. In conventional superconductors, order parameter has

s-wave symmetry. The existence of an anisotropy of the order parameter in HTSC materials, is most probably directly related to the anisotropy in electronic structure and to the anisotropy in the interaction as well.

- (ii) Like BCS superconductors, a HTSCs also have cooper pairs. Typically the coherence length( $\xi$ ) is a measure of the extent Cooper pairs. For a clean, conventional superconductor,  $\xi = \frac{\hbar v_F}{k_B T_c}$ , where  $v_F$  is the velocity of electrons at the Fermi level. For regular BCS superconductors, coherence length is of the order of  $1000A^0$ . For HTSCs, one can define the in plane coherence length( $\xi_{ab}$ ) and the out of plane coherence( $\xi_c$ ). In the zero temperature limit  $\xi_{ab}$  is of the order of  $15A^0$ , whereas  $\xi_c$  is of the order of  $3A^0$ . It is worth mentioning  $\xi_c$  is smaller than the smallest relevant length scales along the c axis, namely the interlayer spacing( $d$ ), where  $d \sim 7A^0$  for single layer compounds(one  $CuO_2$  plane per unit cell) and  $d \sim 12A^0$  for bilayer compounds(two  $CuO_2$  planes per unit cell).
- (iii) Like conventional superconductors the HTSCs also show the meissner effect. HTSCs are type two superconductors. In the context of meissner effect, an important parameter is the London penetration depth( $\lambda_L$ ) which basically measures the distance over which magnetic field can penetrate the sample. Without taking into account of non-local effects, one could write  $\lambda_L = \sqrt{\left\{ \frac{mc^2}{4\pi n_s e^2} \right\}}$ . For HTSC, could define penetration depth associated with ab plane and c axis as  $\lambda_L^{ab}$  and  $\lambda_L^c$  respectively. Typically for conventional superconductors,  $\lambda_L \sim 500A^0$ . On the other hand  $\lambda_L^{ab} \sim 1500A^0$  and  $\lambda_L^c$  can be even much higher.
- (iv) It is mentioned previously, that in case of conventional superconductors, one can successfully use the two fluid model to explain many properties in the superconducting state. In

zero temperature limit, for a clean BCS superconductor,  $n_s = n$  where  $n_s$  is the superfluid density and  $n$  is total electron density in the system. It basically implies that in the zero temperature limit, all the electrons become super electrons in the superconducting state for conventional superconductors. Now for HTSC, one can think of doping( $\delta$ ) as the analog of  $n$ . Now using Uemura's empirical relation one could relate superfluid density( $n_s$ ) to the doping( $\delta$ ) of a HTSC sample, at least in the underdoped side. It turns out that for HTSCs, in the underdoped side  $n_s < \delta$ . Most likely this means that unlike regular superconductors, or HTSCs (at least in the underdoped side) the phase of the order parameter is not very rigid—rather the phase is soft.

- (v) In conventional superconductors,  $\Delta \sim T_c$ . But in case of HTSCs, atleast in the underdoped side, there is no such obvious relation between  $\Delta_{\mathbf{k}}$  and  $T_c$ . Quite surprisingly in the underdoped side, as  $\delta$  is decreased  $\Delta_{\mathbf{k}}$  goes up but  $T_c$  goes down.
- (vi) Unlike conventional superconductors, quite generically for all HTSC materials, collective modes related to magnetic excitations, appear in the superconducting state. There is a huge debate in literature whether this collective mode is a cause or effect of superconductivity in HTSC materials.

Above, we mention a few among many many unusual properties of the SC state in HTSCs. Until now the mechanism of superconductivity in HTSCs is an unsolved riddle.

## CHAPTER 3

### EXPERIMENTAL TECHNIQUES:ANGLE RESOLVED PHOTOEMISSION

This chapter is a brief introduction to angle resolved photoemission (ARPES), a leading and direct method of studying the electronic structure of solids. The main goals of this thesis is to understand the excited states of electrons in the high temperature superconductors

#### 3.1 Basics of Photonemission Spectroscopy

Photoemission Spectroscopy(PES) is a general term which refers to set of experimental techniques that are based on the photoelectric effect. The photoelectric effect was originally observed by Frank and Hertz in 1887 and subsequently Einstein [32] came up with his famous quantum treatment of electromagnetic radiation to explain it. The technique of photoemission spectroscopy has been used extensively in a range of fields, starting from Atomic Physics to surface science, to chemistry, to Solid State Physics, with completely different perspectives. In this thesis we will confine our discussion about the technique in the context of Solid State physics . The idea behind the photoemission process is quite simple. The light shines on the sample, electrons in the sample absorb the photons and are emitted from the sample. Let us consider a solid sample. Assume that the sample is hit by a photon of energy  $h\nu$  and an electron

that has binding energy  $E_B$ , with respect to the Fermi level ( $E_F$ ), absorbs the photon and escapes from the sample. Then conservation of energy leads to,

$$E_{kin} = h\nu - E_B - \phi \quad (3.1)$$

where  $\phi$  is the work function for the sample of interest,  $E_{kin}$  is the kinetic energy of the emitted electron. The work function is the energy required for an electron to reach the surface of the material from the Fermi level, i.e.  $\phi = E_{vac} - E_F$ . In experimental set ups, both the sample and electron energy analyzers are electrically connected and hence the kinetic energy of the electrons is measured with respect to  $E_F$ . Therefore one can rewrite the above equation as,

$$E_{kin} = h\nu - E_B \quad (3.2)$$

where  $E_{kin}$  is the kinetic energy of the emitted electron with respect to  $E_F$ . Hence, by measuring kinetic energy of the emission electron one can obtain the energy of the electron inside the solid. This is the working principle for Fig 7, which shows how one can relate the energy distribution of a photo emitted electron to the energy-levels inside the solid. For this case, the fermi energy  $E_F$  is at the top of the valence band whose minimum is  $E_0$  such that the difference between  $E_0$  and vacuum level  $E_V$  is  $V_0 = E_B + \phi$ . If photoabsorption takes place in a core level with binding energy  $E_B$  ( $E_B = 0$  at  $E_F$ ), photoelectrons can be detected with kinetic energy  $E_{kin} = h\nu - E_B - \phi$  in the vacuum. Inside the solid the reference level is  $E_F$ , whereas outside the reference level is  $E_{vac}$ .

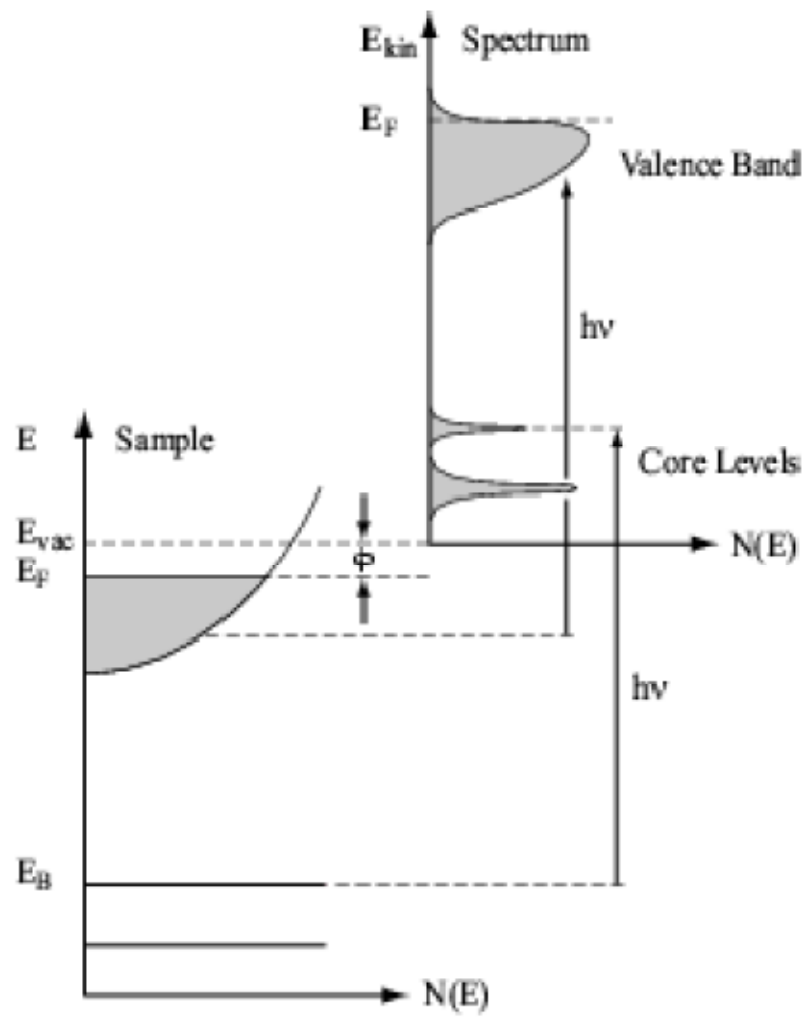


Figure 7. Energetics of the photoemission process



### 3.2 Energetics of Angle Resolved Photoemission Spectroscopy

Angle Resolved Photoemission Spectroscopy (ARPES) is PES, with addition that the direction of emission of the electron is also measured. A beam of monochromatized radiation supplied either by a gas-discharge lamp or by a synchrotron beamline is incident on a sample. Electrons escape into the vacuum in all directions. By collecting the photoelectrons with an electron energy analyzer characterized by a finite acceptance angle, one measures the kinetic energy  $E_{kin}$  of the photoelectrons for a given emission angle. Once the kinetic energy  $E_{kin}$  of the electrons and angle of emission (polar angle  $\theta$ , azimuthal angle  $\phi$ ) of the electron with respect to the normal to sample surface are known, the momentum( $\mathbf{p}$ ) or wave vector( $\mathbf{K}$ ) of the photoelectron is also known. Quite generally  $\mathbf{K}$  can be written as  $\mathbf{K}=(\mathbf{K}_{||}, \mathbf{K}_{\perp})$ , where  $\mathbf{K}_{||}=(\mathbf{K}_x, \mathbf{K}_y)$  and  $\mathbf{K}_{\perp}=\mathbf{K}_z$  correspond to the components of wave vector parallel and perpendicular to the sample surface respectively. A typical geometry for an ARPES experiment is shown in Fig. 8 and for this geometry one could write:

$$K_z = \sqrt{\frac{2mE_{kin}}{\hbar^2}} \cos(\theta) \quad (3.3)$$

$$K_x = \sqrt{\frac{2mE_{kin}}{\hbar^2}} \sin(\theta) \cos(\phi) \quad (3.4)$$

$$K_y = \sqrt{\frac{2mE_{kin}}{\hbar^2}} \sin(\theta) \sin(\phi) \quad (3.5)$$

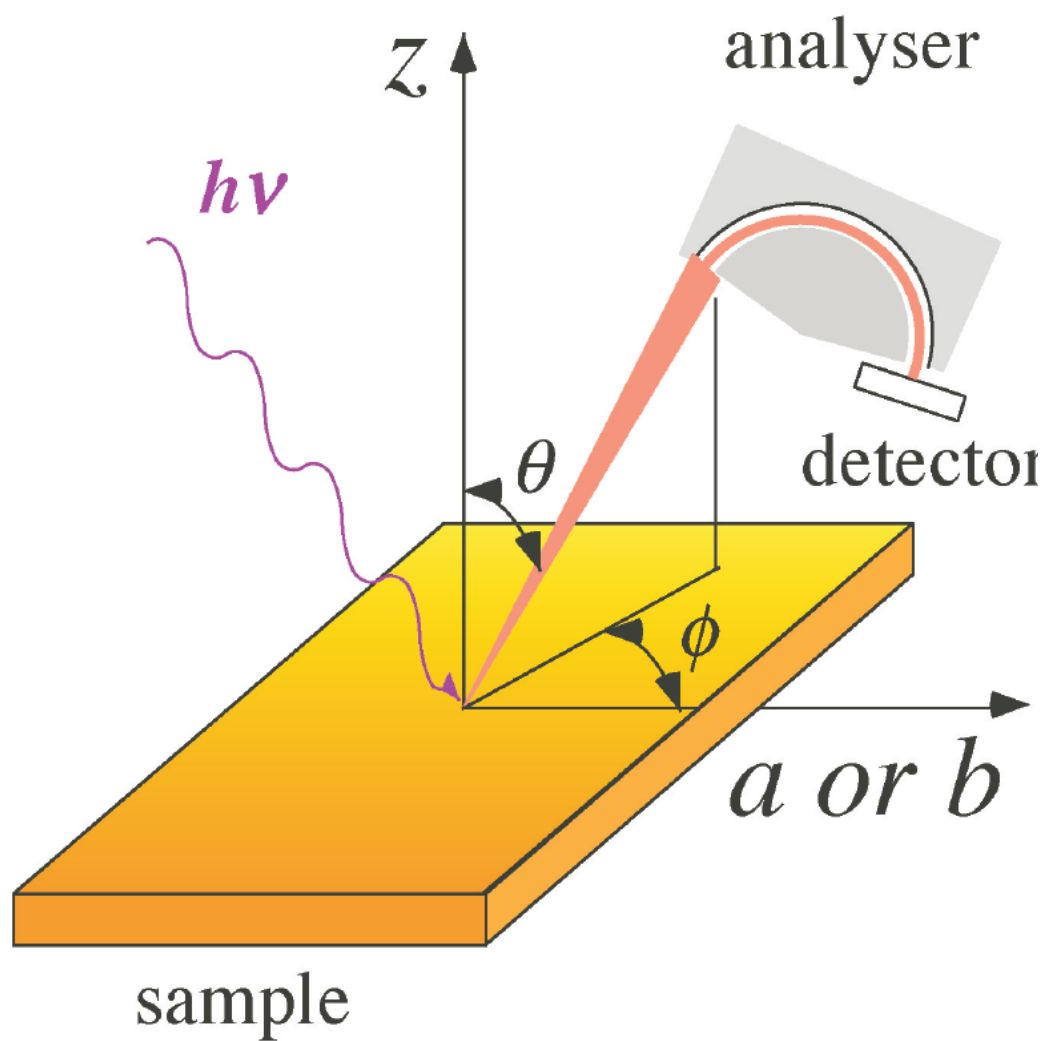


Figure 8. Mechanism of ARPES experiment

These relation give us a direct relation between energy, and momentum of electrons in the sample, provided we know how to relate the momentum and energy of the photoemitted electron to those of the electronic state inside the solid. For most experiments ultraviolet light is used as the impinging radiation and hence one can neglect the momentum associated with the electromagnetic radiation. For a real three dimensional system it is quite non-trivial to relate the momentum  $\mathbf{K}$  of the photoemitted electron to the momentum  $\mathbf{k}$  of a state inside the system, since  $\mathbf{k}_z$  is conserved only to a reciprocal lattice vector at the surface, because the solid differs from the bulk at the surface. But for a translationally invariant quasi-two-dimensional system  $\mathbf{k}_z$  is irrelevant and  $\mathbf{k}_{||}=(\mathbf{k}_x, \mathbf{k}_y)$  is conserved. For such systems one could simply relate  $E = -E_B$  and  $\mathbf{k}$  (the attributes of the electronic state inside the system) with  $E_{kin}$  and  $\mathbf{K}$  which are measured kinetic energy and momentum of photoelectron, as follows:

$$E = E_{kin} - h\nu \quad (3.6)$$

$$k_x = K_x = \sqrt{\frac{2mE_{kin}}{\hbar^2}} \sin(\theta) \cos(\phi) \quad (3.7)$$

$$k_y = K_y = \sqrt{\frac{2mE_{kin}}{\hbar^2}} \sin(\theta) \sin(\phi) \quad (3.8)$$

Hence ARPES gives direct information about the relation between  $E$  and  $\mathbf{K}$  for electronic states inside the system. The high temperature superconductors which we study are translationally periodic quasi-two-dimensional systems. Thus for our systems of interest, the above

simple minded formulation. In Fig. 9 we show how one can implement this formulation to find the energy-momentum relations inside a physical system using ARPES.

### 3.3 Spectral Function formalism of ARPES data

In order to connect ARPES data with some important microscopic attributes of the system, we use a formal description of the photoemission process. As we discussed previously the photoemission process is associated with the removal of an electron from the system. Let us consider a system that it has  $N$  electrons initially. Then after one of the electrons is removed there are  $(N - 1)$  electrons left. The initial state (i.e the state at which the electron was not emitted from the system) is one of the  $N$  particle bulk Bloch eigen states. The final state of the system together with the photoemitted electron, is basically a combination of one of the  $(N - 1)$  particle bulk Bloch eigen states and the wave function of the emitted electron. Hence the exact treatment of the process will be to figure out how the system goes from the initial state to the final state in the presence of proper boundary condition at the surface. However, due to the complexity of looking at the whole process as a one step process [33], [34]. With the impulse approximation, which assume that the outgoing photo-electron is moving so fast that it has no time to interact with the photo-hole, one can take some phenomenological approach in which the whole process is composed of three sequential steps:

- (i) optical excitation of the solid in the bulk, i.e the transition of the bulk from its initial state to its final state,
- (ii) Travel of the excited electron to the surface.
- (iii) Escape of the photonelectron into vacuum.

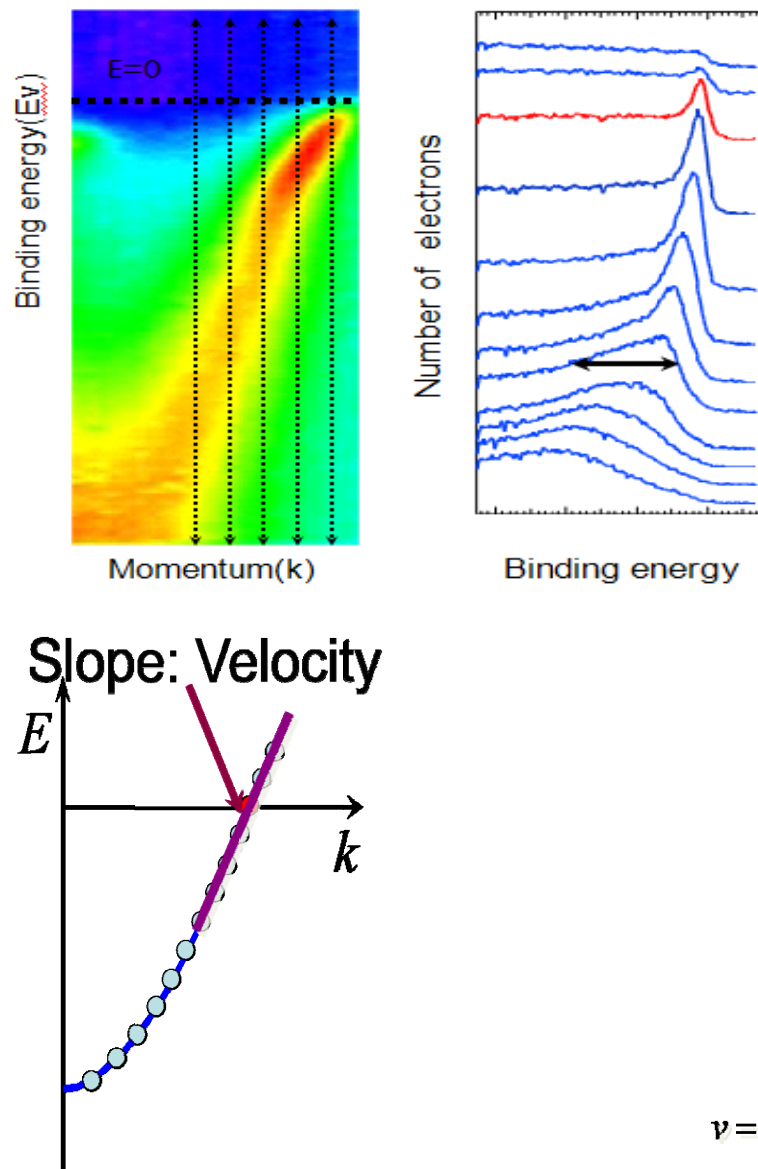


Figure 9. Energy Momentum Relation from ARPES data

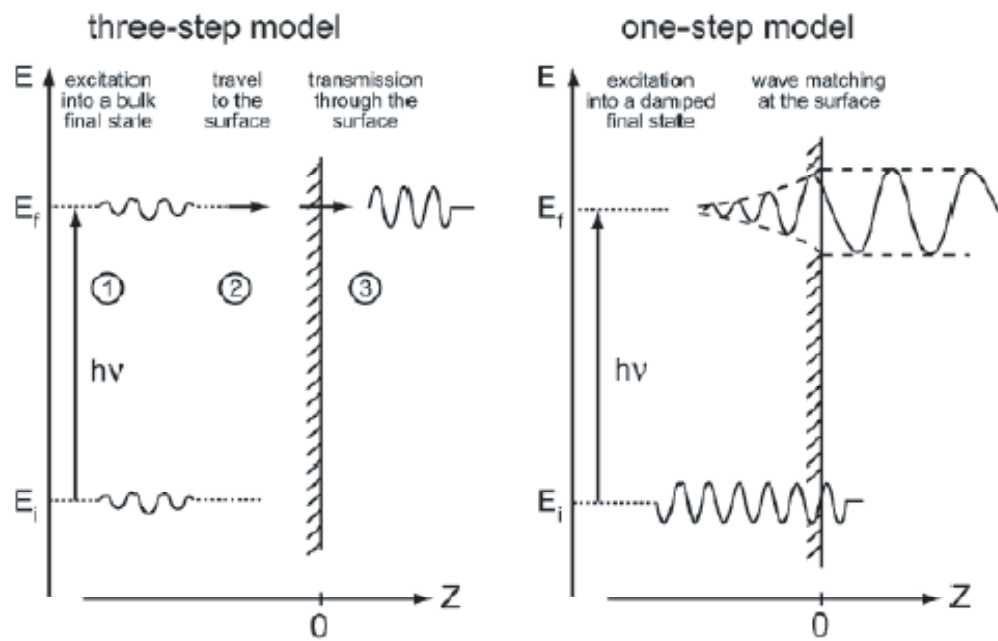


Figure 10. Graphic of One step and Three step process

This approximation is called as three step model [35]. We show the comparison between the one-step and three-step model in Fig.10. We would like to understand the process in which there is a transition of the bulk initial state to the bulk final state as the electron gets excited by the impinging electromagnetic radiation. Note that in this formalism we don't have to deal with the photoemitted electron separately, we will always work with the  $N$  particle wave function for the system. Let us assume that the initial state bulk wave function is  $\Psi_i^N$ , final state bulk wave function is  $\Psi_f^N$  and the interaction between the electron and photon is  $H_{int}$ . From Fermi's golden rule we can write the transition amplitude  $W_{fi}$  as:

$$W_{fi} = \frac{2\pi}{\hbar} |\langle \Psi_f^N | H_{int} | \Psi_i^N \rangle|^2 \delta(E_f^N - E_i^N - h\nu) \quad (3.9)$$

where,  $E_i^N = E_i^{N-1} - E_B^{\mathbf{k}}$  and  $E_f^N = E_f^{N-1} + E_{kin}$  are the initial and final state energies of the  $N$  particle system and the binding energy for the electron is  $E_B^{\mathbf{k}}$ . Treating the interaction with the photon as a perturbation, we could write the interaction term as follows:

$$H_{int} = \frac{e}{2mc} (\mathbf{A} \cdot \mathbf{p} + \mathbf{p} \cdot \mathbf{A}) = \frac{e}{mc} \mathbf{A} \cdot \mathbf{p} \quad (3.10)$$

where,  $\mathbf{A}$  is the electromagnetic vector potential and  $\mathbf{p}$  is the momentum operator of the excited electron.

Now we can write the initial state  $N$  particle wave function as a combination of a one electron wave function and a  $(N - 1)$  particle wave function. For example, one could write  $\Psi_f^N$  as follows:

$$\Psi_f^N = A\phi_f^{\mathbf{k}}\Psi_f^{N-1} \quad (3.11)$$

where,  $\phi_f^{\mathbf{k}}$  is the single particle wave function of the final state having momentum  $\mathbf{k}$  and  $\Psi_f^{N-1}$  is the final state wave function for  $(N - 1)$  particles. The wave function of a system of fermions needs to be antisymmetric and the antisymmetrization operator  $A$  takes care of that. By the same token, one could write  $\Psi_i^N$  as follows:

$$\Psi_i^N = A\phi_i^{\mathbf{k}}\Psi_i^{N-1} \quad (3.12)$$

where,  $\phi_i^{\mathbf{k}}$  is single particle wave function of the initial state having momentum  $\mathbf{k}$  and  $\Psi_i^{N-1}$  is the initial state wave function for  $(N - 1)$  particles. The total photomeimission cross section can be written as:

$$I(\mathbf{k}, E_{kin}) = \sum_{i,f} W_{f,i}. \quad (3.13)$$

One can consider that after the removal of an electron the system will be in an energy eigenstate  $\Psi_m^{N-1}$  with total energy  $E_m^{N-1}$ . Hence, the total cross section will be sum of all the transition amplitudes corresponding to all possible values of  $m$ . If we replace  $\Psi_f^{N-1}$  by some



energy eigenstate  $\Psi_m^{N-1}$  with energy  $E_m^{N-1}$ , then we could write the total photoemission cross section as follows:

$$I(\mathbf{k}, E_{kin}) = \sum_{f,i} |M_{f,i}^{\mathbf{k}}|^2 \sum_m |\alpha_{m,i}|^2 \delta(E_{kin} + E_m^{N-1} - E_i^{N-1} - E_B - h\nu) \quad (3.14)$$

where the overlap integral  $\alpha_{m,i} = |\langle \Psi_m^{N-1} | \Psi_i^{N-1} \rangle|^2$  is the probability that the removal of an electron from state  $i$  will leave the system having  $(N-1)$  electrons to the excited state  $m$  with energy  $E_m^{N-1}$  and  $M_{f,i}^{\mathbf{k}} = |\langle \phi_f^{\mathbf{k}} | \phi_i^{\mathbf{k}} \rangle|^2$  is the one—electron dipole matrix element.

In the discussions of photoemission on many body system, the Green's function formalism  $G(\mathbf{k}, t)$  formalism [36] is the most powerful and commonly used approach. The Green's function  $G(\mathbf{k}, t)$  can be treated as the probability amplitude that an electron having momentum  $\mathbf{k}$  added to the system will still be in the same state after time  $t$ . The Fourier transform of  $G(\mathbf{k}, t)$  is  $G(\mathbf{k}, \omega)$ . One can write  $G(\mathbf{k}, \omega) = G^+(\mathbf{k}, \omega) + G^-(\mathbf{k}, \omega)$ . Now let us consider the operators  $c_{\mathbf{k}}^+$  (creation operators) and  $c_{\mathbf{k}}$  (annihilation operators) such that  $\Psi_i^{N-1} = c_{\mathbf{k}} \Psi_i^N$ . In the zero temperature limit one can write:

$$G^{\pm}(\mathbf{k}, \omega) = \frac{\sum_m |\langle \Psi_m^{N\pm 1} | c_{\mathbf{k}}^{\pm} | \Psi_i^N \rangle|^2}{\omega - E_m^{N\pm 1} + E_i^N \pm i\eta}. \quad (3.15)$$

One defines the single particle spectral function  $A(\mathbf{k}, \omega) = -(1/\pi) \text{Im} G(\mathbf{k}, \omega) = -(1/\pi) (G^+(\mathbf{k}, \omega) + G^-(\mathbf{k}, \omega)) = A^+(\mathbf{k}, \omega) + A^-(\mathbf{k}, \omega)$ . Then one can show that

$$A^{\pm}(\mathbf{k}, \omega) = \sum_m |\langle \Psi_m^{N\pm 1} | c_{\mathbf{k}}^{\pm} | \Psi_i^N \rangle|^2 \delta(\omega - E_m^{N\pm 1} - E_i^N). \quad (3.16)$$

Now if we compare Eq 2.16 and Eq 2.14, it is easy to see that ARPES intensity can be related to  $A^-(\mathbf{k}, \omega)$  if we identify  $\omega$  as the energy of the electron in the system with respect to the Fermi energy  $E_F$ . Hence one could finally write

$$I(\mathbf{k}, \omega) = M(\mathbf{k}, \omega, h\nu) f(\omega) A(\mathbf{k}, \omega) \quad (3.17)$$

where

- (i)  $M(\mathbf{k}, \omega, h\nu) = |M_{f,i}^{\mathbf{k}}|^2$ , dipole matrix element which is general a function of  $\mathbf{k}$ ,  $\omega$  and photon energy  $h\nu$
- (ii)  $\mathbf{k}$  is electronic momentum parallel to the sample surface
- (iii)  $\omega$  is the energy of the electron with respect to the Fermi level  $E_F$
- (iv)  $f(\omega)$  is Fermi function which makes sure that the photoemission intensity is related to only  $A^-(\mathbf{k}, \omega)$

### 3.4 Different representations of ARPES data

As we saw in the previous section ARPES data is a function of both  $\mathbf{k}$  and  $\omega$ , therefore one can represent ARPES data as:

- (i) a function of  $\omega$  for a fixed  $\mathbf{k}$ , known as Energy Distribution Curve (EDC),
- (ii) a function of  $\mathbf{k}$  for a fixed  $\omega$ , known as Momentum Distribution Curve (MDC).

For a non-interacting system EDC and MDC should be equivalent. But for an interacting system like a High Temperature Superconductor, EDC and MDC are not equivalent as shown

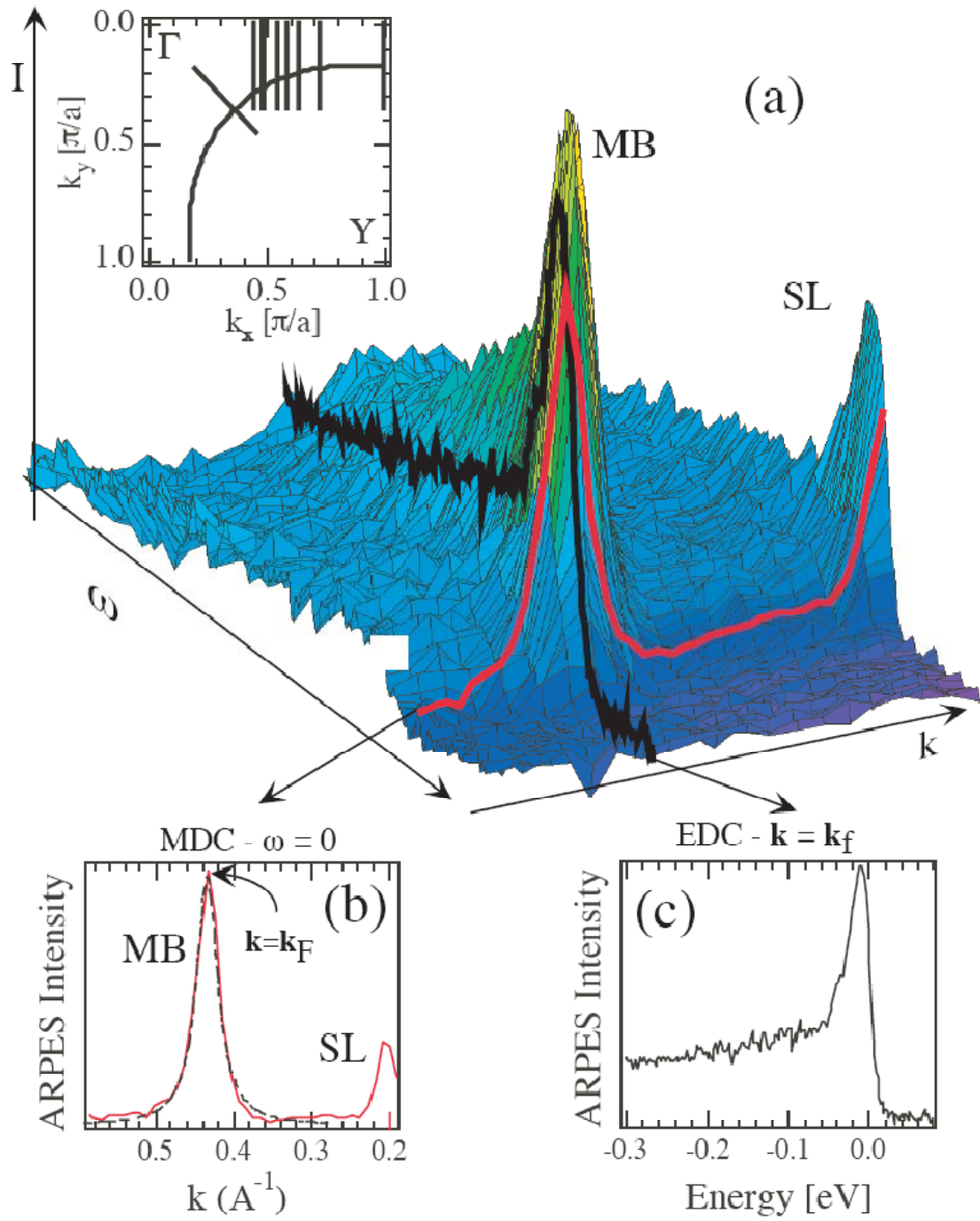


Figure 11. EDC and MDC interpretation of ARPES data

in Fig.11. EDC and MDC have different functions in data analysis. For example, when we want to measure the energy gap size, to find the sample temperature, the electron life time we usually use EDC. When we want to determine the Fermi momentum, to find the self-energy, we always use MDC.

## CHAPTER 4

### ELECTRONIC PHASE DIAGRAM OF HIGH-TEMPERATURE COPPER OXIDE SUPERCONDUCTORS

We have already seen that in conventional superconductors there is only a single temperature scale  $T_c$  separating the normal state from the superconducting state, the high temperature superconductors exhibit two additional temperature scale. One is the pseudogap scale  $T^*$ [37],[38] below which electronic excitation exhibit an energy gap. The second is the coherence scale  $T_{coh}$ [39], below which sharp spectral features appear due to increased lifetime of the excitations. Keep in mind all these experimental result, in this chapter we will address following questions:

- (i) There are two major schematics about the phase diagram for cuprates. As shown in Fig.12, a. is the phase diagram in which  $T^*$  and  $T_{coh}$  intercept at single quantum critical point near optimal doping. b. is the phase diagram of doped mott insulator. What is the relation between  $T^*$  and  $T_{coh}$  line. Do they have crossing point or there is a single quantum critical point where  $T^*$  and  $T_{coh}$  meets .
- (ii) What is the doping dependent of  $T^*$  and  $T_{coh}$ .

For the discussion we will show the result of ARPES measurements on fourteen  $\text{Bi}_2\text{Sr}_2\text{CaCu}_2\text{O}_{8+\delta}$  (Bi2212) samples, range from UD 67K to OD 55K. The crystal samples were grown in traveling solvent floating zone furnaces, and the thin film samples were grown using an RF sputtering process. The  $T_c$  of the samples were defined either by where the diamagnetism reaches satu-

ration, or where the resistance becomes zero, within the uncertainty of the measurement. For all the samples, both films and single crystals  $T_c^{max} \sim 91K$ . All samples were characterized by x-ray diffraction. The samples were doped by changing their oxygen content through an annealing process. Superconducting transition widths of  $< 5K$  were obtained. The doping value was determined from the Presland et al.

#### 4.1 ARPES measurement and data analysis

ARPES measurements were carried out at the Synchrotron Radiation Center, Wisconsin, and the Swiss Light Source, using Scienta R2002 and R4000 analyzers. 22eV photons with polarization parallel to  $(0,0)(\pi,0)$  were used, in order to maximize the signal at the antinode. The energy resolution was 15 - 20 meV (FWHM) with a k-resolution of 0.0055<sup>-1</sup>. For a given cut, we divide the photoemission data by a resolution broadened Fermi function and determine  $k_F$  from the spectrum which (a) has a peak at chemical potential when the system is gapless, or (b) the peak is closest to the chemical potential when the system is gapped, both in the superconducting and pseudogap states. If the symmetrized EDC (i.e. ARPES intensity  $I(k,\omega)$  as a function of  $\omega$  for a fixed  $k$ ) at some  $k_F$  is peaked at  $\omega = 0$ , the corresponding point on the fermi surface has no gap, otherwise it is gapped. The energy gap at a point on the fermi surface is the peak-to-peak separation of the symmetrized EDC at the corresponding  $k = (k_x, k_y)$ .

#### 4.2 $T^*$ and $T_{coh}$

General features of the phase diagram of the copper oxide superconductors have been known for some time. The superconducting transition temperature  $T_c$  has a dome-like shape in the doping-temperature plane with a maximum near a doping  $\delta \sim 0.164$ . While in conventional

metals the electronic excitations for  $T > T_c$ , are (i) gapless and (ii) sharply defined at the Fermi surface, the cuprates violate at least one of these conditions over much of their phase diagram. These deviations from conventional metallic behaviour are most easily described in terms of two crossover scales  $T^*$  and  $T_{coh}$ , which correspond to criteria (i) and (ii), respectively.

To address the role of these energy scales in defining the phase diagram, we concentrate on spectra at the antinode  $((\pi, 0) - (\pi, \pi)$  Fermi crossing), where the spectral changes with doping and temperature are the most dramatic. In Fig. 13, we show spectra at fixed temperature as a function of doping. Data points are indicated in Fig. 13a. Initially, we show spectra at fixed momenta as a function of energy (energy distribution curves, or EDCs) that have been symmetrized about the Fermi energy to remove the effects of the Fermi function[60]. Later, we show that equivalent results are obtained from division of the EDCs by a resolution-broadened Fermi function. In Fig. 13b the spectra at the highest temperature ( $\sim 300K$ ) show two remarkable features: they are extremely broad in energy, exceeding any expected thermal broadening, and their lineshapes, well described by a lorentzian, are independent of doping. The large spectral widths indicate electronic excitations that cannot be characterized by a well defined energy, implying that the electrons are strongly interacting. The incoherent behavior of the spectra at 300 K is consistent with the strange metal regime in two model phase diagrams popular in the literature, shown schematically in Fig. 12 a. If Fig. 12a applies, there would be strong evidence for a single quantum critical point near optimal doping which dominates the behavior to high temperatures[44],[43]. In addition to identifying the sharp peak via a decomposition of the spectrum into a broad lorentzian and a sharp gaussian, the presence

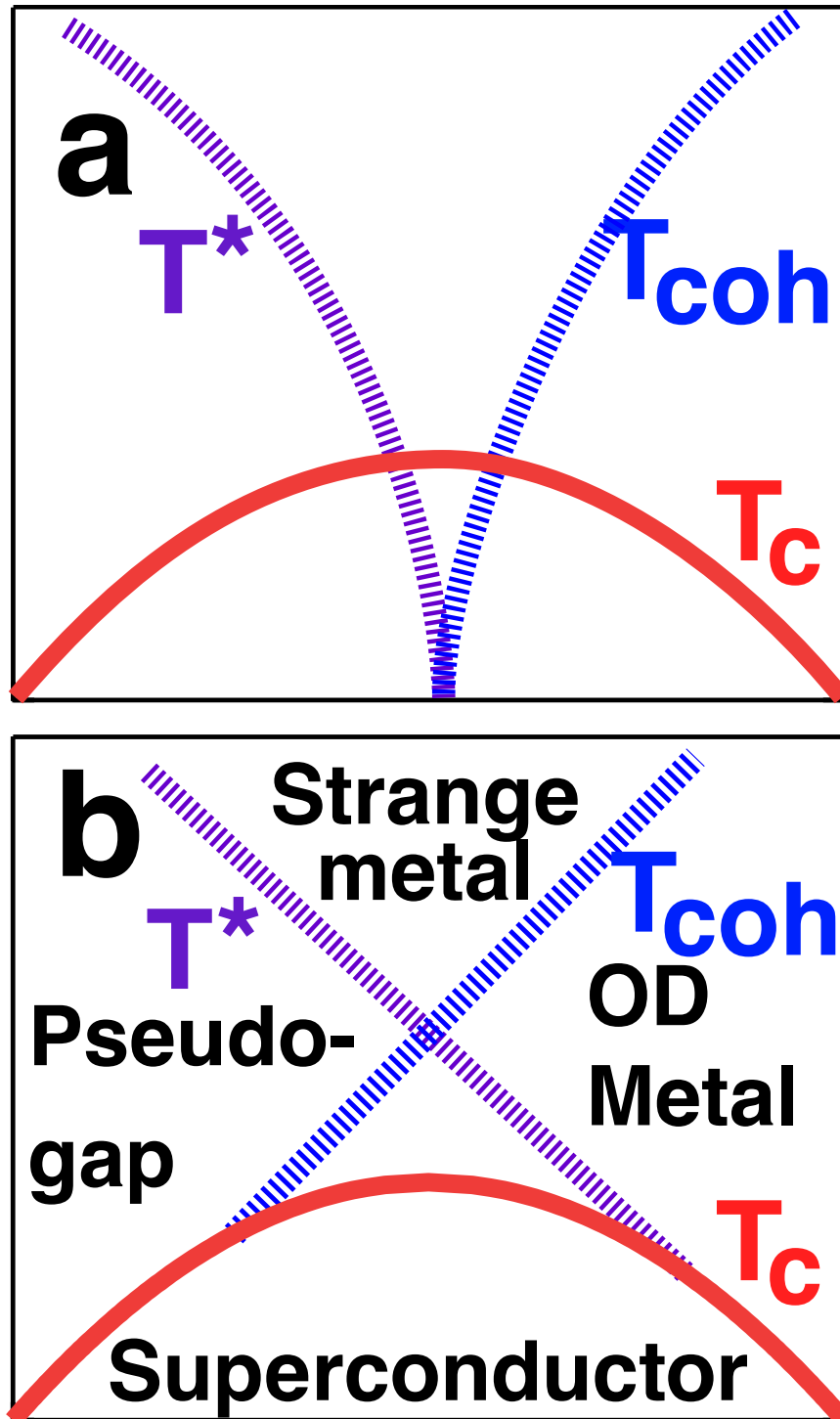


Figure 12. Phase diagram schematics:(A) Schematic phase diagram for a quantum critical point near optimal doping. (B) Schematic phase diagram for a doped Mott insulator.



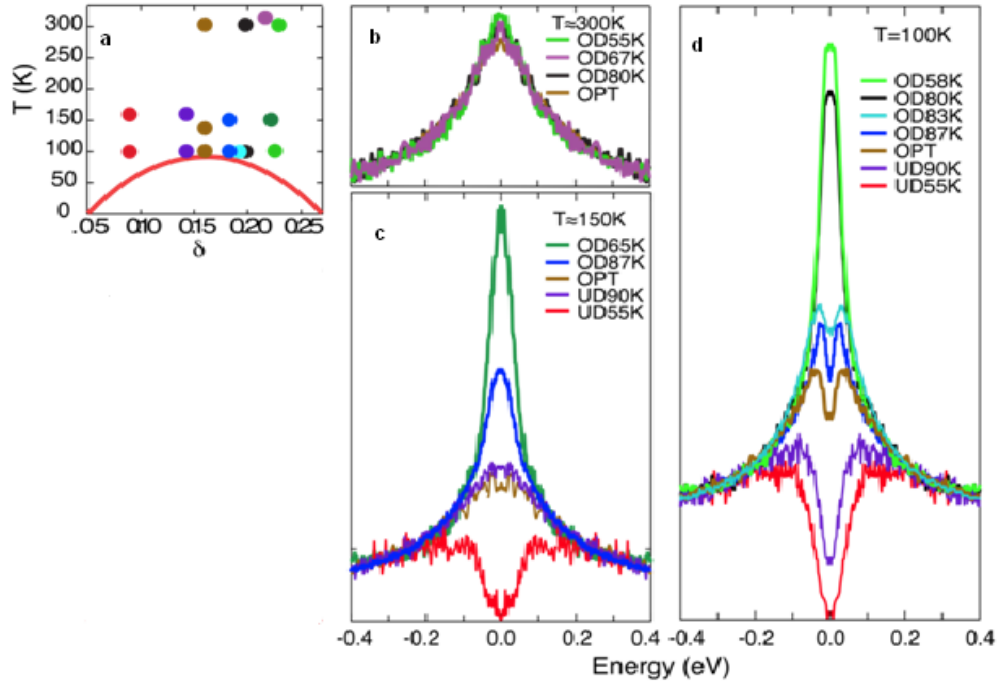


Figure 13. Spectra at constant temperature as a function of doping. (A) Dots indicate the temperature and doping values of the spectra of the same color plotted in BD. (B) Spectra at  $T \sim 300$  K for several samples measured at the antinode, where the d-wave superconducting gap below  $T_c$  is largest. The spectra are normalized to high binding energy and symmetrized in energy to eliminate the Fermi function. The doping values are indicated by the top row of dots in A. (C) Same as in B, but at  $T \sim 150$  K, with the dopings indicated by the middle row of dots in A. (D) Same as in B, but at  $T = 100$  K, with the dopings indicated by the bottom row of dots in A.

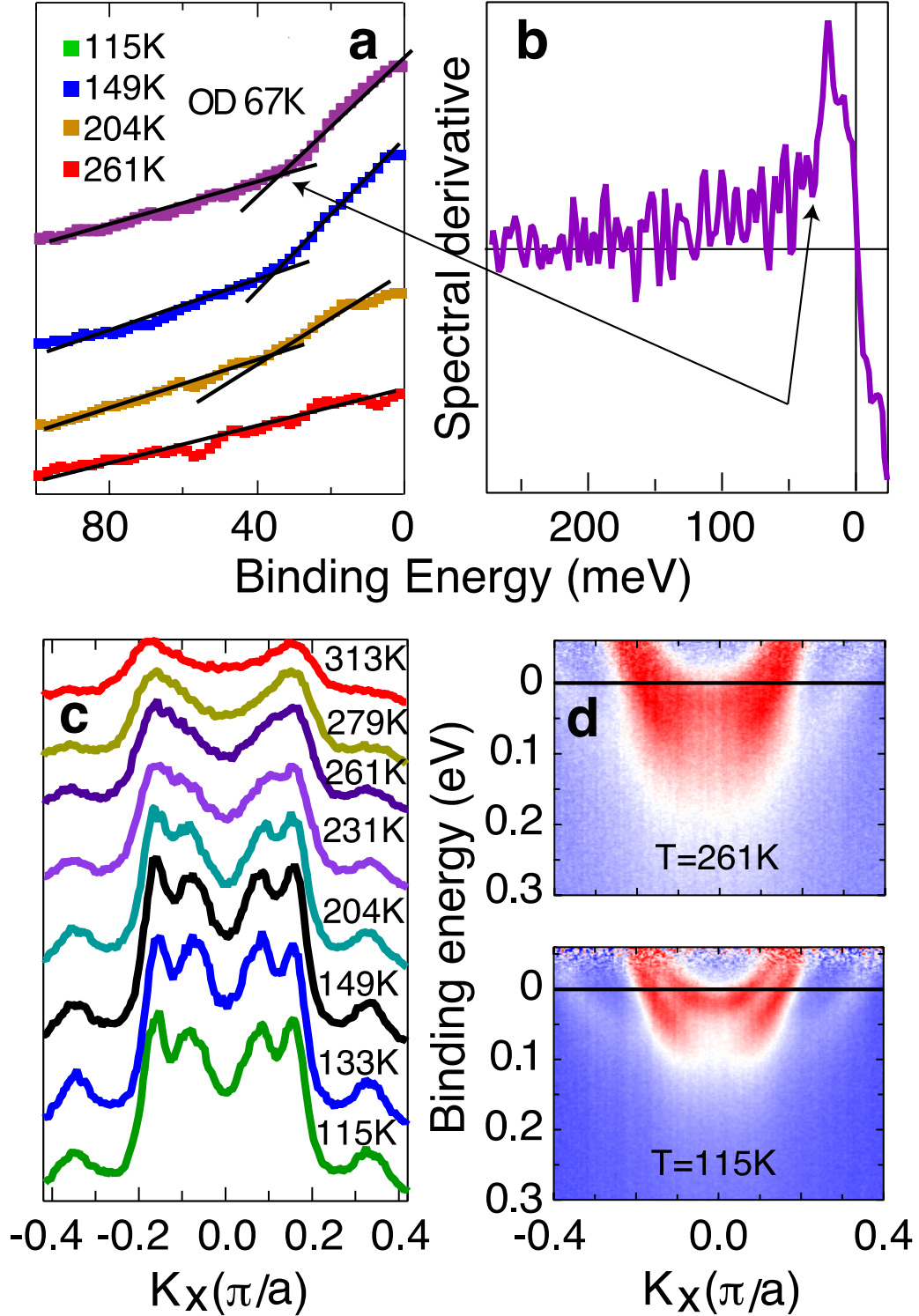
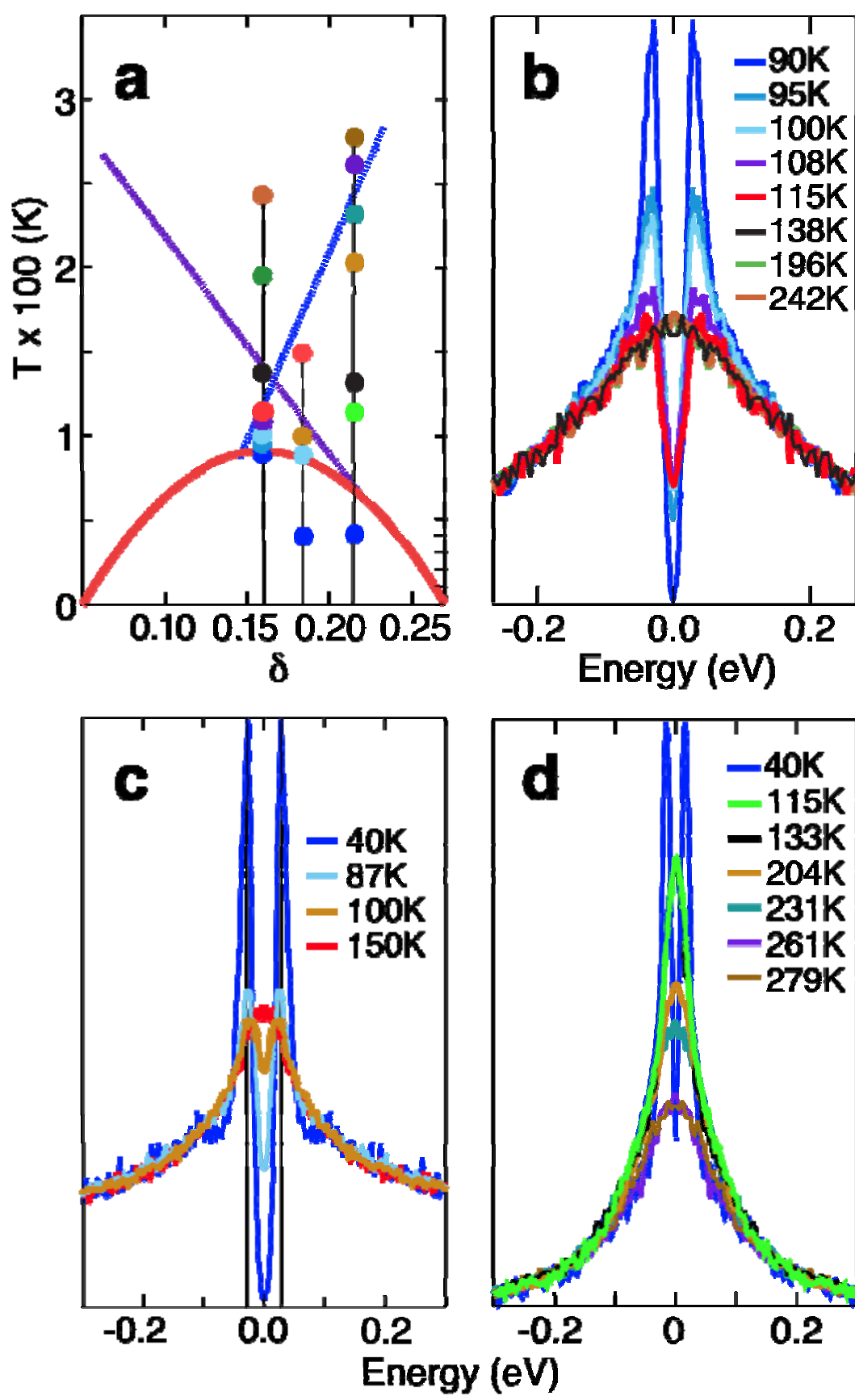


Figure 14. Additional signatures of spectral coherence. a Spectra for a small range of binding energy for different temperatures, showing the break visible when the coherent component merges with the incoherent component. The straight lines are guides to the eye. These spectra are for an overdoped 67K sample. b Derivative of the top spectrum shown in a. The sharp change in the slope at the break point is indicated by the arrows. c Spectra at constant

of a sharp peak can also be deduced directly from the raw spectra. A sharp break in the slope of the raw spectra is present at the binding energy where the coherent region of the spectra merges into the incoherent part, as shown in Fig. 14a. For  $T > T_{coh}$ , no break is discernible. For spectra with sufficiently high signal-to-noise ratio, the break can also be identified from the sudden increase in the derivative of the spectra, as shown in Fig. 14b. A consequence of coherence in bi-layer cuprates such as  $\text{Bi}_2\text{Sr}_2\text{CaCu}_2\text{O}_{8+\delta}$  is a coupling of the states from each layer into a bonding and an antibonding combination, as discussed in earlier work. Here we show a detailed temperature evolution of the spectra as a function of momentum, but at fixed energy in Fig. 14c, at chemical potential, but integrated over an energy range of meV. Below  $T_{coh}$ , two peaks can be seen on either side of the  $\text{CuO}_2$  bond direction, the inner-most corresponding to the antibonding and the outermost to the bonding combinations. As the temperature increases, the antibonding component merges into the bonding one, after which one broad peak is observed above  $T_{coh}$ . Similar results can be found from the intensity maps in Fig. 14d. We note that in previous work we did not observe the merging of the bonding and antibonding combinations, due to the reduced momentum resolution of earlier experiments.  $T^*$  would be the transition temperature for a competing order, with  $T_{coh}$  its ‘mirror’ corresponding to where Fermi liquid behaviour sets in. The non-Fermi liquid behaviour in the strange metal phase above both scales would then arise from fluctuations in the quantum critical region[45]. These same fluctuations presumably mediate superconducting pairing. On the other hand if Fig. 12a applies, the phase diagram would arise from strong correlation theories based on doped Mott insulators[81],[47],[70],[48]. The  $T^*$  line is where spin excitations become gapped, whereas  $T_{coh}$

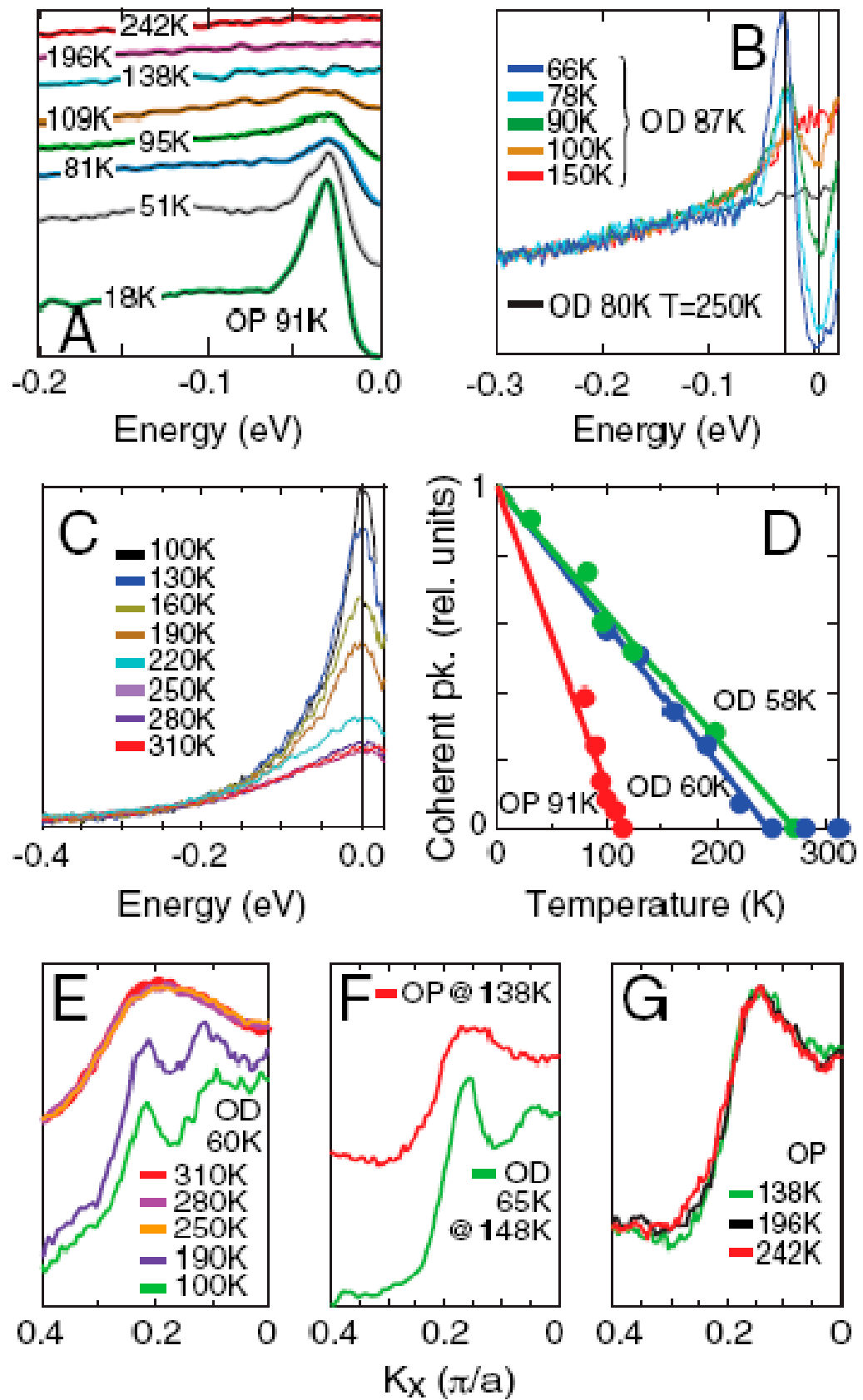
is the temperature below which doped carriers become coherent. Superconductivity emerges below both scales, where spin and charge excitations become gapped and coherent. Which of these two phase diagrams is the appropriate one has critical implications for our understanding of the cuprates. To study this, we reduce  $T$ . In Fig. 13c we show that at  $\sim 150K$ , the spectra has marked changes with doping, and three regions can be identified. At low  $\delta$ , the spectrum (red curve) remains broad as in Fig. 13b, but now a spectral gap is present - the pseudogap. This results in a reduction of the low-energy spectral weight as probed by various experiments[50]. On increasing  $\delta$ , the spectral gap becomes less pronounced, and disappears just below optimal doping (purple and brown curves), where the spectra now resemble those in Fig. 13b. Increasing  $\delta$  beyond 0.17, the spectra exhibit a sharp peak centred at zero energy ( $E_f$ ) (blue and green curves). These spectra are now similar to what one would expect for a more conventional metal. The doping dependences near 150K are again consistent with either Fig. 12a or 12b. A completely different behaviour emerges at a lower temperature, 100K (Fig. 13d). The pseudogap is still present for low  $\delta$  (red and purple curves). But near optimal doping, the spectra change, now exhibiting sharp peaks separated by an energy gap (brown, blue and light blue curves). These sharp peaks indicate that the lifetimes of excitations have increased dramatically, in contrast to the spectra at 150K for optimal doping (brown curve in Fig. 13c). For still higher  $\delta$ , a single sharp peak centred at  $E_F$  appears (green and black curves). Notice that all the spectral changes are limited to an energy scale of less than 200 meV; outside this energy range, the spectra follow the same broad lorentzian shape as in Fig. 13b. Fig. 13d demonstrates that the spectral gap and coherence (manifested by sharp spectral peaks) coexist

in the normal state near optimal doping, implying that the  $T^*$  and  $T_{coh}$  lines cross each other, as in Fig. 12c. To further determine where the crossing appears, we plot spectra at fixed doping as a function of temperature, with the various data points indicated in Fig. 15a. Fig. 15b shows spectra for an optimally doped sample. At  $T = 90K$  (blue curve) the sample is just emerging from the superconducting state. Increasing  $T$ , the sharp peaks at the edge of the gap decrease in intensity, while the gap magnitude remains constant. Finally, for  $T > 108K$ , the sharp peaks disappear, while the spectral gap remains (red and black curves). This indicates that the  $T_{coh}$  line has been crossed, but not the  $T^*$  line. For  $T > 138K$ , the spectral gap has completely filled in (green and orange curves), and the spectra have regained the broad lineshape characteristic of the strange metal phase of Fig. 13b. In contrast, upon increasing the doping, the crossing of the pseudogap and coherence temperatures are reversed, as illustrated in Fig. 14c. Starting in the superconducting state at 40K (blue curve), one can see the same features as in Fig. 15b, but now the spectral gap is smaller. Once  $T_c$  is crossed at 87K, the spectral gap and sharp peaks persist (bronze curve). But at higher  $T$ , the gap disappears, and we are left with a relatively sharp peak at  $E_F$  (red curve), in contrast to Fig. 15b. For higher temperatures (not shown), peaks broaden as in Fig. 13b. If the doping is now increased even further (Fig. 14d), a spectral gap is no longer observed at any  $T > T_c$ . In this highly overdoped region, the superconducting transition is similar to that of conventional superconductors, as the spectral gap closes very near  $T_c$ . The peak at  $E_F$  initially remains sharp, but at high enough temperatures, the strange metal returns (purple and brown curves).



### 4.3 Quantative determination of $T^*$ and $T_{coh}$ line

In Fig. 16, we show that dividing the EDCs by a resolutionbroadened Fermi function[52] gives equivalent results to symmetrizing them. To quantitatively determine the  $T^*$  line, we note that it is easily identified by where the spectral gap disappears[62]. For  $T_{coh}$  we need to identify where the sharp peak disappears. We find that we can model the broad, incoherent part of the spectrum with a lorentzian, and the sharp, coherent piece with a gaussian (a similar decomposition has been used in the very different context of the analysis of critical scattering). In Fig. 16d, we plot the height of the sharp component of the spectra above that of the constant Lorentzian. One clearly sees a linear decrease with T, from which we determine Tcoh. Tcoh can also be observed in plots of the angle-resolved photoemission (ARPES) signal as a function of momentum for a fixed energy, the momentum distribution curves shown in Fig. 16 EG. In Fig. 16E, we show that a significant change in width occurs upon crossing Tcoh, which clearly indicates that this is not a simple temperature broadening effect. The spectra remain relatively unchanged both below and above Tcoh, with significant changes limited to temperatures close to Tcoh. Furthermore, Tcoh is strongly doping dependent. In Fig. 16F, we show spectra at similar T for an optimally doped sample and an overdoped one with  $T_c = 65K$ , showing that the spectral widths depend on the region of the phase diagram, and not simply the temperature. This is emphasized in Fig. 16G, where no spectral changes are observed in the strange metalregion over a wide range in temperature.





#### 4.4 Conclusion

The phase diagram shown in Fig. 17 summarizes our results. The solid dots are based on the antinodal spectra and are colour coded to correspond to the four different regions in the normal state phase diagram. These correspond to antinodal spectra that are: (1) incoherent and gapped, in the underdoped pseudogap region, (2) incoherent and gapless, in the high temperature strange metal, (3) coherent and gapless, in the overdoped metal, and finally (4) coherent and gapped, in the triangular region above optimal doping formed as a result of the crossing of  $T^*$  and  $T_{coh}$ . In addition, we also plot  $T^*$  and  $T_{coh}$  as defined above by double triangles. We emphasize that below  $T_c$ , we find coherent and gapped antinodal spectra for all doping values, even for very underdoped samples.

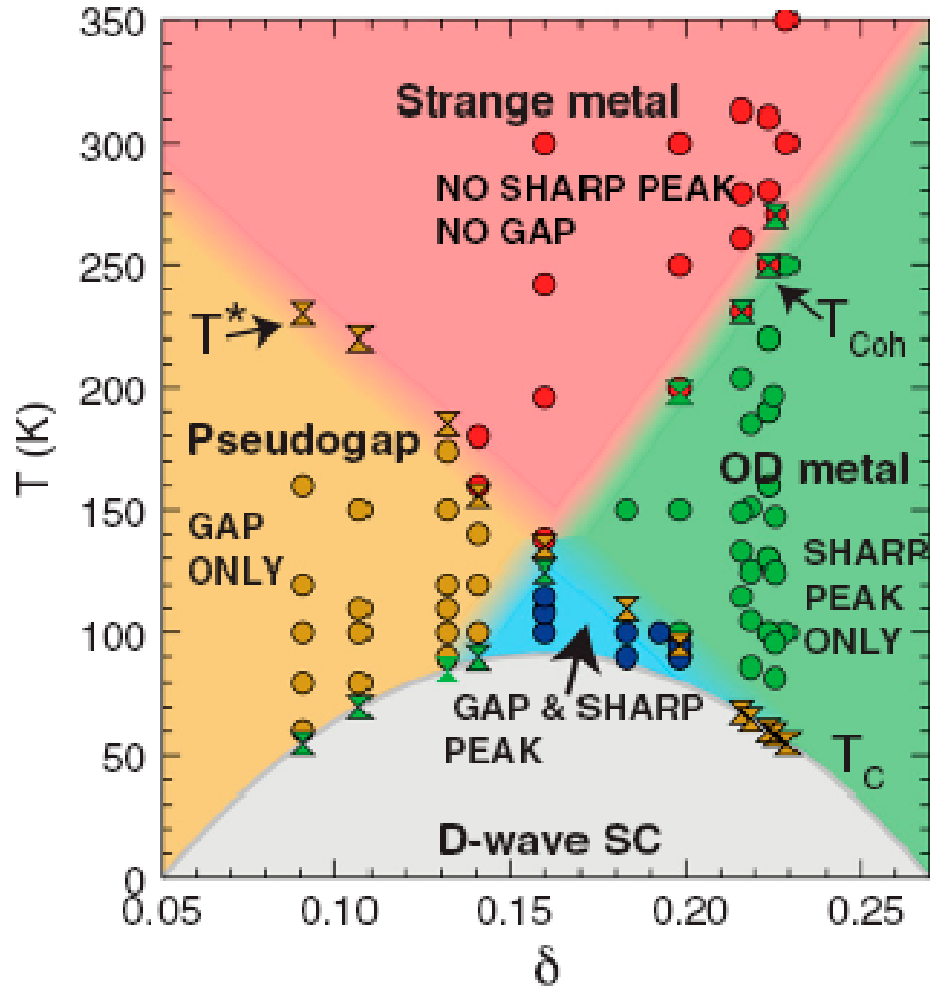


Figure 17. Electronic phase diagram of  $\text{Bi}_2\text{Sr}_2\text{CaCu}_2\text{O}_{8+\delta}$  versus hole doping,  $\delta$ . Brown dots indicate incoherent gapped spectra, blue points coherent gapped spectra, green dots coherent gapless spectra, and red dots incoherent gapless spectra. The brown double triangles denote  $T^*$ , and the green double triangles  $T_{\text{coh}}$ .  $T_c$  denotes the transition temperature into the superconducting state (shaded gray and labeled *D - wave SC*).

## CHAPTER 5

### OBSERVATION OF A D-WAVE NODAL LIQUID IN HIGHLY UNDERDOPED $\text{Bi}_2\text{Sr}_2\text{CaCu}_2\text{O}_{8+\delta}$ (BI2212)

High temperature superconductivity in the cuprates occurs by doping a Mott Insulator whose antiferromagnetic ground state and low-energy excitations are well understood[54]. By adding carriers, the parent insulator turns into a superconductor for dopings that exceed 0.05 holes per  $\text{CuO}_2$  plane. The d-wave nature of the superconducting ground state[55] and its low-lying excitations are also well understood. In between these two phases lies an electronic ground state whose nature is poorly understood. As the temperature is raised, this intermediate pseudogap state occupies a larger and larger region of the phase diagram (Fig. 19a). It is from this phase that the superconducting state emerges for all but the most highly doped samples. Consequently, the nature of this phase holds the key to the origin of high temperature superconductivity. While the electronic excitations in the high temperature pseudogap region have been studied extensively, there is little spectroscopic data at low temperatures, as there is only a very narrow window of dopings where neither superconducting nor antiferromagnetic order occurs. In this chapter we present angle-resolved photoemission spectroscopy (ARPES) data on single crystals and thin films[56] whose doping levels range all the way from the insulator to the over-doped superconductor.

## 5.1 Samples

We focus in particular on non-superconducting thin films, just to the left of the superconducting Tc dome (see Fig. 19a), with an estimated hole doping  $\sim 0.04$ [56]. These samples have an insulating upturn in resistance  $R(T)$  with decreasing temperature shown in Fig. 18b, that is well described by 2D-variable range hopping[57],[58]. We have measured the diamagnetic susceptibility down to 1.5 K, and found no trace of superconductivity, with a sensitivity of 1

## 5.2 How to measure the energy gap using ARPES

We will consider Fermi energy of the system  $E_F$  as the reference level for energy. It has been already approved that  $I(\mathbf{k}, \omega) = M(\mathbf{k}, \omega, h\nu)f(\omega)A(\mathbf{k}, \omega)$ , where:

- (i)  $I(\mathbf{k}, \omega)$  is the ARPES intensity corresponding to photoemission of an electron with momentum  $\mathbf{k}$  and energy  $\omega$  (relative to  $E_F$ ), using photons of energy  $h\nu$ .
- (ii)  $M(\mathbf{k}, \omega, h\nu)$  is the corresponding matrix element discussed in Chapter 2.
- (iii)  $f(\omega)$  is the fermi function.
- (iv)  $A(\mathbf{k}, \omega)$  is known as the spectral function.

The ARPES intensity as a function of energy at a fixed value of momentum  $\mathbf{k}_1$ , an EDC at  $\mathbf{k}_1$  and (b)  $I(\mathbf{k}, \omega = \omega_1)$  i.e. the ARPES intensity as a function of momentum for a fixed value of energy  $\omega_1$ , an MDC at  $\omega_1$ . The energy gap is defined in terms of the spectral function. The energy gap at any point on the fermi surface is given by the peak energy of  $A(\mathbf{k} = \mathbf{k}_F, \omega)$  where  $\mathbf{k}_F$  is the momentum coordinate for the corresponding point on the fermi surface. If  $A(\mathbf{k} = \mathbf{k}_F, \omega)$  is peaked at  $\omega = 0$  then we say that energy gap is zero at that point, otherwise

not. If the energy gap is non-zero we find out the peak position  $\Delta$  of  $A(\mathbf{k} = \mathbf{k}_F, \omega)$  and  $\Delta$  gives the energy gap at that point. In actual ARPES experiment we can not find the whole fermi surface in one single measurement, rather we need to take a series of measurements to obtain the whole fermi surface. We stack the data from different measurements one after the another in order to construct the whole fermi surface. Essentially each measurement, commonly referred as a cut, gives the data in a momentum window (depends on the finite acceptance angle of the detector) around some specific point on the fermi surface, i.e. around some specific  $\mathbf{k}_F$ . We need to identify the  $\mathbf{k}_F$  corresponding to each cut for gap measurement. We know that  $I(\mathbf{k}, \omega)$  is not exactly  $A(\mathbf{k}, \omega)$  because of the factors  $f(\omega)$  and  $M(\mathbf{k}, \omega, h\nu)$ . Actually, if one is not interested in the quantitative details of  $A(\mathbf{k}, \omega)$ , one can think  $M(\mathbf{k}, \omega, h\nu)$  as some overall factor because  $M(\mathbf{k}, \omega, h\nu)$  does not vary much with energy. For the determination of the gap, we are not interested in quantitative details of the spectral function, rather we would like to know only its peak position. So we will simply ignore the matrix elements.

Hence, to find out the energy gap we need to (a) first determine the fermi momentum  $\mathbf{k}_F$ , (b) then get rid of the effect of fermi function from the EDC at  $\mathbf{k}_F$  and (c) finally look for the peak position of the fermi function free EDC at  $\mathbf{k}_F$ . There are several ways to do this. For our analysis we have used one of them—namely symmterization. Without going into detail, below we will briefly discuss this procedure.

### 5.2.1 Symmterization

Let us start with a cut, i.e. a number of EDCs at different  $\mathbf{k}$  points around some  $\mathbf{k}_F$ . We know that an EDC at  $\mathbf{k}$  is  $f(\omega)A(\mathbf{k}, \omega)$ . For reasons explained before we do not take into account

of the matrix elements. The fermi function behaves like a step function at zero temperature. Hence, at zero temperature, ARPES can not access any state having positive energy. But at finite temperature the fermi function has some width and hence, ARPES can probe states with small positive energies consistent with the finite temperature width of the the fermi function. Let us assume that each EDC is defined in an energy window,  $-\omega_2 < \omega < +\omega_1$ . Using experimental data for each  $\mathbf{k}$  we define a new EDC in the energy window  $-\omega_1 < \omega < +\omega_2$  which is the the mirror image of the old EDC (which is directly obtained from experimental data) at every  $\mathbf{k}$ , with respect to  $\omega = 0$ . Afterwards, at each  $\mathbf{k}$ , we add the old EDC with the new EDC for the corresponding  $\mathbf{k}$  and we call the sum as the *symmetrized EDC* at that  $\mathbf{k}$ . Note that, due to the way the symmterized EDC is constructed, it would be defined in an energy window  $-\omega_1 < \omega < +\omega_1$ . Hence, in general, the symmterized EDC will have two peaks. If we find that for some  $\mathbf{k}$  peak-to-peak separation for the corresponding symmetrized EDC is zero, then we say that the system has no gap, otherwise the system is gapped. If the system is gapped, we look for the  $\mathbf{k}$  for which peak-to-peak separation is minimum, the corresponding  $\mathbf{k}$  is the  $\mathbf{k}_F$ . The gap value will be the peak-to-peak separation of the symmterized EDC at that  $\mathbf{k}_F$ . Below we show why this procedure works.

Since an old EDC at  $\mathbf{k}$  is  $f(\omega)A(\mathbf{k},\omega)$  and hence the corresponding new EDC at  $\mathbf{k}$  is  $f(-\omega)A(\mathbf{k},-\omega)$ . The corresponding symmetrized EDC is,  $f(\omega)A(\mathbf{k},\omega) + f(-\omega)A(\mathbf{k},-\omega)$ . If one considers the identity  $f(-\omega)=1 - f(\omega)$  and the assumption that  $A(\mathbf{k},-\omega) = A(\mathbf{k},\omega)$ , it is easy to see that the symmetrized EDC at the corresponding  $\mathbf{k}$  is simply  $A(\mathbf{k},\omega)$ . The specific assumption we made here, is known as *particle-hole approximation*. Hence, by looking at the

energy dependence of the symmetrized EDC, the gap can be found out. Strictly, speaking particle-hole approximation is only valid at  $\mathbf{k} = \mathbf{k}_F$ , but it turns out that one can quite safely use this approximation for any  $\mathbf{k}$  as long as  $|\mathbf{k} - \mathbf{k}_F|$  is not too large.

### 5.3 Gap anisotropy in the PG state and in the SC state

The SC order parameter in HTSC materials has d-wave symmetry. Hence SC the gap (which is basically the amplitude of the SC order parameter) in HTSC materials is highly anisotropic in momentum space, too. In particular, the SC gap has the form,  $\Delta_{\mathbf{k}} = \frac{\Delta_{\max}}{2} (\cos(k_x) - \cos(k_y))$  where the momentum  $\mathbf{k} = (k_x, k_y)$ . There are four points on the fermi surface where SC gaps are exactly zero—known as nodes. Points on the fermi surface where the SC gap reaches its maximum value, are called antinodes. The energy gap in the PG state is highly anisotropic too. But the gap anisotropy in the PG state is different from that in the SC state. Below we contrast the SC state with the PG state in terms of the gap anisotropy. In Figs. 18a and 18b we present data for a slightly underdoped sample of  $\text{Bi}_2\text{Sr}_2\text{CaCu}_2\text{O}_{8+\delta}$  (Bi2212) with a  $T_c = 90\text{K}$ , for (a) the superconducting state at 40K, and (b) the pseudogap phase at 140K. Shown are EDCs at the Fermi momentum  $\mathbf{k}_F$ , which have been symmetrized to remove the effects of the Fermi function on the spectra (as explained before). Fifteen momentum cuts were measured, as shown in Fig. 18d. These momentum cuts cover one-quarter of the whole Brillouin zone. We can easily see from Fig. 18a, that among all fifteen different cuts, only at one cut peak-to-peak separation for symmetrized EDC is zero. Hence, in the SC state only at one single point on the fermi surface, does the energy gap vanish, and this is consistent with the fact that the SC state has point nodes. On the contrary, in the PG state (Fig. 18b, Fig.

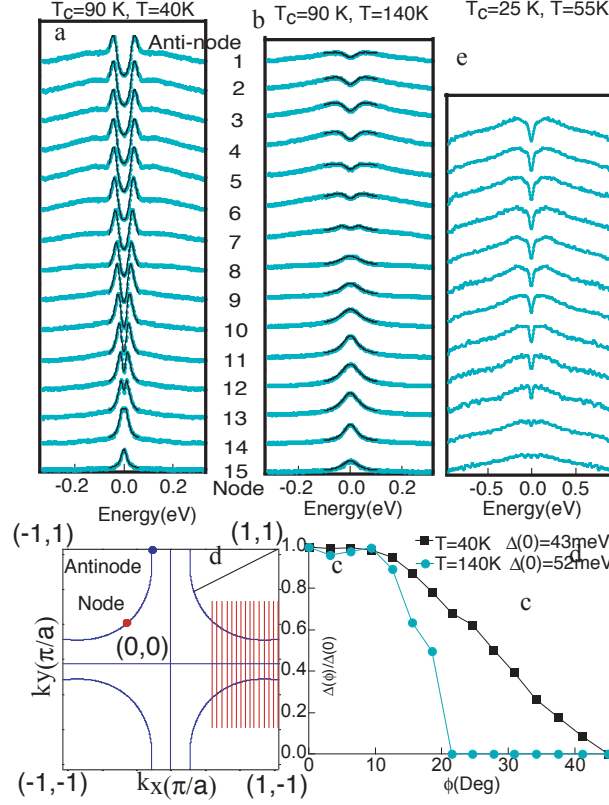


Figure 18. Symmetrized EDCs for underdoped samples along the Fermi surface. (a)  $T_c = 90\text{ K}$  sample in the superconducting state at  $T = 40\text{ K}$ , and (b) the same sample in the pseudogap phase at  $T = 140\text{ K}$ . The bottom EDC is at the node, while the top is at the anti-node, as defined in (d). (c) Variation of the gap around the Fermi surface extracted from (a) and (b). (d) Location of the momentum cuts (red lines), Fermi surface (blue curves), and special points (node and anti-node) in the zone. (e) Symmetrized EDCs for a very underdoped,  $T_c = 25\text{ K}$ , sample (corresponding to  $\mathbf{k}_F$  points 4 through 15), measured at  $55\text{ K}$  in the pseudogap state.



18d) there are more than one cuts at which the peak-to-peak separation for symmetrized EDC is zero. Hence in the PG state, unlike the SC state, the energy gap vanishes over a finite length along the fermi surface. This is manifestation of the disconnected fermi surface in the PG state, known as fermi arc. In order to compare the gap anisotropy in the PG state to the one in the SC state, we have plotted corresponding energy gaps as a function of fermi surface angle( $\phi$ ) in Fig. 18c. We can identify any point on the fermi surface either by specifying  $\mathbf{k} = (k_x, k_y)$  of the point or equivalently by specifying  $\phi$  as shown in Fig.18d. It is quite evident that the SC gap( shown as black dots in Fig. 18c) varies quite smoothly as a function of  $\phi$ , more specifically it goes approximately like  $\cos(2\phi)$ . It is still not clear whether the SC gap as a function of  $\phi$ , goes like  $\cos(2\phi)$  for all doping level. But for our discussions, we do not need to worry about the exact functional form of the SC gap. In contrast to the SC state, the gap in the PG state, opens quite abruptly as for a number of points (cuts 8 through 15 in Fig. 18b) on the Fermi surface energy gap vanishes.

#### 5.4 Result

In Fig. 19d we show the energy distribution curves (EDCs, spectra at constant momentum  $\mathbf{k}$  as a function of binding energy ). Despite the low temperature, no sharp, coherent features are discernable in the spectra. This is not surprising, since earlier work had found a strong suppression of coherent spectral weight in the superconducting state with underdoping[59]. In contrast, the momentum distribution curves (MDCs) in Fig. 19e at  $\pi=0$  show clearly visible peaks. Thus the excitations are much better defined in  $\mathbf{k}$ -space than they are in energy, and are sharper near the zone diagonal than near its boundary (the Brillouin zone is shown in Fig.

19c). Remarkably, despite the insulating-like nature of the resistivity, the MDC peaks indicate a locus of minimum energy excitations similar to that of the superconductors, clearly visible in the ARPES intensity map in Fig. 19c at  $\pi=0$ . These Fermi momentum ( $K_F$ ) values were in fact used to generate the EDCs in Fig. 19d. In Fig. 19f we show the ARPES intensity as a function of energy and  $k$  for another sample at the same doping, which shows that there is a well-defined dispersion despite the incoherent nature of the EDCs. To better understand the electronic excitations in the non-superconducting sample in Fig. 20d, we plot its raw EDCs at  $k_F$ , symmetrized to remove the effects of the Fermi function[60], and compare them with superconducting state spectra (Figs. 20e, f, and g) at various doping indicated in Fig. 20a. In each panel d through g, the top curve corresponds to  $k_F$  on the zone boundary ( $\theta=0$ ), while the lowest curve to  $K_f$  on the zone diagonal ( $\theta=45$ ), with the Fermi surface angle  $\theta$  increasing from top to bottom. In the non-superconducting sample (Fig. 20d) we see a highly anisotropic energy gap which decreases monotonically from a maximal value at  $\theta=0$ , to zero at  $\theta=45$ . Even though there are no sharp coherence peaks at any angle, there is a clearly discernable lowenergy gap. This is the pseudogap at low temperature (16 K) in the non-superconducting sample. With increasing doping we move from the non-superconductor (Fig. 19d) to the highly underdoped superconductor (Fig. 20e), whose EDCs look qualitatively similar to those in Fig. 20d, except for the appearance of observable coherent quasiparticle peaks at the gap edge at each angle on the Fermi surface. These peaks grow in strength with increasing doping (Fig. 20f and g). We note that the energy gap evolves smoothly going from the insulator (Fig. 20d) to the optimally doped superconductor (Figs. 20e to g) as the doping increases. Much of the

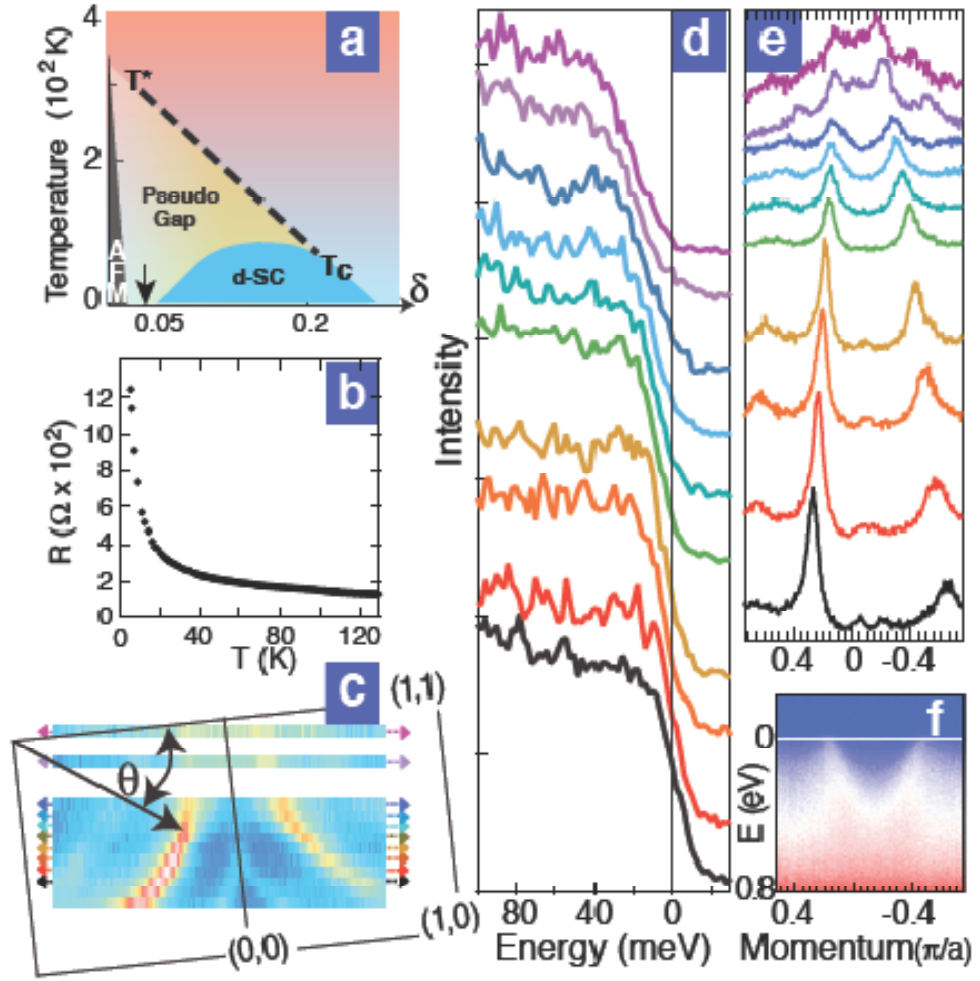


Figure 19. Data for non-superconducting samples. (a) Schematic phase diagram of  $\text{Bi}_2\text{Sr}_2\text{CaCu}_2\text{O}_{8+\delta}$  in the hole-doping ( $\delta$ ), temperature ( $T$ ) plane. The arrow indicates the doping level of the non-superconducting thin film samples whose data are shown in subsequent panels. (b)  $T$ -dependence of the resistance showing an insulating upturn. (c) Low-energy ARPES intensity at  $T=16$  K

intensity of the EDCs in Fig. 20d can be traced to the existence of a large background that is present for all ks in the zone. The origin of this background is not entirely clear, though it can be readily identified as the ARPES spectra for unoccupied states ( $k$  much beyond  $K_f$ ), or extracted from the flat ( $k$ -independent) part of the MDCs[61], and is plotted in Fig.20b. We note that following the signal, the intensity of the background also continuously decreases as the doping decreases (See supplemental information). If this background is subtracted from the data in Fig. 20d, we obtain the symmetrized results shown in Fig. 20c, which further emphasize the presence of a low energy pseudogap ( $\theta=0$ ) and the node ( $\theta=45$ ).

### 5.5 Anisotropic gap of insulating and superconducting samples

In Fig. 21 we show the angular anisotropy of the spectral gap for all our thin film and single crystal samples. The superconducting samples were measured at temperatures between 16K and 40K, well below their  $T_c$ ; the non-superconducting sample was measured at 16 K. The energy gap for superconducting samples was determined from half the spacing between coherence peaks in symmetrized spectra at their corresponding  $k_F$ . For the non-superconducting sample, we determine the low energy gap from the raw data (as indicated by the intersection of red straight lines in Fig. 3d), from the background subtracted data (Fig. 20c), and also from lineshape fits. All three methods lead to the same gap estimates within error bars. Our results confirm an earlier extrapolation[62], based on ARPES measurements above  $T_c$  for underdoped superconducting samples, that the low temperature pseudogap phase should be characterized by a node along the zone diagonal. They are also consistent with thermal conductivity ( $\kappa$  measurements[63] in highly underdoped  $\text{YBa}_2\text{Cu}_3\text{O}_{6+\delta}$  which show that the low temperature

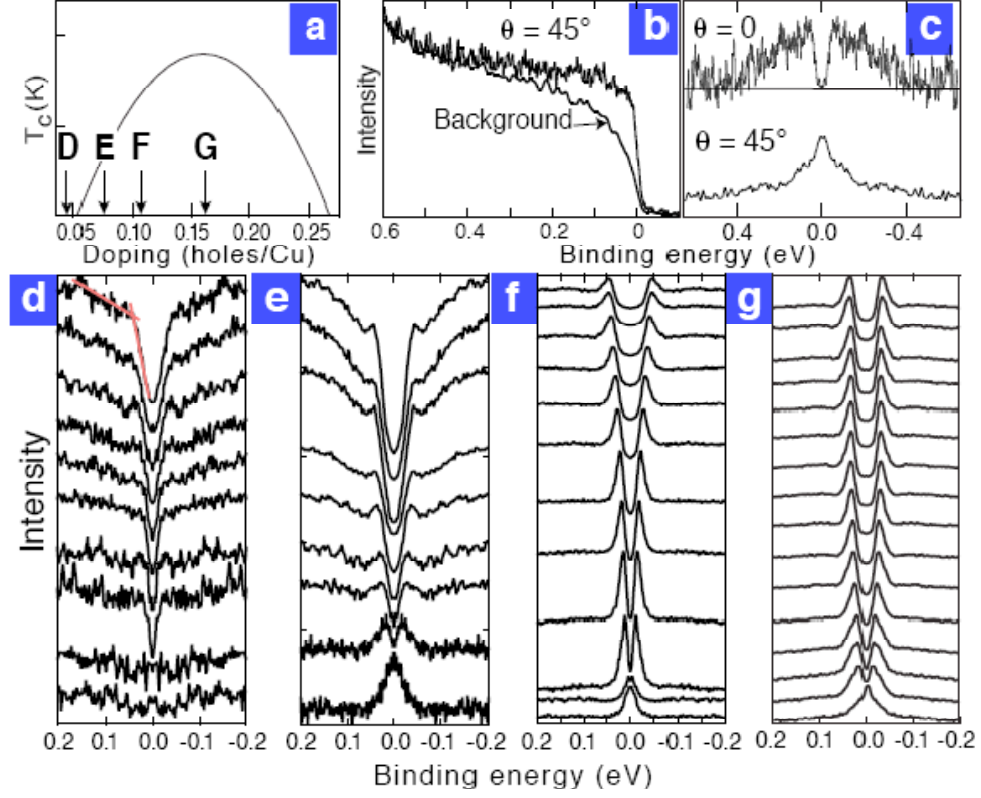


Figure 20. Spectral function vs. doping. (a) The doping levels  $\delta$  of the four samples whose spectra are shown in panels (d) through (g). The determination of  $\delta$  is described in the Supplemental section. (b) Nodal spectrum and background (see text) for the non-superconducting sample D in (a) at  $T = 16$  K. c Background-subtracted, symmetrized intensity for sample D at the antinode ( $\theta = 0$ ) showing a gap and node ( $\theta = 45^\circ$ ) with zero gap. (d) through (g) show symmetrized EDCs, without background subtraction, for (d) the non-superconducting thin film at  $T = 16$  K, (e) an underdoped  $T_c = 33$  K thin film at  $T = 16$  K; (f) an underdoped  $T_c = 69$  K single crystal at  $T = 20$  K, and (g) a near-optimal  $T_c = 80$  K thin film at  $T = 40$  K. In each panel (d) through (g) the spectra are plotted with increasing from 0 (antinode) at the top to  $45^\circ$  (node) at the bottom. Note the highly anisotropic gap seen at all four doping levels, with sharp quasiparticle peaks at the gap edge at all  $K_F$ , with weight diminishing with underdoping for all superconducting samples. Even after superconductivity is lost, we see in (d) a clear low-energy gap scale as emphasized by the red lines drawn in the top spectrum.

$\kappa$  of the insulating phase proximate to the superconducting dome is the same as that in the d-wave superconducting phase, where it is dominated by nodal excitations. Many experiments report a node in the superconducting state but a gap that deviates from the simple  $\cos(2\theta)$  form with underdoping. This behavior is attributed to two different order parameters[64], with an energy gap in the antinodal region (near  $\theta=0$ ) larger than what would be inferred by extrapolating the gap from the nodal region ( $\theta=45^\circ$ ). Our own work[65] a decade ago found evidence for a flattening of the gap around the nodes, but at that time the detectors had at least an order of magnitude lower  $k$  resolution and sparser angular sampling compared to the present study. Recent ARPES studies[66][67][68] and scanning tunneling microscopy[69][70] have also reported two gap behavior. The present results are not consistent with a two gap picture. Several other experiments also find evidence for a simple d-wave gap. These include thermal transport data[71], where the nodal gap slope extrapolated to the antinode was consistent with the maximum gap, and ARPES data on underdoped  $\text{La}_{2-x}\text{Sr}_x\text{CuO}_4$ [72], 1/8 doped  $\text{La}_{2-x}\text{Ba}_x\text{CuO}_4$  [73], and  $\text{Bi2201}$ [74][75]. Why some experiments and/or samples show two-gap behavior while others show a simple d-wave gap is not presently understood. We must emphasize here that we observe coherent quasiparticle peaks at the gap edge at all  $K_f$  for all superconducting samples down to the lowest  $T_c$ s. If, however, quasiparticle peaks were absent near the antinodes, one would erroneously estimate much larger gap values in the vicinity of these  $k$ -points. Another important question in highly underdoped samples is the possible existence of hole pockets, reported in a recent ARPES measurement[77]. We have not found any evidence for such pockets. Our MDCs always trace out a large underlying Fermi surface as in

Fig. 19c. This brings us to the implications of our main result, the observation of a d-wave like gap in a non-superconducting state that persists through the insulator-to-superconductor transition. One possibility is that our insulating sample is highly inhomogeneous and has a small fraction of superconducting regions that dominate the low-energy signal, while the less doped insulating regions produce the large spectroscopic background and dominate the transport. This inhomogeneity should be intrinsic, and not a surface phenomenon, since we have found very similar results in the superconducting samples for thin films and single crystals of  $\text{Bi}_2\text{Sr}_2\text{CaCu}_2\text{O}_{8+\delta}$ , as well as single crystals of  $\text{La}_{2x}\text{Sr}_x\text{CuO}_4$ [72] (which involved a completely different surface preparation). We emphasize that our diamagnetic susceptibility measurement puts a bound of 10 Our observations imply that the sharp quasiparticles of the d-wave superconducting state exist down to the lowest doping levels while rapidly losing spectral weight, but are no longer visible on the insulating side. Nonetheless, a low energy d-wave like gap survives the phase-disordering transition. Obviously, the node must disappear as the Mott insulator is approached, as indicated by some photoemission studies[80]. We note that we are unable to make low temperature measurements at a smaller doping than that presented here due to sample charging, suggesting a fully gapped insulator.

## 5.6 Conclusion

Summarizing, we have found spectroscopic evidence for a d-wave nodal liquid ground state in the narrow doping regime between the high  $T_c$  superconductor and the undoped Mott antiferromagnet. This quantum liquid has no superconducting order, the transport characteristics of an insulator, no sharp quasiparticles, and yet it has an energy gap that looks just like that

of a d-wave superconductor. Since the spectral gap evolves smoothly through the insulator-to-superconductor phase transition, the d-wave superconductor appears to be just a phase-coherent version of the d-wave nodal liquid[81][82][83].



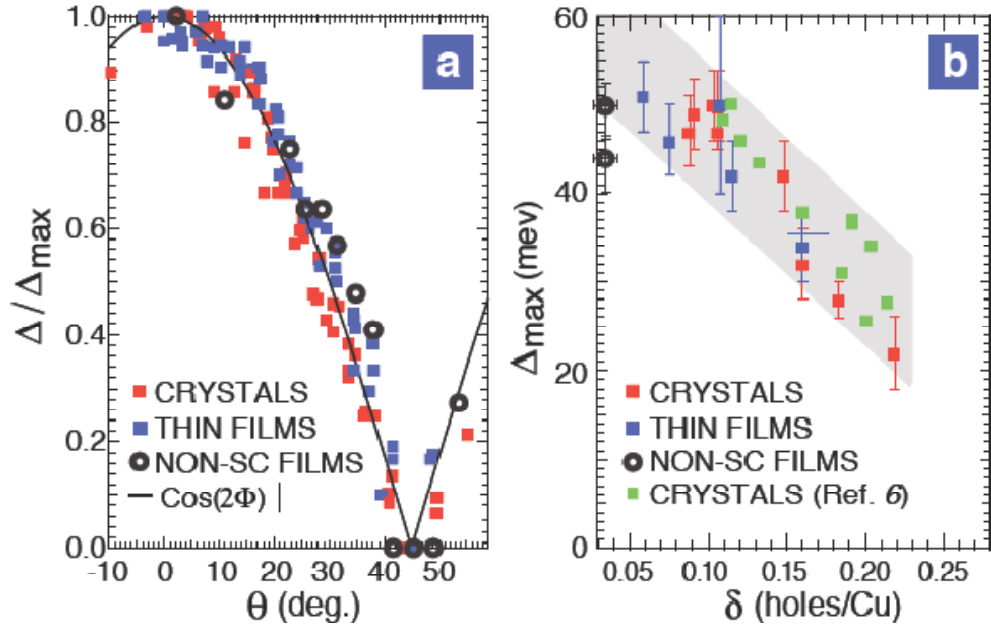


Figure 21. The spectral gap as a function of angle around the Fermi surface and doping. (a)

The spectral gap  $\Delta(\theta)$ , normalized by its maximum value at the antinode, plotted as a function of the Fermi surface angle  $\theta$ . Different colors are used for various superconducting samples (single crystals and thin films), while an open symbol is used for the non-superconducting sample. The energy gap at all doping levels is consistent with the d-wave form  $\cos(2\theta)$  shown as a black curve. (b) Maximum gap as a function of hole-doping.

Gaps of the superconducting samples are denoted by filled symbols (blue for thin films and red for single crystals measured in this work, and green for published data), while open circles are used for the non-superconducting samples.

## CHAPTER 6

### SCALING CHARACTERISTIC OF SPECTRAL FUNCTION OF UNDER-DOPED CUPRATES

#### 6.1 Motivation

We have already discussed the phase diagram of cuprates high  $T_c$  superconductor in the last chapter. As the phase diagram manifest itself, there are a pseudo-gap and conventional metal states, and in between there is strange metal state. If the single quantum critical point model shown in Fig. 12 is not evident, there must be a quantum critical part in between the metal and pseudo-gap phases, although it is hidden by the superconducting dome. In order to examine if there are any quantum critical properties, we use ARPES data to check for a proposed scaling relations in the pseudogap region. Right at the critical point, the spectral function  $A(k, \omega)$  is expected to have a universal singular dependence on  $\omega$  and  $k_{||}$  when these are both small. It is expected that this singular structure is described by a scaling ansatz of the form[84]:

$$A(k, \omega) \sim \frac{c_0}{\omega^{\frac{\alpha}{z}}} * F_0\left(\frac{c_1 * \omega}{k_{||}^z}, \frac{\omega}{T}, \frac{\omega}{\Delta}\right) \quad (6.1)$$

Where  $c_0$  and  $c_1$  are scaling coefficients,  $k_{||}$  is the deviation from the closest Fermi-surface point,  $T$  is the temperature, and  $\alpha$  and  $z$  are the scaling parameters. In order to examine this scaling function assumption, we use ARPES data measured on under-doped and over-doped  $\text{Bi}_2\text{Sr}_2\text{CaCu}_2\text{O}_{8+\delta}$  (Bi2212) samples. The function depends on three variables. If we choose

the data points where the gap value is zero, which is the Fermi-arc region in the pseudogap state, the number of variables will decrease to two. And by keeping the value of one variable constant, we can examine the scaling properties of the spectral function as a function of one variable. (The data should overlap with each other if we rescale the data as a function of scaling variables)

## 6.2 Methodolog and results

We used the following procedures to treat the raw data:

- (i) Normalization of the data. Because the absolute intensity of the spectrum we measure depends on the number of scans we did for each momentum cut in the brillouin zone. If we want to compare all the spectra together, we need to normalize the data. We use the assumption that the area under a small range of high energy away from the excitation peak should be equal for all the EDCs. Thus we can normalize the data by dividing the spectral intensity by the area under a small high energy range. This will not change the line shape of the data, but as a result we can compare data together even if the absolute intensity for each data set are quite different.
- (ii) Subtraction of the background. As we know, there is always some background in the raw ARPES data. We can subtract the background from our data to remove its effect. Here we determine the background by a spectrum that is far away from the Fermi momentum. As shown in Fig.22 (a) is the intensity map of energy and momentum (b) is the background which is the energy distribution curve at fixed momentum that far away from  $k_F$  (c) is

the spectrum before the background subtraction (d) is the spectrum after background subtraction.

- (iii) Division of the data by a resolution broadened Fermi function to remove the effects of the Fermi function. Because ARPES measures electrons, which are fermions, there is always a Fermi function cut off experimental data. The data we measure from the ARPES measurement  $I$  is proportional to  $f(T, \omega) * A(k, \omega)$ , if we want to know the information about spectral function  $A(k, \omega)$ , we need to remove the effect of Fermi function. We can remove it by symmetrization as we discussed in previous chapter or we can divide the raw data by Fermi function. We measure the spectra of gold which is polycrystalline and therefore has no momentum dependence, and fit the data with Fermi-function to determine the effective temperature of the sample, and then use the temperature to calculate the Fermi-function we need to divide the data by.

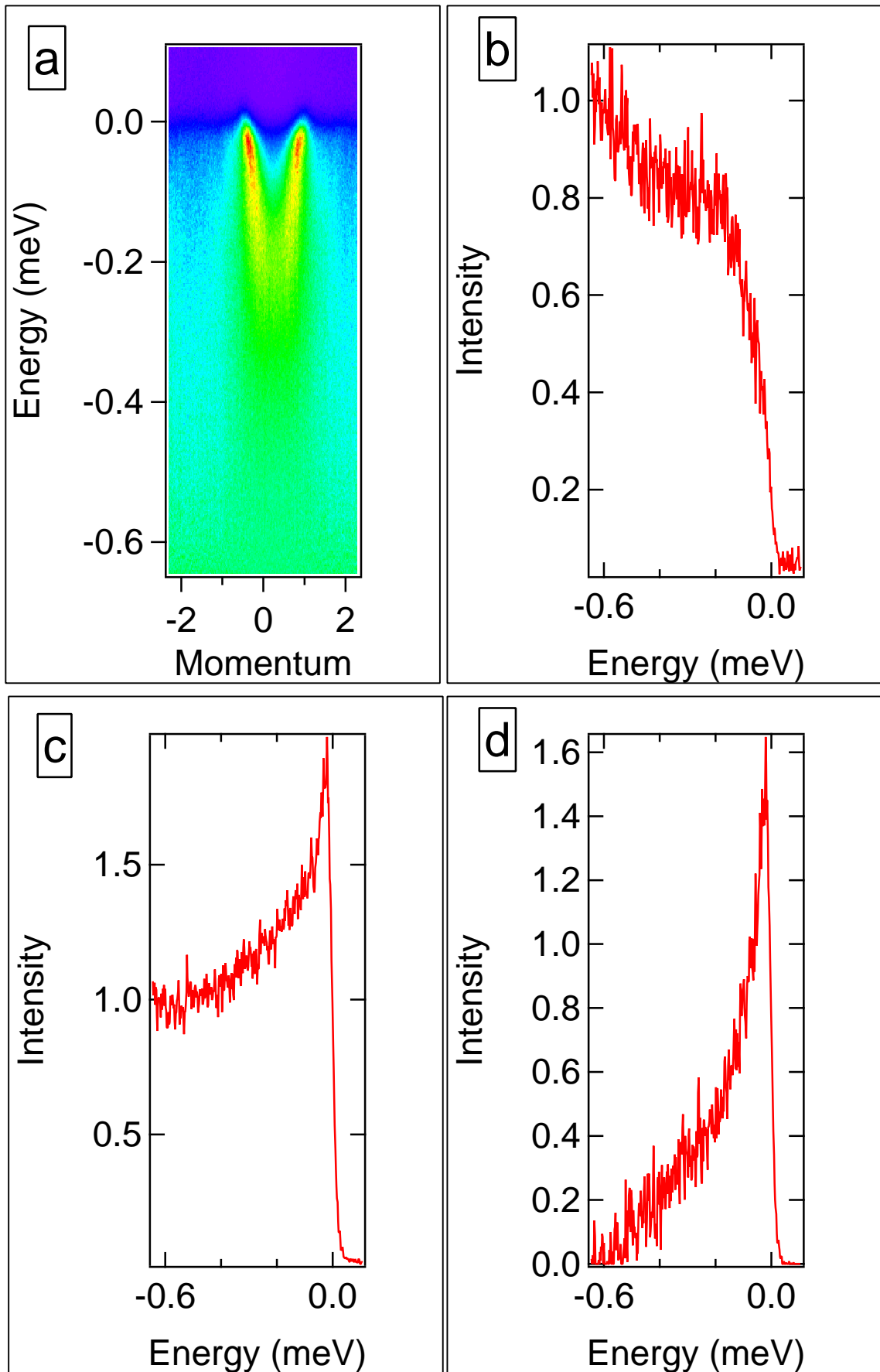


Figure 22. Background subtraction procedure. (a) intensity map of energy and momentum.

(b) EDC far away from  $k_F$  (c) the spectrum before the background subtraction (d) the

### 6.2.1 Temperature term

By choosing the data points right at the Fermi-momentum at different temperatures, we can fix the value of  $k_{||}$  at zero, therefore the first term in the scaling function  $\frac{\omega}{k_{||}}$  equals to infinity. (we can treat a variable equal to infinity in the function as irrelevant). We can vary the temperature related term to check the scaling property of the function. We can find  $k_F$  by looking for the smallest gap locus, therefore we need to plot the symmetrized EDCs and compare gap value. But here we measure the Fermi-arc part where there is no energy gap at  $k_F$ , after Fermi function division we can determine the  $k_F$  by the point where the dispersion cross the zero energy line. As shown in Fig. 23, the Y-axis is energy and X-axis is momentum channel. In the intensity map, red means high intensity, blue means low intensity. Therefore, the intensity map give us information about the dispersion of energy states, and the arrow points to the Fermi-momentum.

In Fig. 24 we show the intensity of  $A(k, \omega)$  ( data as function of energy at fixed momentum) all taken at the same Fermi momentum, at different temperatures for an under-doped  $T_c=78\text{K}$  sample. It is clear that using raw data, all the lines deviate from each other. In Fig. 25 we show the rescaled result of Fig. 24 by changing the raw data's x and y axis into the scaling function variables and choosing the right value of scaling parameters  $\alpha$  and  $z$ . ( the x-axis (energy) is rescaled to  $\frac{\omega}{T}$ , and y-axis (intensity) is rescaled to  $\text{intensity} * \omega^{\frac{\alpha}{z}}$ ). The data we present are within the energy range from -100meV to 0 meV. The scaling function works very well in this range, but if we try to examine the larger energy range, the scaling relation is not expected to work and it does not. We showed the data from -600meV to 0meV in Fig. 26 and it is obvious

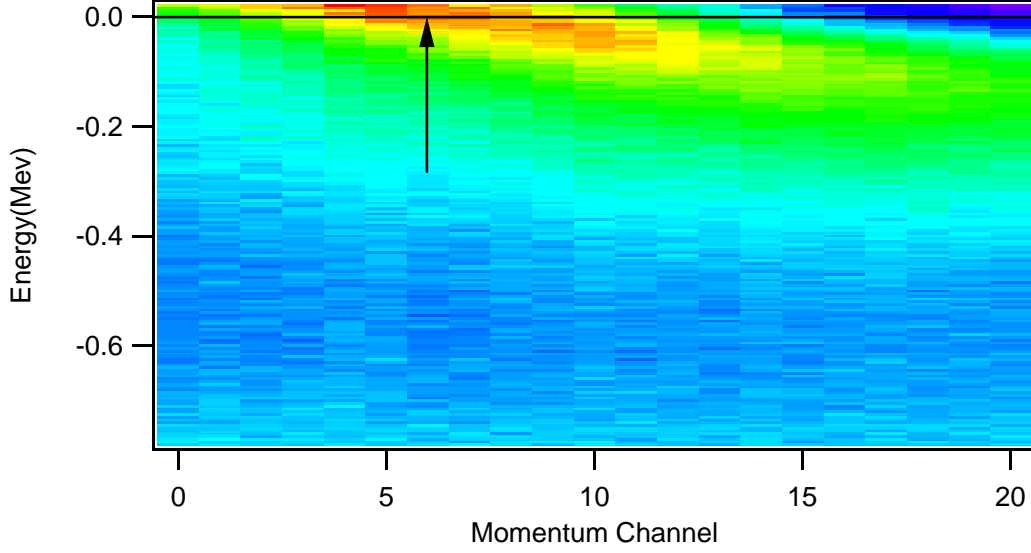


Figure 23. Fermi function divided intensity map

that within -150meV range, the spectral overlap with each other, but below that, to -600meV, the spectra are quite different from each other even after rescaling. It is worth mentioning that the values of scaling parameters are also critical for scaling to work. As discussed in reference [84], the value of  $\alpha$  is always smaller than  $z$ , and from our analysis,  $z = 1$  is the best value for scaling. In Fig. 27 we show a set of results for different scaling parameter values. One can see from the figure that there is always a best value of parameters that scales the data. In order to find the best parameter value, we carried out a chi-square analysis for the rescaled data explained below:

- (i) We fit one of the rescaled spectrum with a fitting function. For example assume that we have four rescaled EDCs at different temperatures, and we fit the rescaled EDC at highest temperature with a power function  $a * (\text{abs}(\frac{\omega}{T})^b)$ . After determine the fitting coefficients  $a$  and  $b$ , we can calculate the chi-square value for rest of the three rescaled EDCs with respect to the fitting function. The formular we use for chi-square calculation is  $(\text{intensity} * \omega^{\frac{\alpha}{z}} - a * (\text{abs}(\frac{\omega}{T})^b))^2$ .
- (ii) After the chi-square calculation for each rescaled EDC, we calculate the average value of the chi-square and plot them as a function of scaling parameter  $\alpha$  in Fig. 28. We also calculate the confidence interval for the minimum chi-square by calculate the standard deviation of minimum chi-square. Then with the assumption that the chi-square is line near the minimum value, we find the confidence interval on two sides are 0.0190231 and 0.0707679. As we can see, there is a minimum chi-square at  $\frac{\alpha}{z}=0.3$ . In figures 29 and 30, we show scaled results for other two under-doped samples, with  $T_c$ s of 85K and 47K. One can see that the data along the Fermi momentum scale with temperature for all the samples we showed. In Fig. 29, showed scaled data for an optimal-doped sample with  $T_c$  of 85K. it does not scale as well as the last two samples but it does scale better than the over-doped sample data in Fig. 30, because as we discussed in the chapter 4, the sample with  $T_c=85\text{K}$  already exhibits coherence electron, therefore the scaling function no longer describe the data very well.



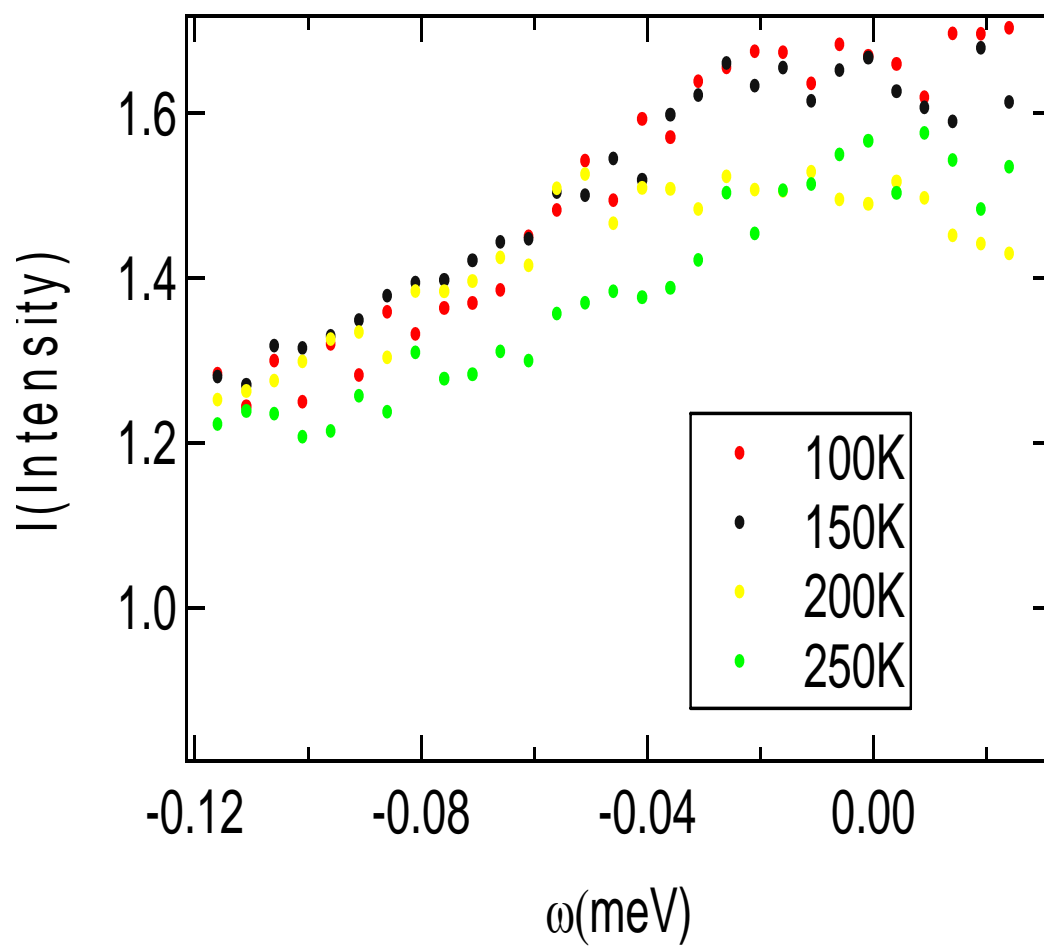


Figure 24. Raw data for under-doped ( $T_c=78\text{K}$ ), EDCs at different temperatures

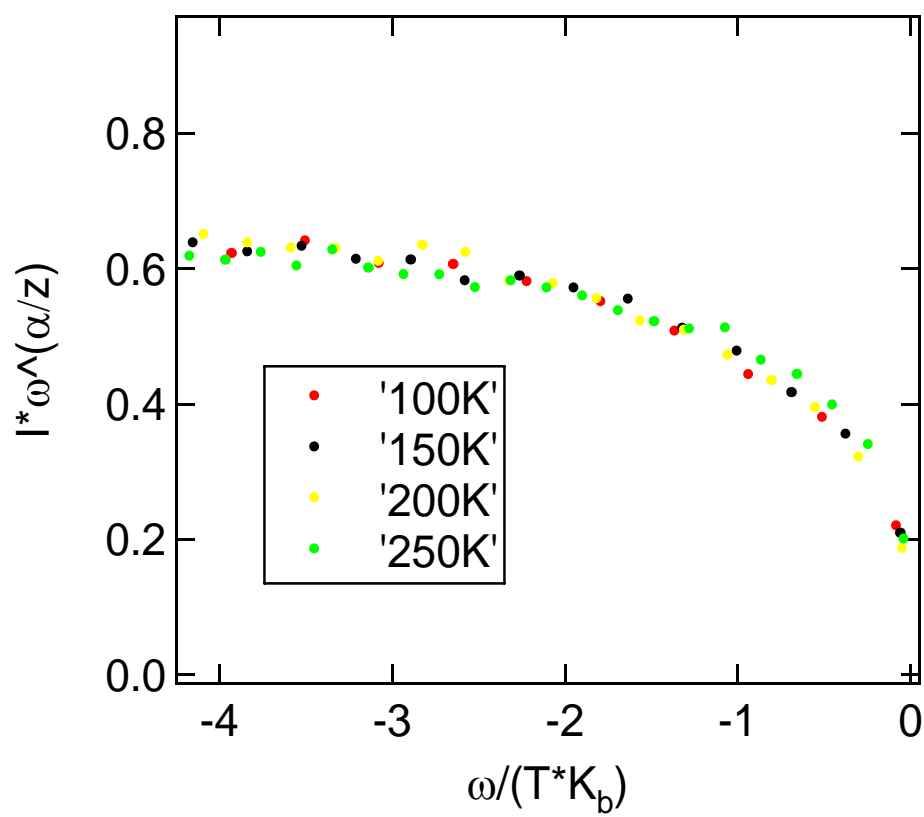


Figure 25. Scaled data for under-doped ( $T_c=78K$ ), EDCs at different temperatures

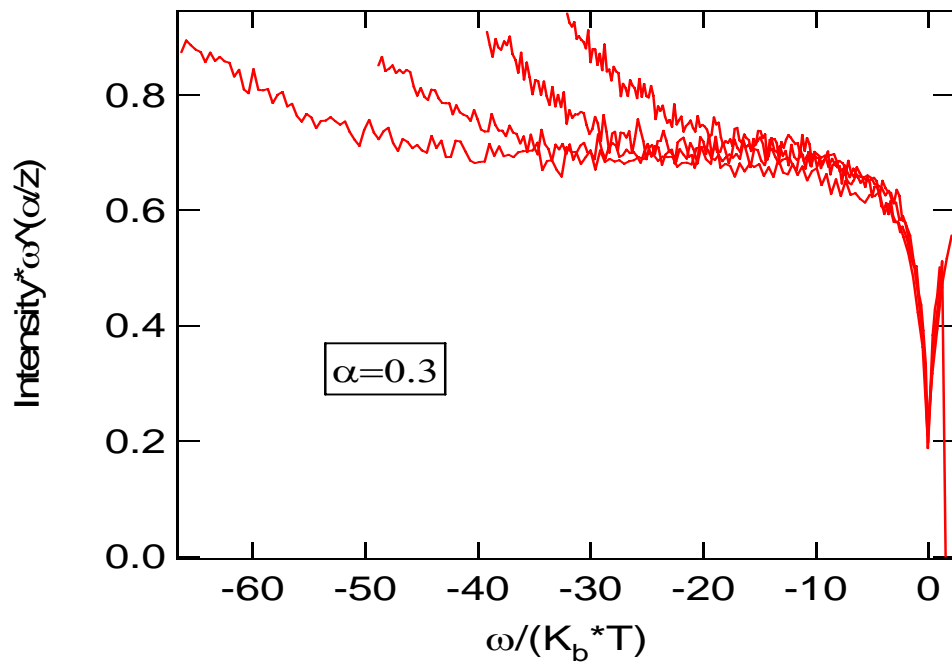


Figure 26. Scaling result for larger energy range from -600meV to 0meV

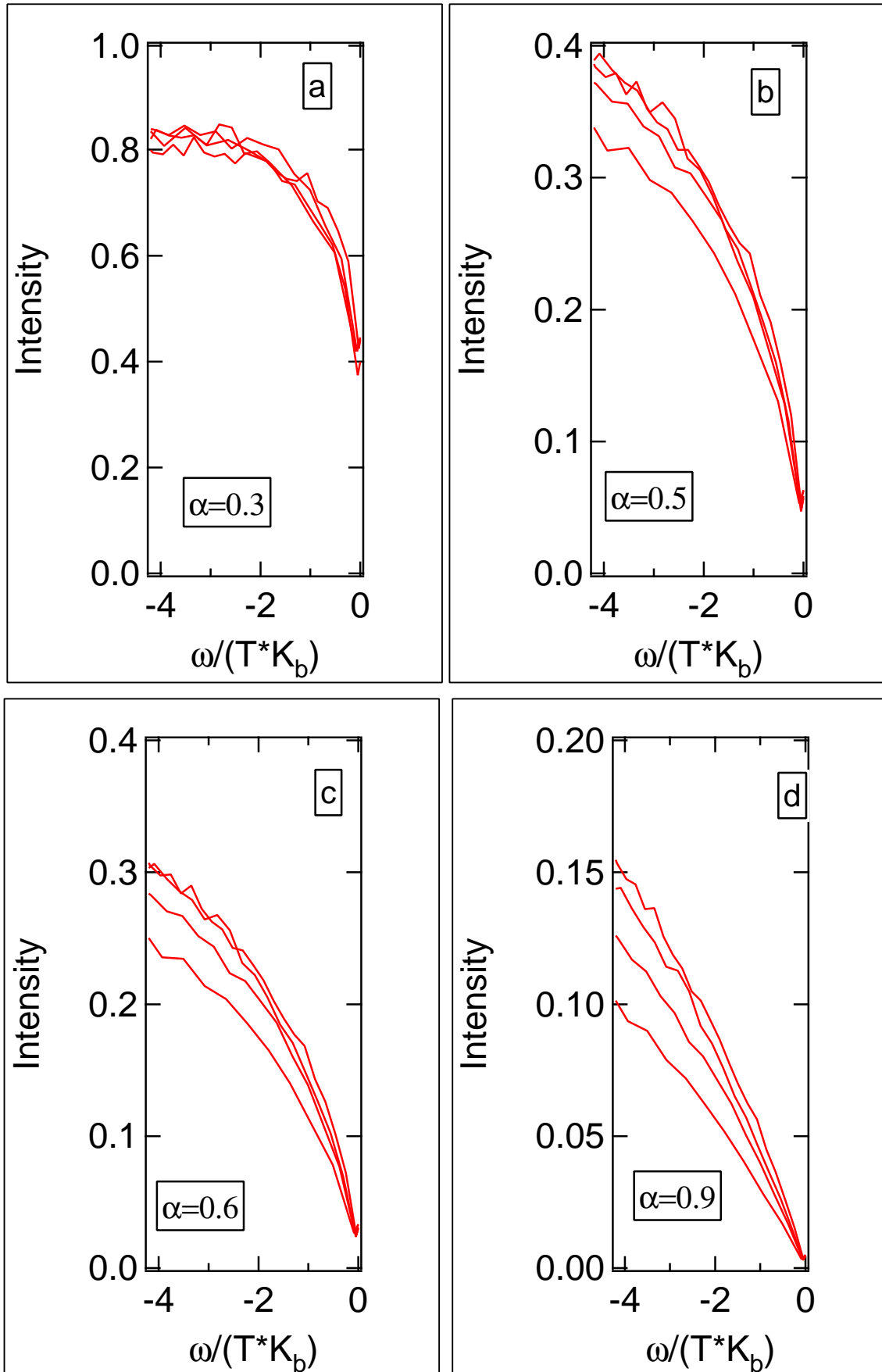


Figure 27. Comparison of different scaling parameter values (a)  $\alpha = 0.3$  (b)  $\alpha = 0.5$  (c)  $\alpha = 0.6$  (d)  $\alpha = 0.9$

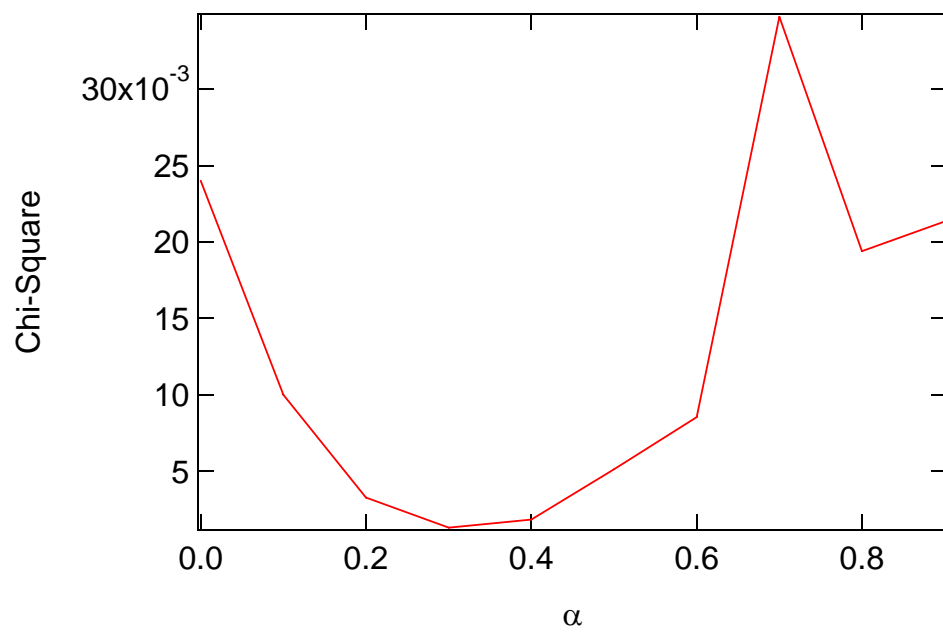


Figure 28. Chi-square value as function of scale parameter

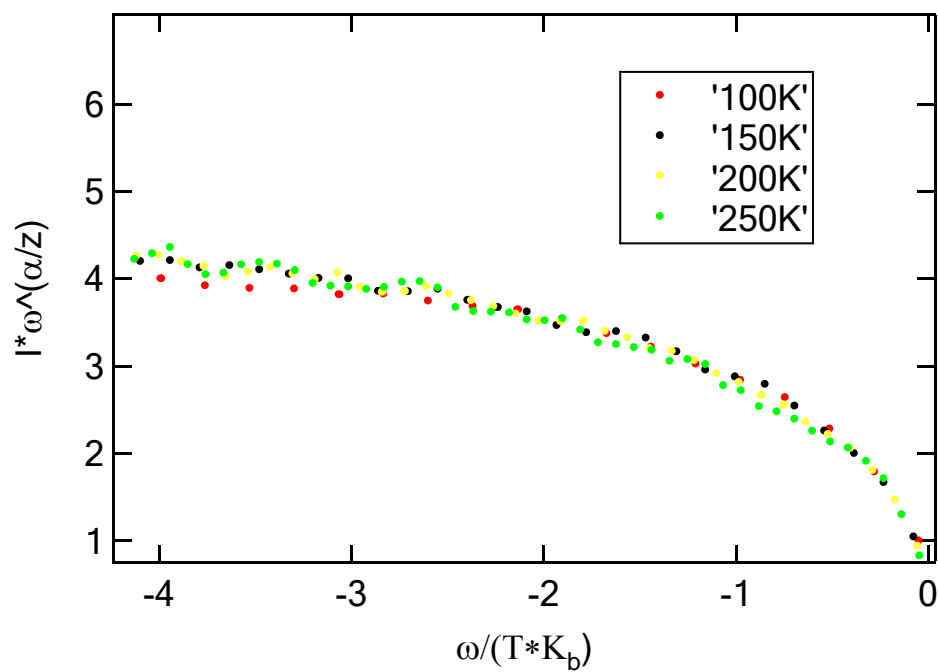


Figure 29. Scaled data for under-doped ( $T_c=47K$ ), EDCs at different temperatures

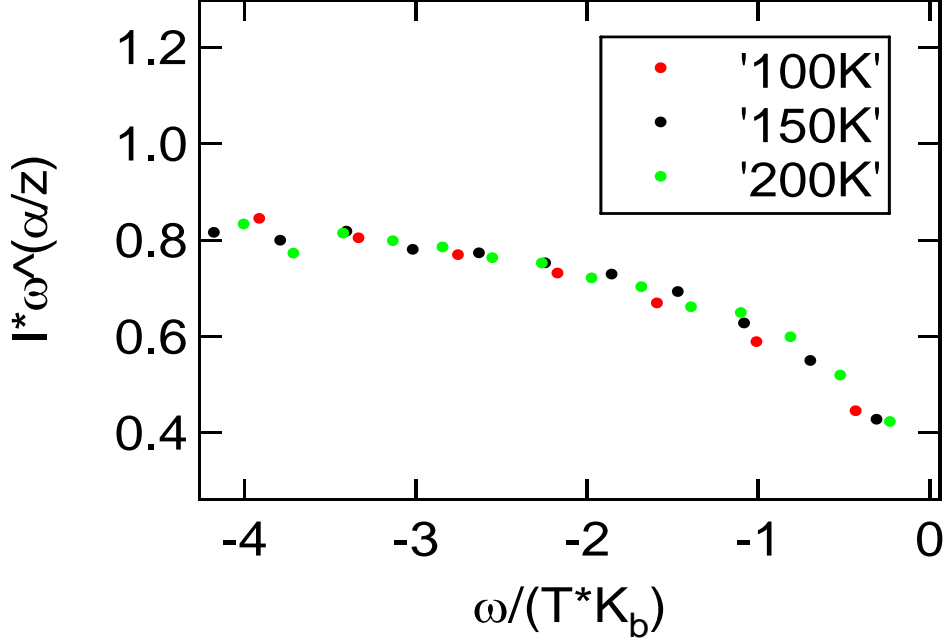


Figure 30. Scaled data for under-doped ( $T_c=85K$ ), EDCs at different temperatures

### 6.2.2 K parallel term

For  $k_{||}$  related term in the scaling function, we can fix the temperature term constant and change the  $k_{||}$  related term. But this time, it is more complicated. Because  $\omega$ ,  $T$  and  $k_{||}$  are independent variables, therefore if we want to fix one variable in the scaling function at same value for two data we want to compare, we need to measure the spectral function  $A(k, \omega)$  for two different temperatures. We measured one sample at two different temperature known as  $T_1$  and  $T_2$ . Then we choose a pair of energies  $\omega_1$  and  $\omega_2$ , which

meet the criteria that  $\frac{\omega_1}{T_1} = \frac{\omega_2}{T_2}$ . For each temperature we have a full Fermi-surface plot as shown in Fig. 31 from which we can calculate the value of  $k_{||}$  of every momentum point. Other than the Fermi-surface plot, we have constant energy plot for each temperature as well, from which we can obtain the intensity for each momentum point at fixed energy. Now with all the data above, we choose the constant energy plot ( $\omega = \omega_1$ ) at temperature  $T = T_1$  and constant energy plot ( $\omega = \omega_2$ ) at temperature  $T = T_2$ , the temperature related term  $\frac{\omega}{T}$  for two data are fixed and equal. And as energy  $\omega$  is also fixed for two data, we can change the  $k$  parallel related term by varying the  $k_{||}$ . And as we can see from the Fig. 31 when we choose different Fermi-momentum points to determine the  $k_{||}$  value, the range of available  $k_{||}$  is different, thus there will be some different in the x-axis value when we compare the data for different Fermi-momentum points. We use the following steps to obtain the data discussed above:

- (i) From each 3-D intensity map, we choose the data as function of momentum at fixed energy zero. After that we combine the data to build the zero energy contour at fixed energy zero which is the Fermi-surface. In the meantime, we make the Fermi-surface plot by the tight-binding simulation. By rotation and translation of our experiment results (caused by sample and detector orientation), we can fit the data with the tight-binding calculation and find the required momentum and energy points for our scaling analysis.
- (ii) Then, we plot the intensity and momentum value of our experimental data.



In Fig.31 we show the tight-binding Fermi-surface fit with our results. Fig.32 shows some examples of the calculated  $k_{||}$  and intensity. Fig.32 (a) is the intensity for momentum points in b Fig.32 (b) is the  $k_{||}$  for one specific Fermi momentum ( the colors are value related) In Fig.33 we plot intensity and  $k_{||}$  in 2-D, the x-axis is the point number on the line which normal to the Fermi-surface.

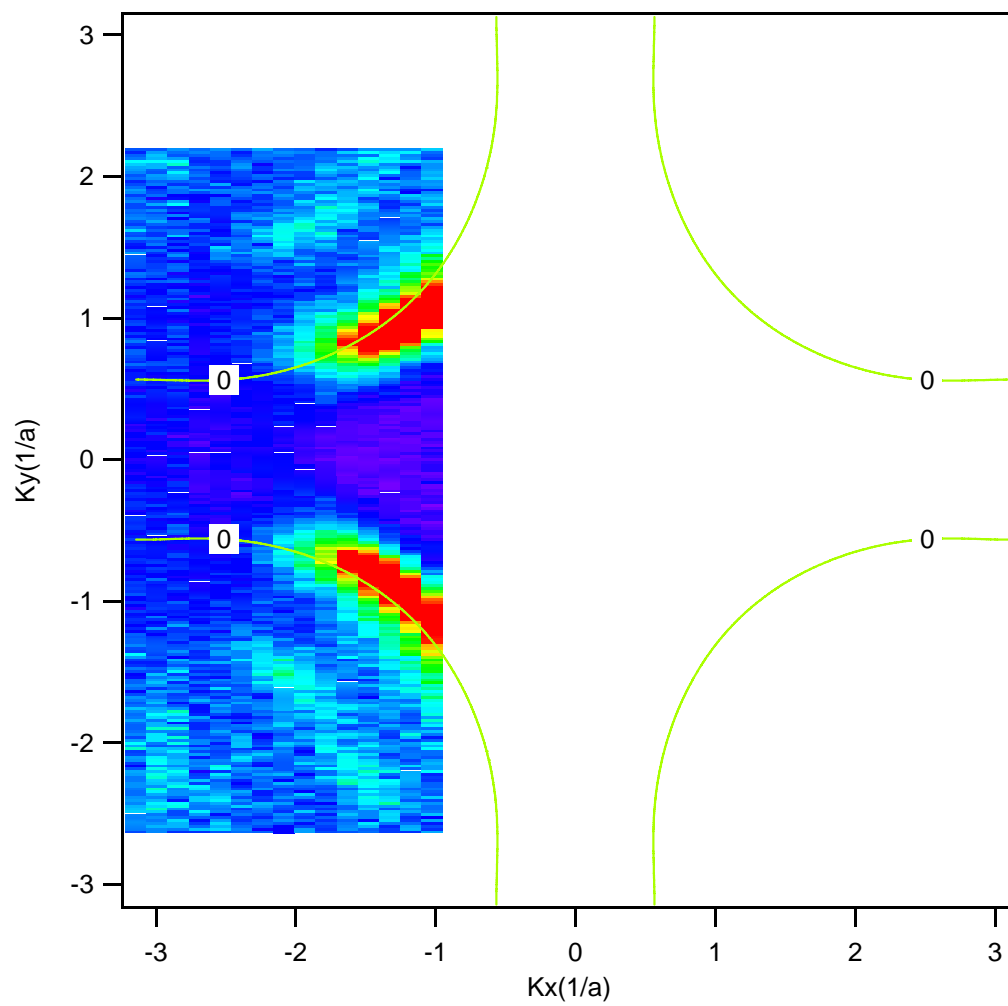


Figure 31. Tight-binding fit of the Fermi surface

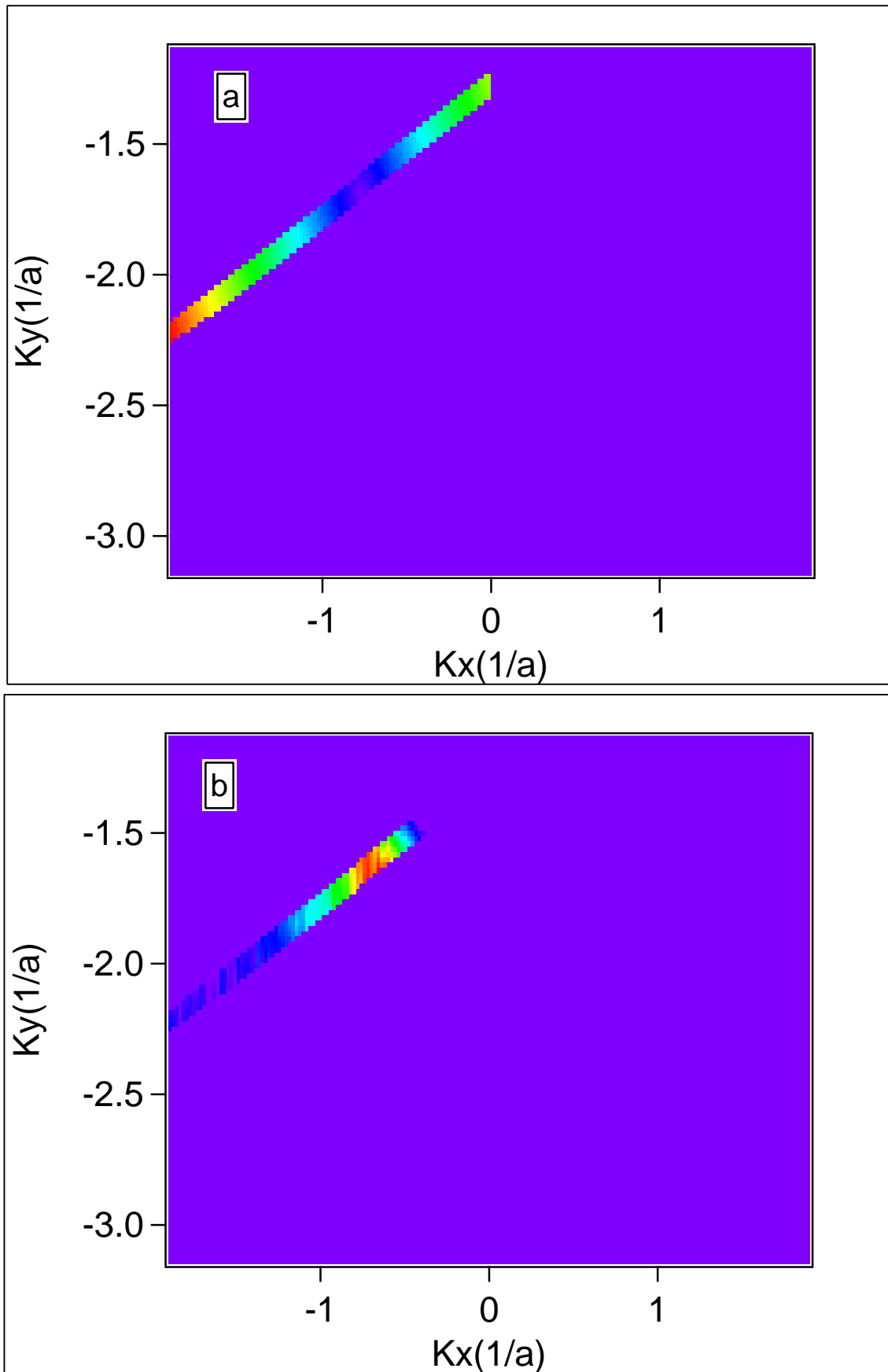


Figure 32. Intensity and  $k_{\parallel}$  value in 3D map (a) the intensity (b) the  $k_{\parallel}$

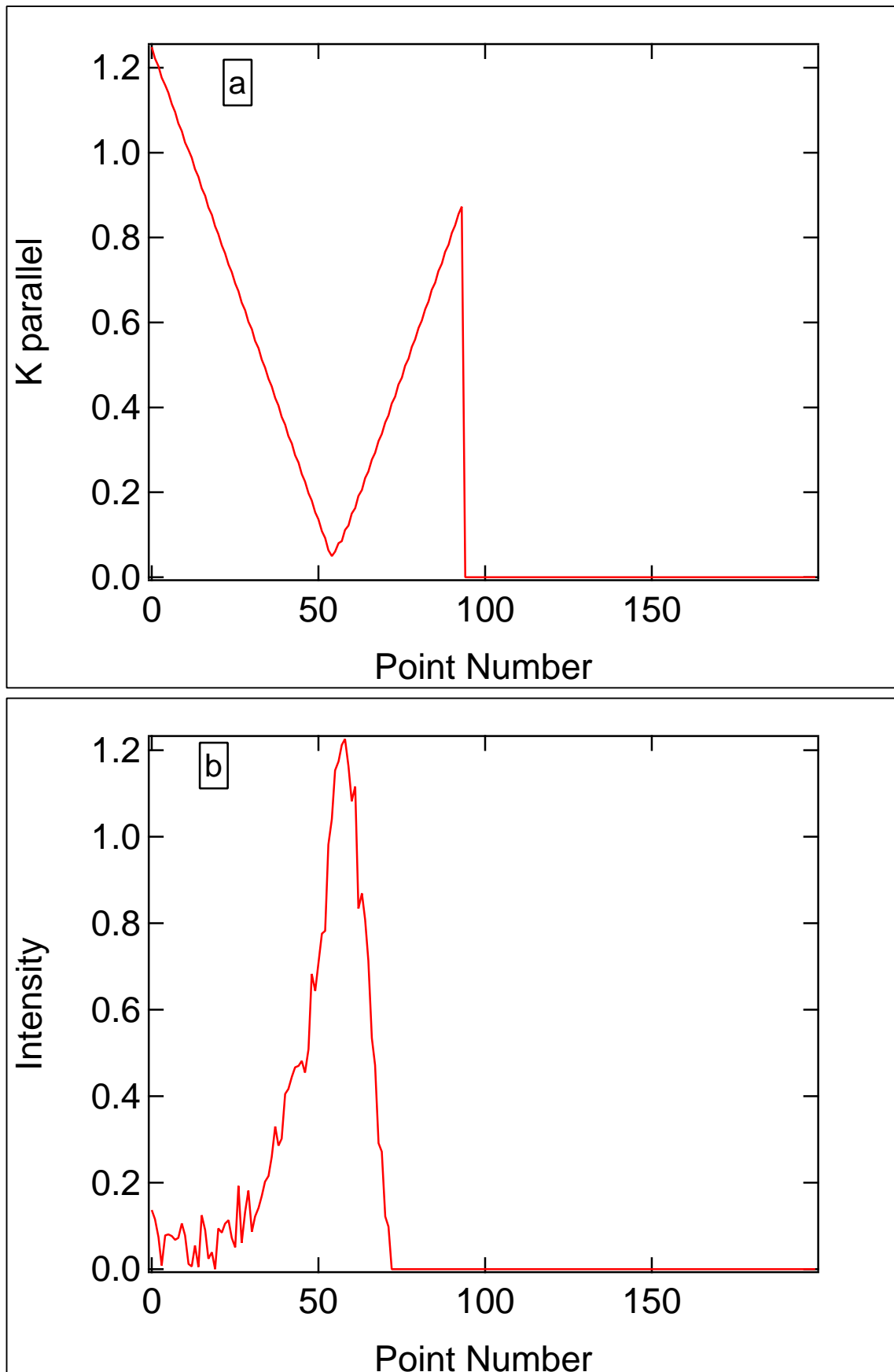


Figure 33. Intensity and  $k_{||}$  value in 2D map (a) the intensity (b) the  $k_{||}$

In the Fig.34, we show the intensity versus  $k_{||}$  data for four pairs of momentum lines at  $T_1$  with energy  $\omega_1$  and  $T_2$  with energy  $\omega_2$  for an under-doped sample whose  $T_c$  is 68K. The momentum lines is shown in Fig.37 by different color arrows. It is obvious that for the raw data all the lines are deviate from each other. In Fig.35 we show the rescaled result of Fig.34 by changing the raw data's x and y axis into the scaling function variables. (x-axis  $k_{||}$  rescaled to  $\frac{\omega}{k_{||}^z * v_F}$ , and y-axis intensity rescaled to  $\text{intensity} * \omega^{\frac{\alpha}{z}}$ ). Here we make the x-axis unitless by dividing it by Fermi velocity  $v_F$ . And in Fig.36 we show the unscaled and scaled result for an under-doped sample whose  $T_c$  is 80K. For the momentum term scaling, we also find the value of scaling parameter for best scaling, and plot them as a function of Fermi surface cut as shown in Fig.38 (each red line means one degree). Because this time the value of  $z$  is also taken into account. We find out that the best value of  $z$  for the scaling function to work is around one. We plot the different scaling result for different value of  $z$  in figures 39 and 40. As we can see, when  $z$  is larger than one, because the  $k_{||}$  value increases as times of unit momentum value, the difference between first few  $k_{||}$  with others is already very large. Therefore if we use large  $z$  value, this difference will increase exponentially, and as a result we can only have very few  $\frac{\omega}{k_{||}^z * v_F}$  value to compare which will make the scaling meaningless. And for small  $z$  value, from the result in Fig. 40, with the value of  $z$  decrease, the rescaled spectral will deviate from each other more and more which means the scaling relation does not work for smaller  $z$  value. For the temperature term scaling as we discussed in the last section, the scaling function only works very well in a certain range of energy. Same as the temperature term scaling for

the  $k_{||}$  term scaling, in Fig.41 we also show the scaling result for smaller range of  $k_{||}$  than result in Fig.35. We can see that after a certain range of  $k_{||}$  the rescaled data begin to deviate and not as good as the result for smaller range of  $k_{||}$ .

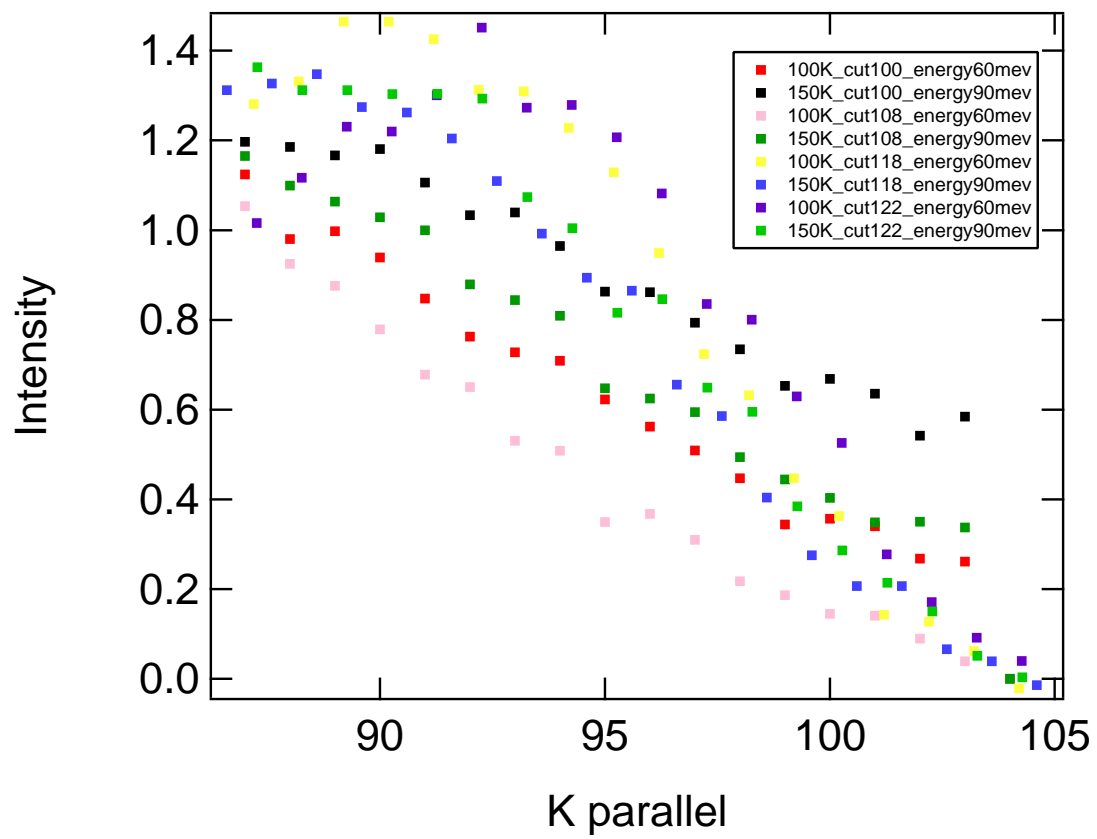


Figure 34. Raw data for under-doped ( $T_c=68\text{K}$ ), MDCs for different temperature

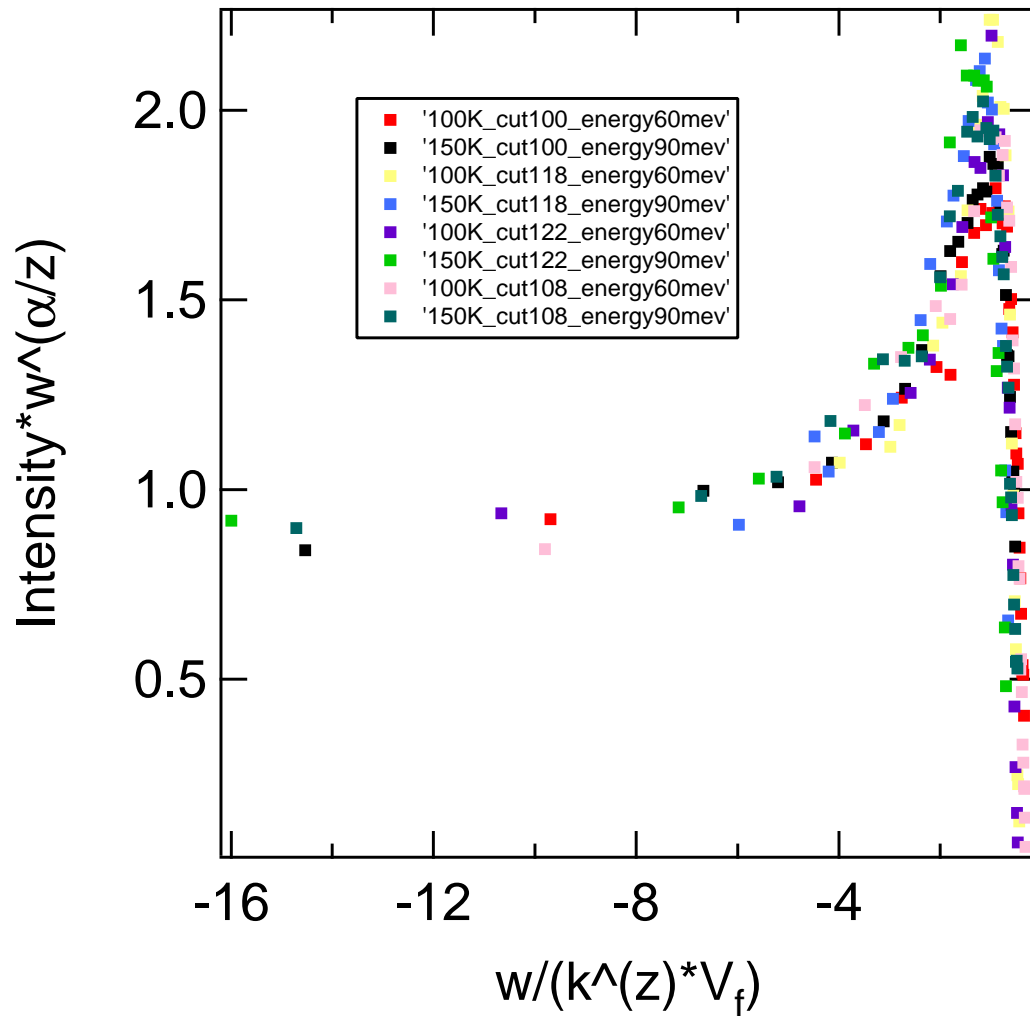


Figure 35. Scaled data for under-doped ( $T_c=68\text{K}$ ), MDCs for different temperature



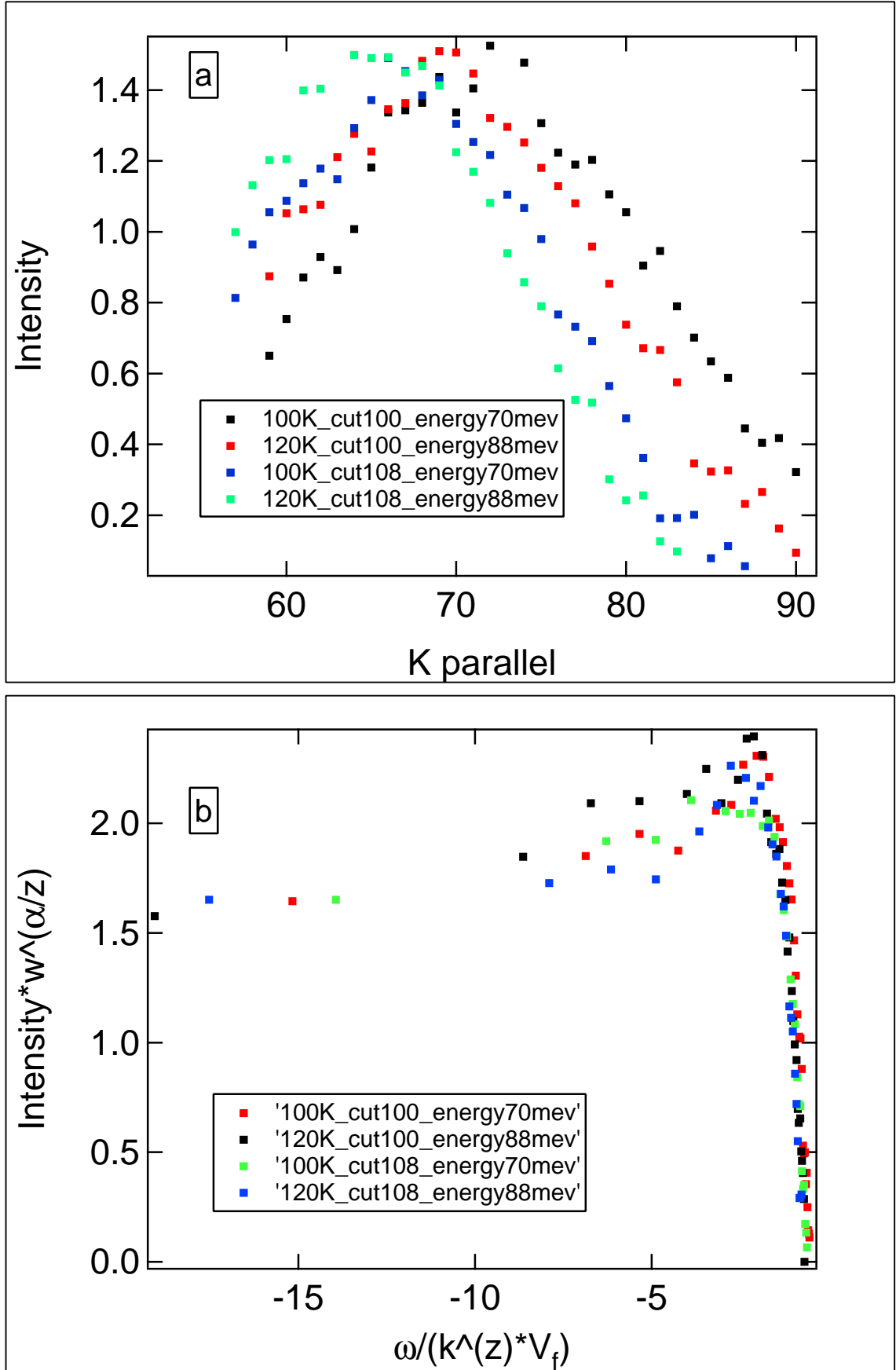


Figure 36. Unscaled and scaled data for under-doped ( $T_c=80\text{K}$ ), MDCs for different temperature

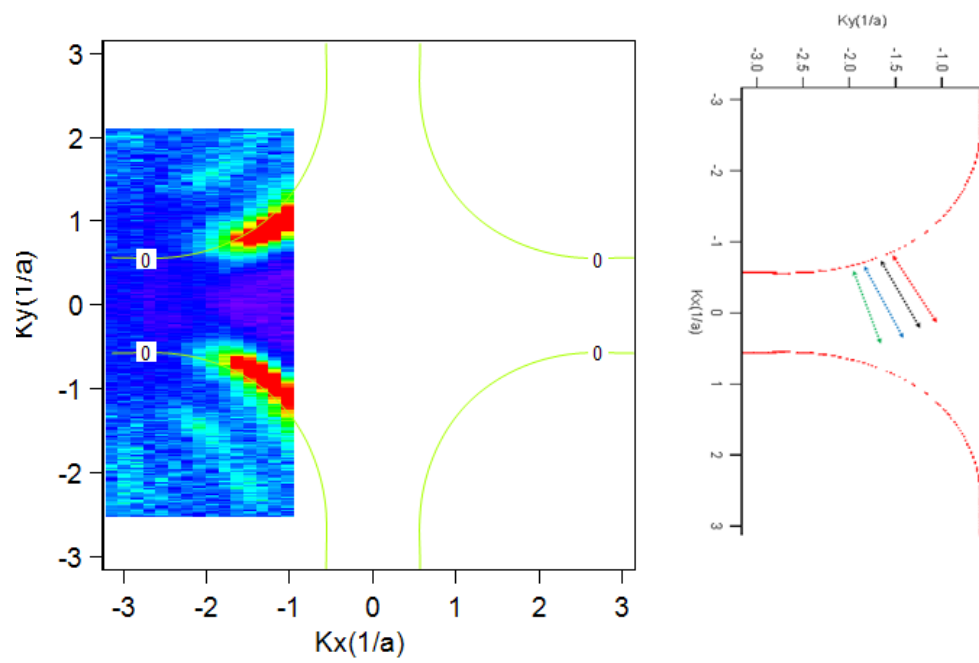


Figure 37. Momentum lines chosen for Fig.33, 34

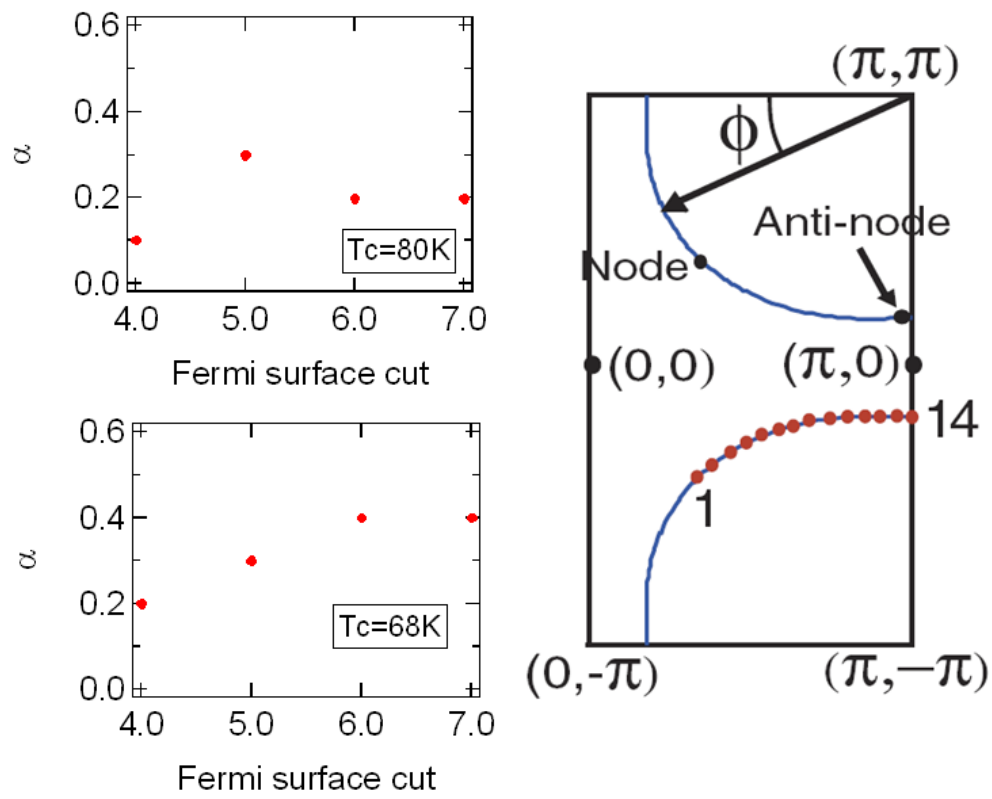


Figure 38. Scaling parameter versus Fermi-surface cut

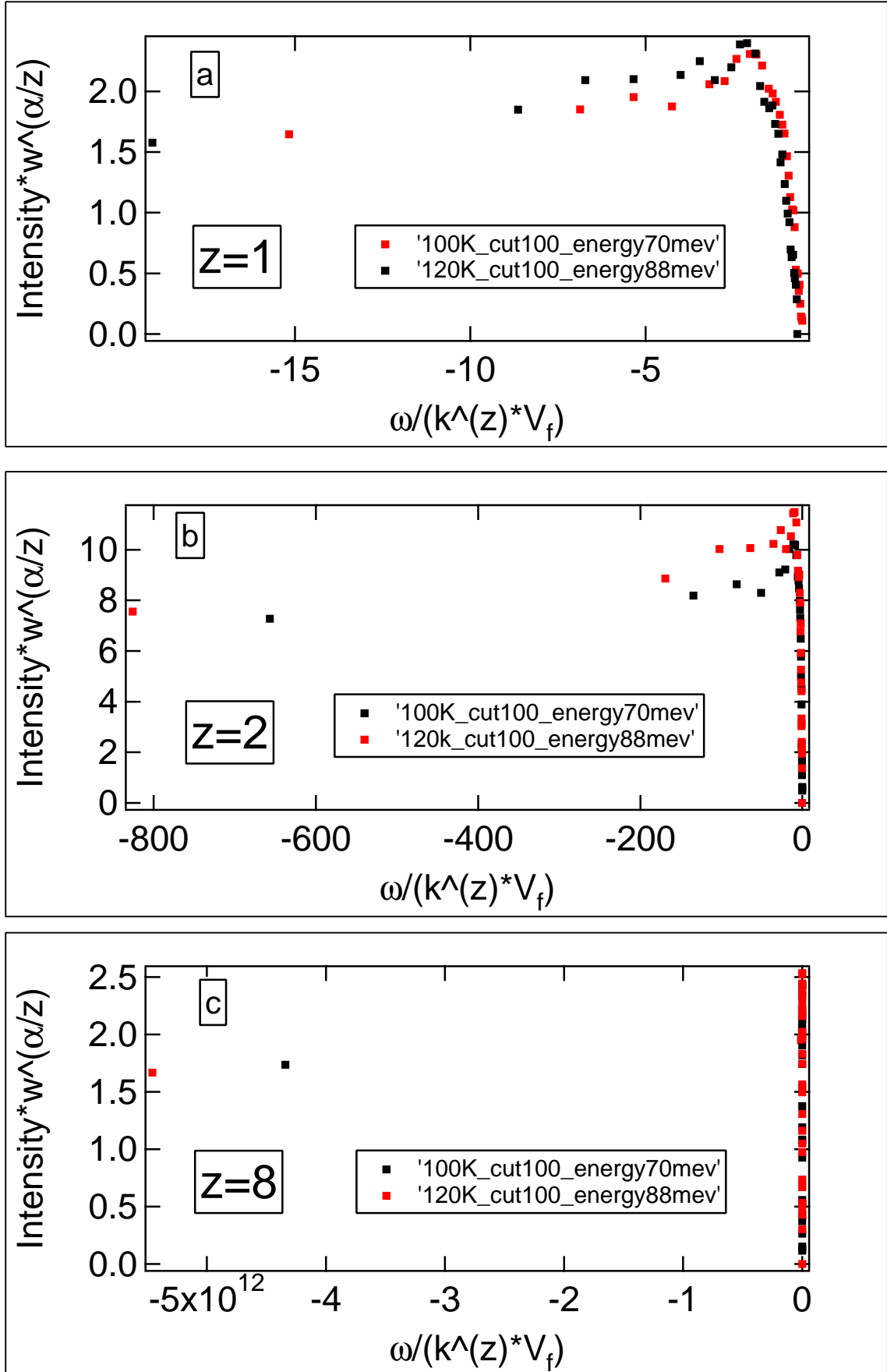


Figure 39. Scaling result for different value of  $z$  (a) result for  $z=1$  (b) result for  $z=2$  (c) result for  $z=8$

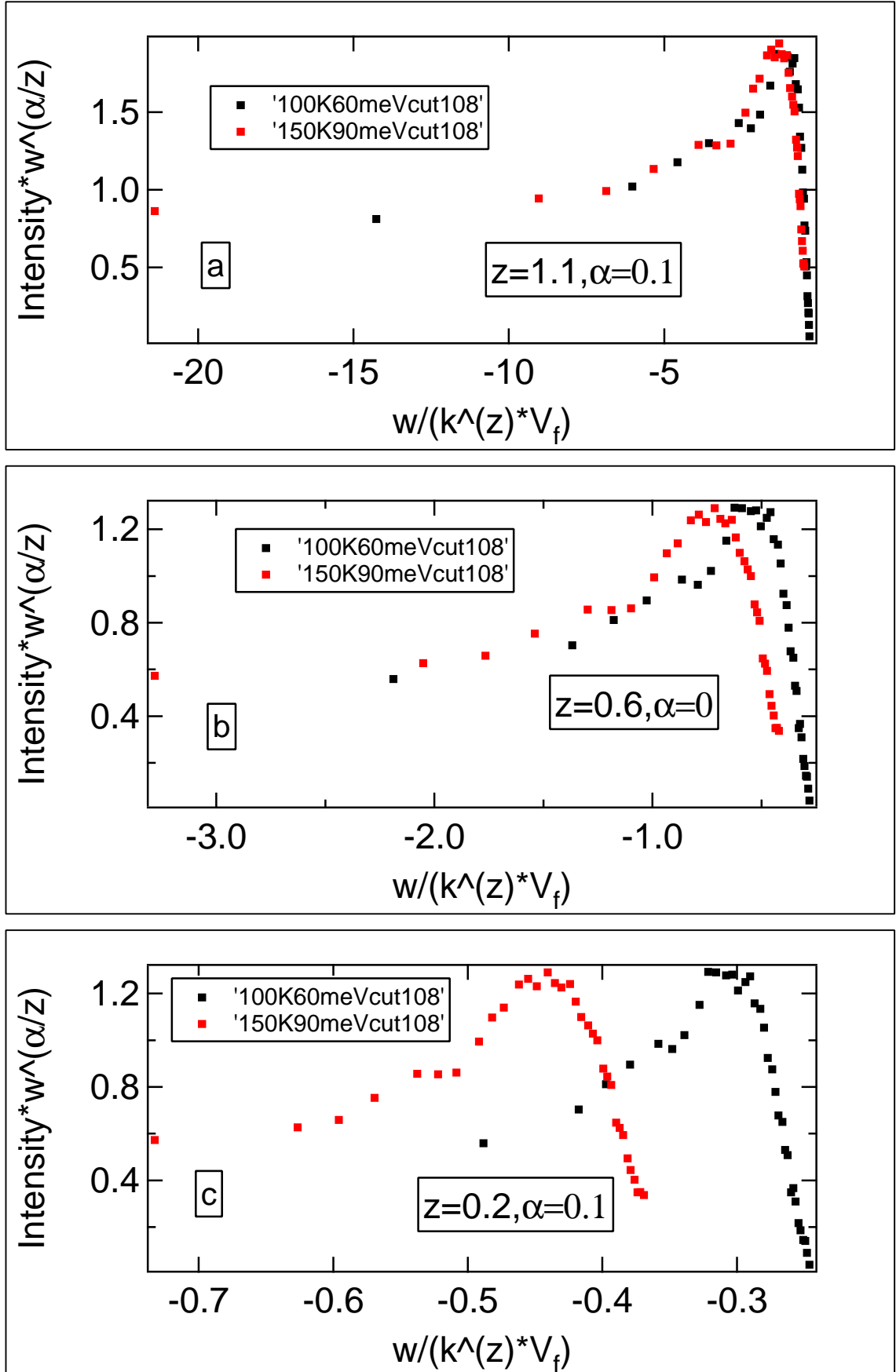


Figure 40. Scaling result for different value of  $z$  (a) result for  $z=1.1$  (b) result for  $z=0.6$  (c) result for  $z=0.2$

In order to show that the scaling property is the special characteristic of the pseudogap states. We did the same analysis for an over-doped sample with a  $T_c=67\text{k}$ . As shown in Fig. 42, the data for this over-doped sample does not scale. Also, the chi-square value, the over-doped sample has much higher chi-square value compare to under-doped sample. We can see that the ChiSquare decreases indefinitely as the value of  $\frac{\alpha}{z}$  increase. We also do not find scaling in the gapped region for the Brilliumn Zone. This might because as  $\frac{\alpha}{z}$  increase, the energy effect is more dominant. The reason is that the value of energy is very small near the peak, so if  $\frac{\alpha}{z}$  is large  $\omega^{\frac{\alpha}{z}}$  is smaller and it will depress the curve feature. Thus we think scaling for a large value of  $\frac{\alpha}{z}$  is an artificial effect.

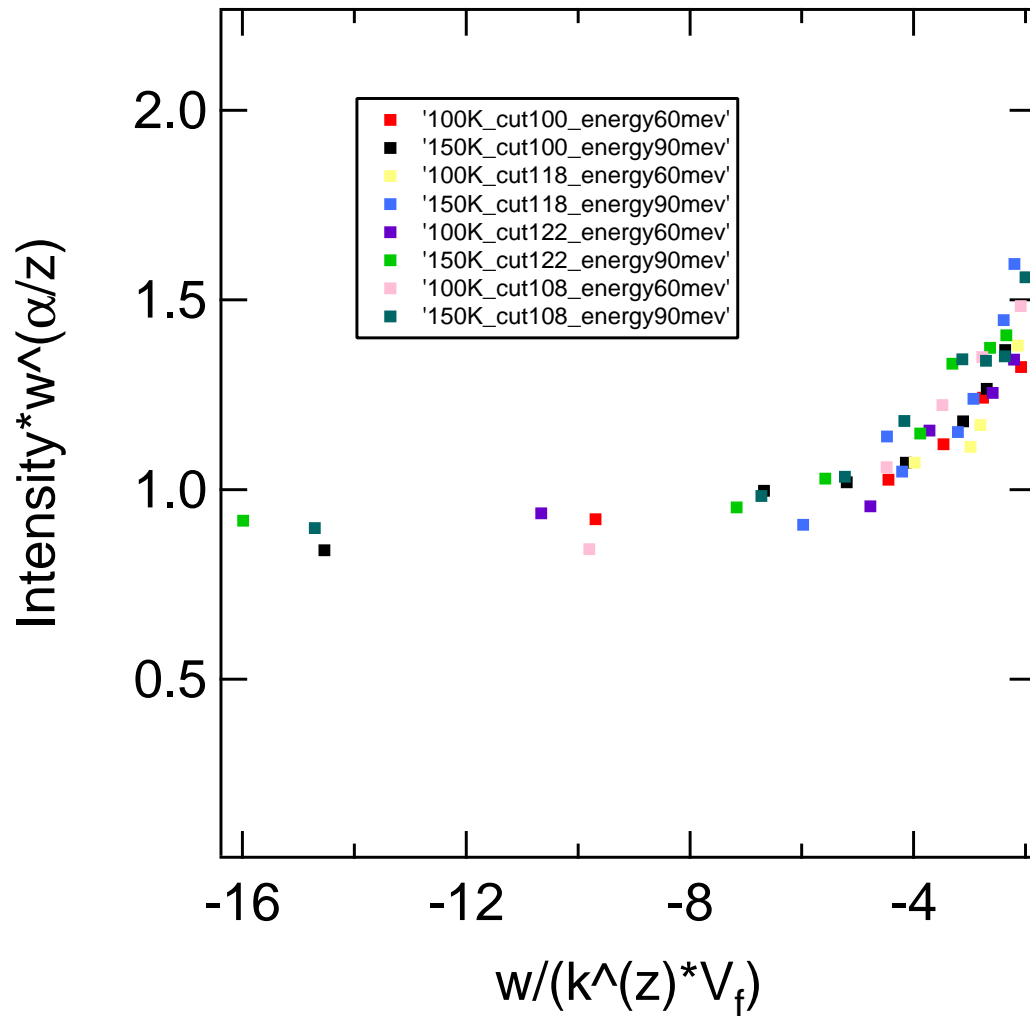
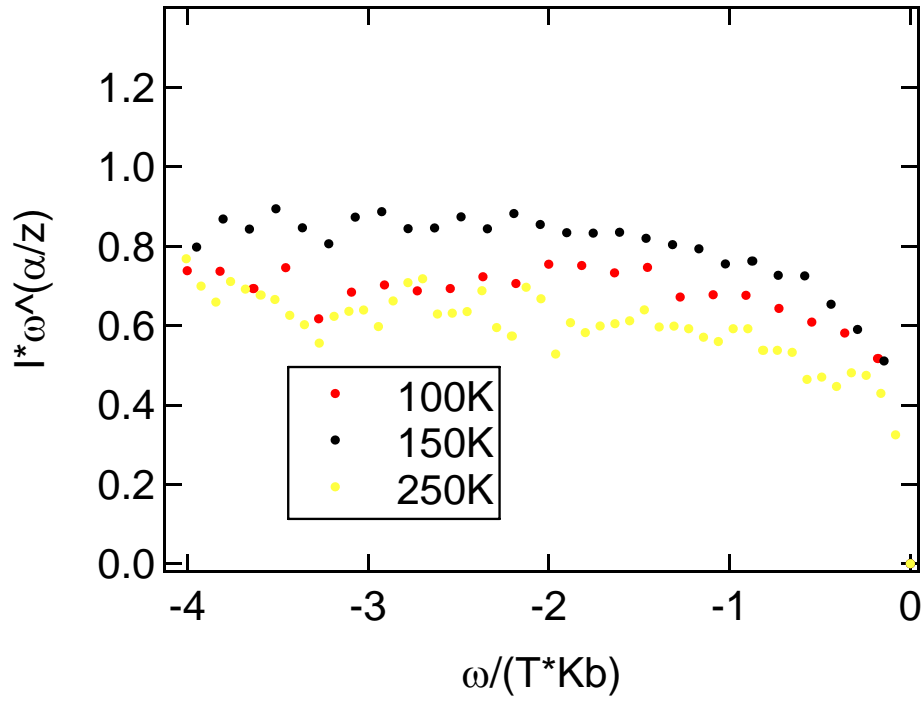
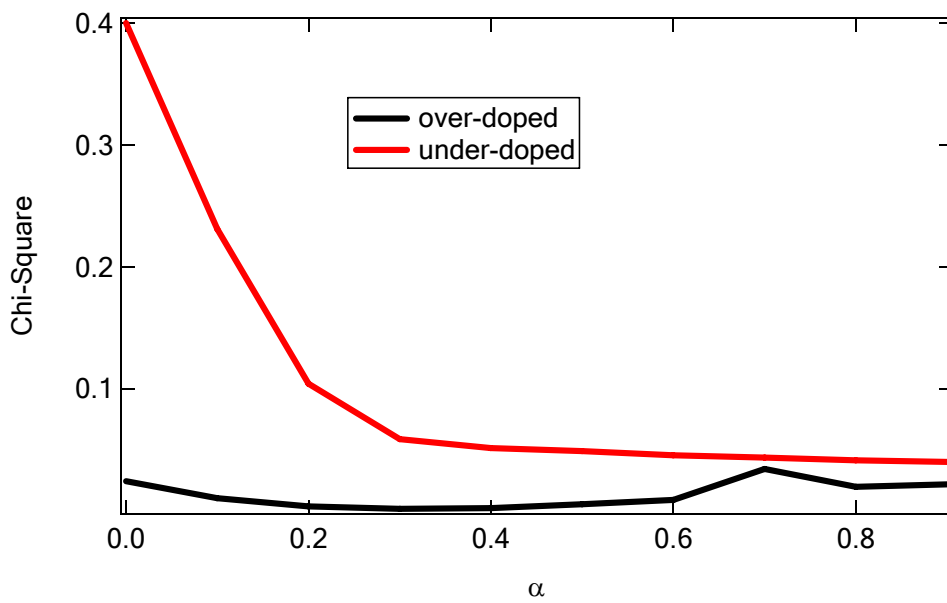


Figure 41. Scaling result for smaller  $k_{||}$  range



a



b

Figure 42. Scaled data for over-doped ( $T_c=67K$ ) and chi-square (a) scaled data (b) chi-square value vs parameters



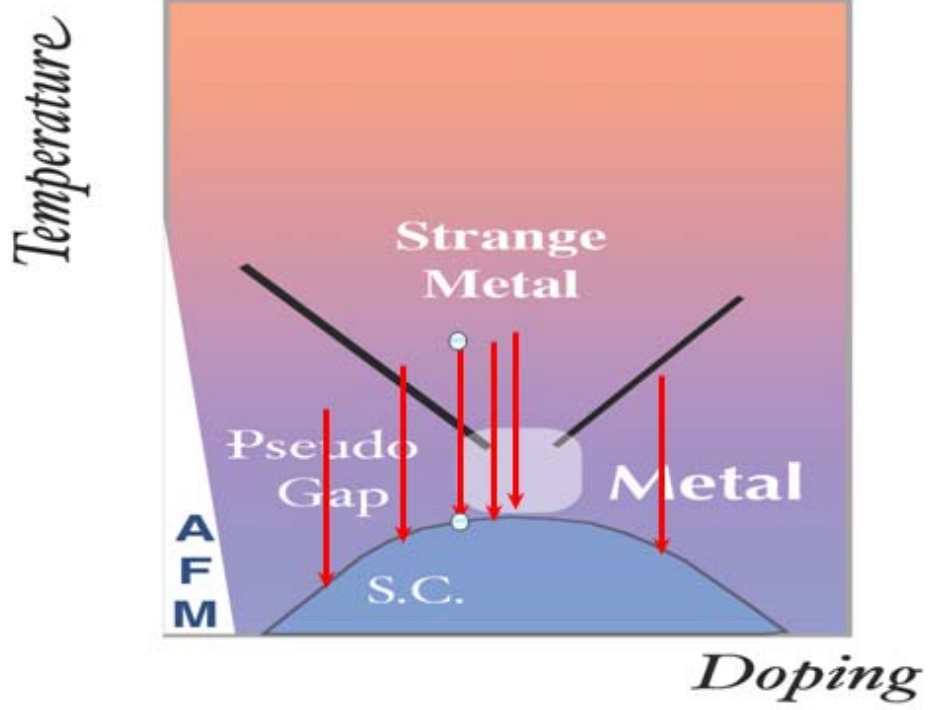


Figure 43. Measured samples in phase diagram

### 6.3 Conclusion

In summary, we use the  $\text{Bi}_2\text{Sr}_2\text{CaCu}_2\text{O}_{8+\delta}$  (Bi2212) sample data to evaluate the scaling function. We found that, for five different under-doped samples in the Fermi-Arc region the scaling function works very well. And for the over-doped sample, the data shows that the scaling function does not work. In Fig. 43, we show the samples we measured in the HTSCS phase diagram. Therefore, there is a universal scaling relation is only shared by under-doped  $\text{Bi}_2\text{Sr}_2\text{CaCu}_2\text{O}_{8+\delta}$ .

## CITED LITERATURE

1. Utpal Chatterjee Angle Resolved Photoemission Spectroscopy Study of High Temperature Superconductors. 2007.
2. H.Kammerlingh Onnes *Commun. Phys. Lab. Univ. Leiden. Suppl.* 29(Nov. 1911)
3. G.D.Mahan. *Many Particle Physics*. Plenum Press, 1990.
4. I. E. Dzyaloshinski A. A. Abrikosov, L. P. Gorkov. *Methods Of Quantum Field Theory In Statistical Physics*. Prentice-Hall, Inc, 1963.
5. J. P. Sethna. *Order parameters, Broken Symmetry and Topology*, volume 15. Addison-Wesley, 1992.
6. P. W. Anderson. More is different. *Science*, 177:393, 1972.
7. J. London F. London. *Proceedings of the Royal Society of London*, A149:71, 1935.
8. V. L. Ginzburg and L. D. Landau. *Zh. Eksperim. i. Teor. Fiz*, 20:1064, 1950.
9. J. Bardeen, L. N. Cooper, and J. R. Schrieffer. Theory of superconductivity. *Phys. Rev.*, 108(1175), 1957.

10. L. N. Cooper. Bound electron pairs in a degenerate fermi gas. *Phys. Rev.*, 104:1189, 1956.
11. W. S. Coark, B. B. Goodman, C. B. Satterthwaite, and A. Wexler. Exponential temperature dependence of the electronic specific heat of superconducting vanadium. *Phys. Rev.*, 96:1442, 1954.
12. W. S. Coark, B. B. Goodman, C. B. Satterthwaite, and A. Wexler. Atomic heats of normal and superconducting vanadium. *Phys. Rev.*, 102:656, 1956.
13. C. A. Reynolds, B. Serin, W. H. Wright, and L. B. Nesbit. Superconductivity of isotopes of mercury. *Phys. Rev.*, 78:487, 1950.
14. J. R. Schrieffer. *Theory of Superconductivity*. Preseus Books, 1964.
15. G. Bednorz and K. A. Muller. Possible high  $T_c$  superconductivity in Ba-La-Cu-O system. *Z. Phys. B*, 64:189, 1986.
16. M. K. Wu. Superconductivity at 93k in a new mixed-phase Y-Ba-Cu-O compound system at ambient pressure. *Phys. Rev. Lett.*, 58:908, 1987.
17. P. A. Lee, N. Nagaosa, and X.-G. Wen. Doping a mott insulator: Physics of high -temperature superconductivity. *Rev. Mod. Phys*, 78:17, 2006.

18. E. Dagotto. Correlated electrons in high -temperature superconductors. *Rev. Mod. Phys*, 66:763, 1994.
19. S. A. Kivelson, I. P. Bindloss, E. Fradkin, V. Oganesyan, J. M. Tranquada, A. Kapitulnik, , and C. Howald. How to detect fluctuating stripes in the high -temperature superconductors. *Rev. Mod. Phys*, 75(2003):1201, 2003.
20. G. Burns. *High-Temperature Superconductivity*. Academic Press, Inc, 1992.
21. J. C. Campuzano, M. R. Norman, and M. Randeria. *Physics of Conventional and Unconventional Superconductors*. Springer-Verlag, 2004.
22. A. Damascelli, Z. Hussain, and Z. X Shen. Angle-resolved photoemission studies of the cuprate superconductors. *Rev. Mod. Phys*, 75:473, 2003.
23. A. A. Abrikosov and L. P. Gorkov. *Zh. Eksperim. i Teor. Fiz*, 39:1781, 1960.
24. A. A. Abrikosov and L. P. Gorkov. *Soviet Phys JETP*, 12:1243, 1961.
25. P. W. Anderson. *The Theory of Superconductivity in the High- $T_c$  Cuprates*. Princeton University Press, 1997.
26. M. R. Norman, D. Pines, and C. Kallin. The pseudogap: friend or foe of high  $t_c$ ? *Adv. Phys*, 54:715, 2005.

27. H. Ding, T. Yokya, J. C. Campuzano, T. Takahashi, M. Randeria, M. R. Norman, T. Mochiku, K. Kadowaki, and J. Gaiapintzakis. Spectroscopic evidence for a pseudogap in the normal state of underdoped high- $t_c$  superconductors. *Nature*, 382:51, 1996.
28. Y. S. Ando, G. S. Boebinger, A. Passner, N. L. Wang, C. Geibel, and F. Steglich. Metallic in-plane and divergent out-of-plane resistivity of a high- $t_c$  cuprate in the zero-temperature limit. *Phys. Rev. Lett.*, 77:2065, 1996.
29. J. M. Harris, Y. F. Yan, and N. P. Ong. Experimental test of the  $t^2$  law for the hall angle from  $t_c$  to 500 k in oxygen-reduced  $\text{YBa}_2\text{Cu}_3\text{O}_{6+x}$  crystals. *Phys. Rev. B*, 46:14293, 1992.
30. B. Statt T. Timusk. The pseudogap in high-temperature superconductors: an experimental survey. *Rep. Prog. Phys*, 62:61, 1999.
31. M. R. Norman, H. Ding, M. Randeria, J. C. Campuzano, T. Yokya, T. Takeuchi, T. Takahashi, T. Mochiku, K. Kadowaki, P. Guptasarma, and D. G. Hinks. Destruction of the fermi surface in underdoped high- $T_c$  superconductors. *Nature*, 392:157, 1998.
32. A. Einstein. *A. Ann.Physik*, 31:132, 1905.

33. G. D. Mahan. Angular dependence of photoemission in metals. *Phys. Rev. Lett.*, 24:1068, 1970.
34. W. L. Schaich and N. W. Ashcroft. Model calculations in the theory of photoemission. *Phys. Rev. B*, 3:2452, 1971.
35. C. N. Berglund and W. E. Spicer. Photoemission studies of copper and silver: Theory. *Phys. Rev.*, 136:A1030, 1964.
36. G.D.Mahan. *Many Particle Physics*. Plenum Press, 1990.
37. Ding H, et al. (1996) Spectroscopic evidence for a pseudogap in the normal state of underdoped high-Tc superconductors. *Nature* 382:5154.
38. Loeser AG, et al. (1996) Excitation gap in the normal state of underdoped Bi<sub>2</sub>Sr<sub>2</sub>CaCu<sub>2</sub>O<sub>8</sub> . *Science* 273:325329.
39. Kaminski A, et al. (2003) Crossover from coherent to incoherent electronic excitations in the normal state of Bi<sub>2</sub>Sr<sub>2</sub>CaCu<sub>2</sub>O<sub>8</sub>. *Phys Rev Lett* 90:207003.
40. Valla T, et al. (2000) Temperature dependent scattering rates at the Fermi surface of optimally doped Bi<sub>2</sub>Sr<sub>2</sub>CaCu<sub>2</sub>O<sub>8</sub>.
41. Chatterjee U, et al. (2010) Observation of a d-wave nodal liquid in highly underdoped Bi<sub>2</sub>Sr<sub>2</sub>CaCu<sub>2</sub>O<sub>8</sub> . *Nat Phys* 6:99103.

- 42. Norman MR, et al. (1998) Destruction of the Fermi surface in underdoped high-Tc superconductors. *Nature* 392:157160.
- 43. Varma CM (2006) Theory of the pseudogap state of the cuprates. *Phys Rev B Condens Matter Mater Phys* 73:155113.
- 44. Sachdev S (2010) Where is the quantum critical point in the cuprate superconductors? *Phys Status Solidi B* 247:537543.
- 45. Varma CM, et al. (1989) Phenomenology of the normal state of the Cu-O hightemperature superconductors. *Phys Rev Lett* 63:19961999.
- 46. Anderson PW(1987) The resonating valence bond state in La<sub>2</sub>CuO<sub>4</sub> and superconductivity. *Science* 235:11961198.
- 47. Suzumura Y, Hasegawa Y, Fukuyama H (1988) Mean field theory of RVB and superconductivity. *J Phys Soc Jpn* 57:27682778.
- 48. Kotliar G (1988) Resonating valence bonds and d-wave superconductivity. *Phys Rev B Condens Matter Mater Phys* 37:36643666.
- 49. Lee PA, Nagaosa N, Wen X-G (2006) Doping a Mott insulator: Physics of hightemperature superconductivity. *Rev Mod Phys* 78:1785.

50. Timusk T, Statt B (1999) The pseudogap in high-temperature superconductors: An experimental survey. Rep Prog Phys 62:61122.
51. Valla T, et al. (2002) Coherence-incoherence and dimensional crossover in layered strongly correlated metals. Nature 417:627630.
52. Matsui H, et al. (2003) BCS-like bogoliubov quasiparticles in high-Tc superconductors observed by angle resolved photoemission spectroscopy. Phys Rev Lett 90:217002.
53. Kanigel A, et al. (2006) Evolution of the pseudogap from Fermi arcs to the nodal liquid. Nat Phys 2:447451.
54. Kastner, M. A. , Birgenau, R. J. Magnetic, transport, and optical properties of monolayer copper oxides. Rev. Mod. Phys. 70, 897-928 (1998).
55. Tsuei, C. C., Kirtley, J. R., Hammerl, G., Mannhart, J., Raffy, H., Li, Z. Z. Robust  $d_{x_2y_2}$  Pairing Symmetry in Hole-Doped Cuprate Superconductors. Phys. Rev. Lett. 93, 187004 (2004).
56. Konstantinovic, Z., Li, Z. Z., Raffy, H. Normal state transport properties of single- and double-layered  $\text{Bi}_2\text{Sr}_2\text{Ca}_{n-1}\text{Cu}_n\text{O}_y$  thin films and the pseudogap effect. Physica C 341-348, 859 - 862 (2000).



57. Oh, S., Crane, T. A., Van Harlingen, D. J. Eckstein, J. N. Doping Controlled Superconductor-Insulator Transition in  $\text{Bi}_2\text{Sr}_{2-x}\text{La}_x\text{CaCu}_2\text{O}_{8-\delta}$ . Phys. Rev. Lett. 96,107003 (2006).
58. Matei, I., Li, Z. Z., Raffy, H. Observation of the superconducting-insulating transition in a  $\text{BiSr}(\text{La})\text{CuO}$  thin film tuned by varying the oxygen content. J.Phys.: Conf. Ser. 150, 052154 (2009).
59. Campuzano, J.C. et al. Electronic Spectra and Their Relation to the  $(\pi, \pi)$  Collective Mode in High-Tc Superconductors, Phys. Rev. Lett. 83, 3709-3712 (1999).
60. Norman, M. R. et al. Destruction of the Fermi surface in underdoped high-Tc superconductors. Nature 392, 157-160 (1998).
61. Kaminski, A. et al. Identifying the background signal in angle-resolved photoemission spectra of high-temperature cuprate superconductors. Phys. Rev B 69, 212509 (2004).
62. Kanigel, A. et al. Evolution of the pseudogap from Fermi arcs to the nodal liquid. Nature Physics 2, 447-451 (2006).
63. Doiron-Leyraud, N. et al. Onset of a Boson Mode at the Superconducting Critical Point of Underdoped  $\text{YBa}_2\text{Cu}_3\text{O}_y$ . Phys. Rev. Lett. 97, 207001 (2006).

64. See Huefner, S., Hossain, M. A., Damascelli, A., Sawatzky, G. A. Two gaps make a high-temperature superconductor? Rep. Prog. Phys. 71, 062501 (2008) and references therein.
65. Mesot, J. et al. Superconducting Gap Anisotropy and Quasiparticle Interactions: A Doping Dependent Photoemission Study. Phys. Rev. Lett. 83,840-843 (1999).
66. Tanaka, K. et al. Distinct Fermi-MomentumDependent Energy Gaps in Deeply Underdoped Bi2212. Science 314, 1910-1913 (2006).
67. Ma, J.-H., et al. Coexistence of Competing Orders with Two Energy Gaps in Real and Momentum Space in the High Temperature Superconductor  $\text{Bi}_2\text{Sr}_{2-x}\text{La}_x\text{CuO}_{6+\delta}$ . Phys. Rev. Lett. 101, 207002 (2008).
68. He, R.-H. et al. Energy gaps in the failed high-Tc superconductor  $\text{La}_{1.875}\text{Ba}_{0.125}\text{CuO}_4$ . Nat. Phys. 5, 119-123 (2009).
69. Pushp, A. et al. Extending Universal Nodal Excitations Optimizes Superconductivity in  $\text{Bi}_2\text{Sr}_2\text{Ca}_{n-1}\text{Cu}_n\text{O}_y$ . Science 324, 1689-1693 (2009).
70. Lee, J. et al. Spectroscopic Fingerprint of Phase Incoherent Superconductivity in the Pseudogap State of Underdoped  $\text{Bi}_2\text{Sr}_2\text{CaCu}_2\text{O}_{8+\delta}$ . Science (to be published).

71. Sutherland, M. et al. Thermal conductivity across the phase diagram of cuprates: Low-energy quasiparticles and doping dependence of the superconducting gap. *Phys. Rev. B* 67, 174520 (2003).
72. Shi, M. et al. Coherent d-Wave Superconducting Gap in Underdoped  $\text{La}_{2-x}\text{Sr}_x\text{CuO}_4$  by Angle-Resolved Photoemission Spectroscopy. *Phys. Rev. Lett.* 101, 047002 (2008).
73. Valla, T. et al. The Ground State of the Pseudogap in Cuprate Superconductors. *Science* 314, 1914-1996 (2006).
74. Meng, J. et al. Monotonic d-wave superconducting gap of the optimally doped  $\text{Bi}_2\text{Sr}_{1.6}\text{La}_{0.4}\text{CuO}_6$  superconductor by laser-based angle-resolved photoemission spectroscopy. *Phys. Rev. B* 79, 024514 (2009).
75. Wei, J. et al. Superconducting Coherence Peak in the Electronic Excitations of a Single-Layer  $\text{Bi}_2\text{Sr}_{1.6}\text{La}_{0.4}\text{CuO}_{6+\delta}$  Cuprate Superconductor. *Phys. Rev. Lett.* 101, 097005 (2008).
76. Meng, J. et al. Direct Observation of Fermi Pocket in High Temperature Cuprate Superconductors. *arXiv:0906.2682*.
77. Hetel, I., Lemberger, T. R., Randeria, M. Quantum critical behaviour in the superfluid density of strongly underdoped ultrathin copper oxide films. *Nature*

Physics 3, 700-702 (2007).

78. Wang, Y., Li, L. Ong, N. P. Nernst effect in high-Tc superconductors. Phys. Rev. B 73, 024510 (2006).
79. Li, L., Chechelsky, J. G., Komiya, S., Ando, Y. Ong, N. P. Low-temperature vortex liquid in  $\text{La}_{2x}\text{Sr}_x\text{CuO}_4$ . Nature Physics 3, 311-314 (2007).
80. Shen, K. M. et al. Fully gapped single-particle excitations in lightly doped cuprates. Phys. Rev. B 69, 054503 (2004).
81. Anderson, P. W. et al. The physics behind high-temperature superconducting cuprates: the plain vanilla version of RVB. J. Phys. Cond. Mat. 16, R755-R799 (2004).
82. Balents, L., Fisher, M. P. A., Nayak, C. Nodal Liquid Theory of the Pseudo-Gap Phase of High-Tc Superconductors. Int. J. Mod. Phys. B 12, 1033-1068 (1998).
83. Tesanovic, Z. d-wave duality and its reflections in high-temperature superconductors. Nature Physics 4, 408-414 (2008).
84. T. Senthil Critical Fermi surfaces and non-Fermi liquid metals Phys. Rev. B 78, 035103 (2008)